OUKA
The University of Osaka
Institutional Knowledge Archive

Title	Comprehensive Evaluation of Double-Wire Narrow Gap GMAW Process and Dissimilar Joints Properties
Author(s)	Xiao, Ning
Citation	大阪大学, 2026, 博士論文
Version Type	VoR
URL	https://doi.org/10.18910/105490
rights	
Note	

The University of Osaka Institutional Knowledge Archive : OUKA

https://ir.library.osaka-u.ac.jp/

The University of Osaka

Doctoral Dissertation

Comprehensive Evaluation of Double-Wire Narrow Gap GMAW Process and Dissimilar Joint Properties

(ダブルワイヤ・ガスシールドメタルアーク溶接によるナロウギャップ異材継手性能の総合評価)

XIAO NING

January 2026

Graduate School of Engineering,
The University of Osaka

Table of Contents

Chapter 1. Introduction 5
1.1 Background and significance of the subject 5
1.2. Narrow gap welding 6
1.2.1. Definition and application background 6
1.2.2. Classification and characteristics 6
1.2.3. Difficulty and solution 9
1.3. GMAW narrow gap welding 13
1.3.1. Single-wire narrow gap GMAW 13
1.3.2. Double-wire narrow gap GMAW 15
1.4. Deposition for high-strength and low-alloy (HSLA) steel 17
1.5. Dissimilar steels welding 19
1.6. Wire arc cladding for enhancement in wear resistance 21
1.7. Numerical simulation for temperature field during GMAW 24
1.8. Purpose and outline 26
Chapter 2. Double-wire narrow gap welding process optimization 31
2.1. Research purpose and process conditions 31
2.1.1 Research purpose 31
2.1.2 Welding setup and materials 31
2.1.3 Welding parameters 32
2.2. Dynamic behaviors of arc and droplets and their generation mechanism in single-wire welding 34
2.3. Dynamic behaviors of arc and droplets in double-wire welding and spacing influence 36
2.4. Weld formation in double-wire welding and spacing influence 40
2.5. Summary 46
Chapter 3. Improvement of microstructure and mechanical properties of deposited weld metal ER70-G 47
3.1. Welding conditions and welding material 47
3.1.1 Materials and method 47
3.1.2 Microstructure and mechanical properties characterization 49
3.1.3 Thermal modeling 51
3.2. Simulation for dwell time influence 53
3.3. Improvement of microstructure via dwell time strategy 54
3.3.1 Phase composition 54
3.3.2 Microstructure characteristics 55
3.4. Improvement of mechanical properties via dwell time strategy 59
3.4.1 Microhardness 59
3.4.2 Tensile properties 60
3.4.3 Impact toughness 62
3.5. Mechanisms of mechanical properties improvement 64
3.6. Summary 67
Chapter 4. Comprehensive evaluation of NM450/ER70-G/ZG30SiMn dissimilar welded joint 69

4.1. Welding conditions and welding material 69
4.1.1. Materials and Methods 69
4.1.2. Microstructure analysis 72
4.1.3. Mechanical properties analysis 72
4.1.4. Thermal modeling 73
4.2. Elements distribution characteristics in welded joint 74
4.3. Microstructure characteristics and evolution in welded joint 75
4.3.1 Macroscopic forming of welded joints 75
4.3.2 Phase and microstructure characteristics of the weld seam 76
4.3.3 Microstructure characteristics of the HAZ 80
4.3.4 Thermal induced microstructure evolution of the welded joint 81
4.4. Comprehensive evaluation of mechanical properties in welded joint 83
4.4.1 Microhardness 83
4.4.2 Tensile properties 84
4.4.3 Impact toughness 86
4.4.4 Bend properties 87
4.5. Summary 88
Chapter 5. Wear performance and microstructures of Fe-Cr-C alloy cladding on heterogeneous welded joint of NM450/ER70-G/ZG30SiMn 90
5.1. Cladding conditions and material 90
5.1.1 Cladding experiment setup 90
5.1.2 Material characterization 91
5.1.3 Wear resistance evaluation 92
5.2. Macrostructure characteristics of the cladding layer 93
5.2.1 Macro-morphology of the cladding layer 93
5.2.2 Metallographic observation of the cladding layer 94
5.3. Microstructure characteristics of the cladding layer 98
5.3.1 Microstructure characteristics at the NM450/cladding layer interface 98
5.3.2 Microstructure characteristics at the ER70-G/cladding layer interface 101
5.3.3 Microstructure characteristics at the ZG30SiMn/cladding layer interface 103
5.3.4 Microstructure characteristics of the ternary mixing zones 105
5.4. Wear performance improvement for the welded joint 106
5.4.1 Microhardness distribution of the cladding layer 106
5.4.2 Wear performance evaluation for the welded joint 107
5.5. Summary 110
Chapter 6. Summary and prospect 111
References 114
Achievements 127
Acknowledgements 128
Supplementary materials 128

Chapter 1. Introduction

1.1 Background and significance of the subject

Coal remains one of the most abundant fossil fuel resources globally, playing a pivotal role in meeting global energy demands[1]. It serves not only as a primary energy source for electricity generation but also as a key raw material in various industries. The efficient extraction and transportation of coal are essential for maximizing resource utilization and ensuring economic viability in the mining sector. In this context, the design and functionality of equipment used in coal mining, particularly scraper conveyors, are pivotal in enhancing mining efficiency and operational effectiveness[2].

Scraper conveyors are extensively employed in underground coal mines to transport mined coal from working faces to surface storage or processing facilities. Central to the conveyor's performance is the chute structure, which supports the system and facilitates coal movement. The chute primarily consists of a running mechanism, blocking coal board, middle plate, and groove. This structure must exhibit robustness and reliability, as failures can lead to significant downtime and economic losses. Optimizing the design and manufacturing processes of this structure is therefore critical for ensuring the efficient operation of coal mining equipment.

A critical factor influencing chute durability is the welding quality of component joints, particularly between the middle plate and groove[3]. The middle plate is typically made of wear-resistant steel to withstand high-frequency friction, while the groove is fabricated from cast steel. To enhance structural integrity, these components often feature large thicknesses and high strength[4]. However, high-strength steels present weldability challenges, including cold cracking susceptibility, which necessitates mismatched weld metals for joint optimization[5]. Traditional thick-plate welding relies on V-shaped grooves with large angles[6], where multi-layer, multi-pass filling increases heat input (which degrades joint performance) and reduces production efficiency. Later, K-shaped or X-shaped grooves gained prominence. Although these reduce filler metal volume, the requirement for structural flipping during double-side

welding extends production time. In addition, chute structures are subjected to long-term friction from coal, leading to inevitable surface degradation. Joint fracture and surface damage are common failure modes, highlighting the urgent need for advanced manufacturing and surface engineering technologies to ensure durability and longevity.

Double wire narrow gap gas metal arc welding (GMAW) is an effective method for joining thick-walled structures, while arc cladding with Fe-Cr-C alloys can enhance wear resistance. This study addresses these gaps by conducting a comprehensive evaluation of double-wire narrow gap GMAW for dissimilar steel joints and improving their performance through cladding, contributing to advancements in welding technology and surface engineering.

1.2. Narrow gap welding

1.2.1. Definition and application background

In the field of thick-walled metal structure manufacturing, narrow gap welding has become a research hotspot in both academic and engineering communities due to its high efficiency and quality as an advanced joining technology[7]. Its technical framework is built around a core feature: the use of extremely small groove angles and groove widths to form narrow, deep I-shaped, U-shaped, or V-shaped grooves, achieved through fusion welding methods to accomplish multi-layer and multi-pass welding. Compared with traditional wide-groove welding techniques, narrow gap welding significantly reduces the weld cross-sectional area (by up to 30%-80%), thereby substantially decreasing filler metal consumption (saving 20%-50% of material) and heat input. This design not only enhances economic efficiency but also effectively improves the mechanical properties of the joint by reducing heat input, notably increasing toughness and plasticity while minimizing welding stress and distortion. This technology has demonstrated irreplaceable advantages in critical applications involving thick plates (typically above 30mm), such as nuclear pressure vessels, offshore platforms, and heavy machinery[8].

1.2.2. Classification and characteristics

Based on the heat source type, narrow gap welding technologies can be classified

into narrow gap arc welding, narrow gap laser welding, narrow gap electron beam welding, and narrow gap hybrid welding. Among these, narrow gap arc welding can be further subdivided into narrow gap gas metal arc welding (NG-GMAW), narrow gap gas tungsten arc welding (NG-GTAW), narrow gap submerged arc welding (NG-SAW), and others. Fig. 1.1 illustrates schematic diagrams of these narrow gap welding methods. Each of these techniques finds practical engineering applications by leveraging their distinct advantages and characteristics.

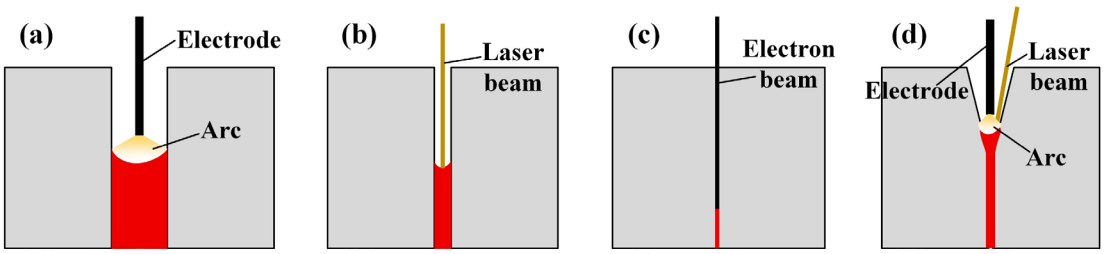


Fig. 1.1. Classification of narrow gap welding methods: (a) narrow gap arc welding, (b) narrow gap laser welding, (c) narrow gap electron beam welding, (d) narrow gap laser-arc hybrid welding.

Narrow gap arc welding utilizes an arc as the heat source and offers advantages such as high welding efficiency and low cost. In particular, narrow gap GMAW features a wide range of applicable parameters, all-position welding capability, and high deposition efficiency, making it widely applicable to materials such as low-alloy steels, stainless steels, and aluminum alloys[9]. Narrow gap GTAW uses a tungsten electrode to generate the arc, offering benefits such as a stable process, spatter-free operation, and high weld quality. It is particularly suitable for root passes and welding of thermally sensitive materials, finding extensive use in titanium alloys, stainless steels, and others[10]. However, a relative disadvantage of GTAW is its comparatively lower deposition efficiency. Narrow gap SAW is renowned for its high deposition efficiency and spatter-free operation, making it especially suitable for flat-position welding of thick-walled low-alloy steel containers[11]. A drawback is its relatively high heat input, which can affect joint toughness. Furthermore, the groove width in SAW often cannot be too small, and it is difficult to apply in positions other than flat. Current research on narrow gap arc welding primarily focuses on further improving welding or deposition

efficiency, reducing groove width, and enhancing process stability and quality through heat source optimization. Narrow gap arc welding holds broad application prospects in fields such as engineering machinery, nuclear power, and offshore engineering.

Narrow gap laser welding uses a laser as the heat source. Lasers provide high energy density, enabling deep penetration and high welding speeds. It is mainly divided into two types: autogenous welding[12] and wire-feed welding[7]. Autogenous welding does not use filler material, relying solely on the laser energy to melt the base metal, resulting in very low heat input and minimal distortion. However, it demands extremely high fit-up accuracy (e.g., gap, misalignment). Wire-feed welding introduces filler wire synchronously to compensate for fit-up deviations, adjust weld composition, and improve joint properties. A challenge in narrow gap laser welding is the tendency for defects like porosity, cracking, and columnar grains due to the high cooling rate and high depth-to-width ratio. The introduction of beam oscillation technology is a key advancement[13], effectively expanding the heat source action zone, promoting sidewall fusion, agitating the molten pool to aid gas escape, significantly reducing the tendency for porosity and lack of sidewall fusion, and refining the grain structure.

Narrow gap electron beam welding is performed in a high-vacuum environment. Its most prominent characteristic is the extremely high energy density, capable of producing welds with a very high depth-to-width ratio[14]. The vacuum environment effectively prevents atmospheric contamination, yielding very pure, high-quality welds ideally suited for reactive metals like titanium and zirconium[15]. This technique produces a very narrow heat-affected zone with minimal welding stress and distortion. Its application is limited by vacuum chamber size, complex and expensive equipment, and the need to prevent magnetic arc blow interference during welding. Electron beam scanning can be employed to improve weld bead morphology. This technology is primarily used for critical components requiring the highest quality standards in aerospace, nuclear industry, and other fields, such as aircraft engine rotors and nuclear reactor components.

Narrow gap hybrid welding aims to synergistically combine the advantages of

different heat sources to achieve a "1+1>2" effect. Taking the common laser-arc hybrid welding as an example: the laser provides high energy density, ensuring penetration depth and speed, while the arc heat source has a wider action zone, improving sidewall fusion[16]. The nature of the arc aids in preheating the wire and base metal, increasing deposition efficiency, and relaxing the stringent requirements on joint fit-up. This synergistic effect makes hybrid welding more robust and adaptable than laser welding alone for thick plates, especially in on-site conditions where fit-up accuracy or gap consistency is difficult to guarantee. This technique is suitable for on-site welding of large thick-walled structures such as those in heavy machinery, offshore platforms, and petrochemical pipelines.

1.2.3. Difficulty and solution

While narrow gap electron beam welding offers advantages such as high welding quality and efficiency, its stringent requirement for a vacuum environment and relatively high cost limit its widespread application in fields like engineering machinery. Currently, the most widely used narrow gap welding methods in the industry are narrow gap laser welding and narrow gap arc welding. Although narrow gap welding reduces groove size, improves welding efficiency, and lowers production costs, its mature application still faces certain challenges.

When filler wire is required in narrow gap welding, the base materials to be joined typically require a groove. A distinctive feature of narrow gap welding technology is that the sidewalls of the groove are nearly parallel, and the width between them is extremely narrow. The central axis of heat sources such as arcs or laser beams is usually parallel to the sidewalls, making it difficult for heat to act directly and effectively on the base material of the sidewalls. If the heat input is insufficient or the heat source's action area is too small (e.g., an overly focused laser spot), the sidewall base material may not reach the melting temperature, leading to lack of fusion defects (Fig. 1.2), which severely compromise the quality of the welded joint. To address these issues, researchers worldwide have conducted extensive studies, with the fundamental goal being to optimize the temperature field distribution within the narrow gap groove,

ensuring the sidewalls receive sufficient heat to prevent lack of fusion defects.

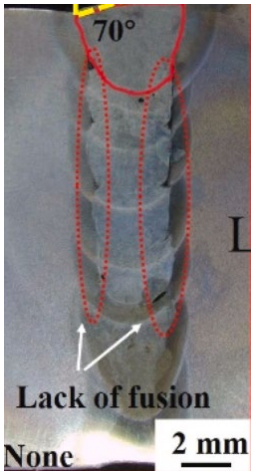


Fig. 1.2. Lack-of-fusion defects in laser narrow gap welding[13].

Laser welding is a high-energy beam welding process. Most researchers address lack of fusion defects in narrow gap welding by redistributing heat within the groove via beam oscillation or wire oscillation. In the field of narrow gap laser welding: Lei et al.[7] proposed a novel high-efficiency narrow gap dual-beam laser welding method utilizing laser plume energy radiation to achieve "quasi-hot wire" filling. By controlling the solidification behavior of the molten pool through the dual-beam approach, reliable suppression of solidification cracking was achieved. The development of a high temperature resistant tungsten wire feeding nozzle improved the feeding speed and stability of the filler wire. Heating the tungsten wire feeding nozzle via laser plume energy radiation enabled "quasi-hot wire" filling, successfully welding 120-mm-thick high-strength steel. Long et al.[17] performed narrow gap laser wire feeding welding on thick TC4 titanium alloy plates with V-grooves in a narrow gap butt joint configuration, applying beam oscillation during the process. The relationship between welding conditions and lack of fusion was investigated for four groove widths (4, 6, 8, and 10 mm). The study found that eliminating lack of fusion requires consideration of two aspects: first, the beam oscillation amplitude should be appropriate; second, the ratio of line energy to wire feed rate should be suitable. Li et al.[18] developed a new narrow gap laser welding method that introduces an electromagnetically assisted wire oscillation technique to regulate energy distribution, melt flow, and metallurgical

structure. Results indicated that the forced convection generated by the electromagnetic wire oscillation enlarged the molten pool size and drove high-temperature weld metal toward the groove sidewalls. This improved the wetting of the liquid weld metal on the sidewalls, resulting in a concave weld bead profile, thereby preventing incomplete sidewall fusion. Additionally, the oscillation of both the wire and the beam refined the grain structure and enhanced mechanical properties. Wang et al.[19] introduced ring-core adjustable laser technology to the narrow gap welding process. Through experimental and numerical simulation methods, they investigated the effects of groove gap and ring-core ratio on the molten pool morphology in ring-core adjustable laser welding of narrow gap structures, achieving high-quality welding of titanium alloys.

In narrow gap arc welding, addressing lack-of-fusion defects can be approached from aspects such as welding parameters, torch design, wire geometry, number of wires, and auxiliary energy fields. In terms of welding parameters, increasing the welding current and heat input expands the width of the weld pool, thereby improving sidewall fusion. This approach has been effectively applied in NG-SAW, where the welding current is generally higher compared to other arc welding processes, resulting in relatively fewer sidewall fusion issues. However, increasing the welding current in NG-GTAW is limited by the current-carrying capacity of the tungsten electrode, making it difficult to enhance sidewall fusion through current adjustment alone. In NG-GMAW, increasing the welding current can, to some extent, improve sidewall fusion. However, excessively high current may alter the droplet transfer mode, leading to rotating spray transfer. It can also cause arc instability along the sidewalls, increase spatter, and ultimately deteriorate weld bead formation. Furthermore, high-current welding involves substantial heat input, which can easily cause microstructural defects and adversely affect the mechanical properties of the joint.

In terms of torch structure, the issue of inadequate sidewall fusion can be addressed by incorporating arc oscillation or rotation mechanisms to alter the arc's position within the groove. Among these, oscillating arcs are typically achieved using motors for forward and reverse rotation, which has been applied in both narrow gap GMAW and

GTAW. Wei et al.[20] investigated the stirring effect of a rotating arc on the molten pool during asymmetric tungsten narrow gap GTAW. They found that, compared to conventional static tungsten welding, the liquid metal layer in the molten pool exhibited intense fluctuations under the influence of the rotating asymmetric tungsten electrode. The periodic rotation of the arc significantly altered the flow pattern of the molten pool. A vortex formed near the edges of the pool, enhancing sidewall scouring and thereby improving sidewall fusion in narrow gap welding.

In terms of wire geometry, the use of various pre-deformed wires—such as wave-shaped, bent, spiral, or twisted wires—induces periodic oscillation of the arc within the narrow groove during combustion at the wire tip, owing to the predetermined deformation of the wire. This oscillation enhances sidewall fusion. However, such methods typically require specially pre-formed wires (e.g., twisted wires) or the integration of a wire pre-deformation mechanism within the wire feed system near the torch front. Additionally, they necessitate specialized wire guide components and contact tubes within the narrow gap welding torch, significantly increasing the complexity of the wire feeding system, reducing wire feed reliability, limiting wire versatility, and raising manufacturing costs.

In terms of wire quantity, introducing multiple wires for narrow gap welding is an effective approach. In multi wire welding, some researchers have developed cable-type wires[21], while others have employed multiple independent wires. On one hand, multi-wire welding expands the molten pool size, aiding in addressing lack of fusion defects. On the other hand, it significantly enhances welding efficiency. However, improper multi-wire welding parameters can result in excessive heat input, which may deteriorate the mechanical properties of the joint.

In terms of external field control, the application of an alternating magnetic field can manipulate the arc to oscillate laterally within the narrow groove at a specific frequency during welding. This guides the arc to periodically heat the groove sidewalls, thereby improving sidewall fusion. The method of using an external magnetic field to control arc oscillation is generally applied in NG-TIG, with relatively limited research in the

field of NG-GMAW. Li et al.[22] developed a novel unilateral wall wetting test to investigate the wetting behavior of molten metal on narrow gap sidewalls and its effect on lack of fusion defects in arc oscillated NG-GTAW. The results demonstrated that arc oscillation significantly improves the wettability of the molten metal on both the plate and the narrow gap sidewalls. Furthermore, Li et al.[23] successfully applied NG-GTAW to the welding of ferromagnetic materials. Sun et al.[10] introduced an oscillating filler wire into magnetically controlled NG-GTAW. Through wire oscillation, the wire feed rate was increased from 1.8 m/min to 2.2 m/min with minimal heat input. This method significantly enhances welding efficiency by effectively utilizing the energy of both the arc and the molten pool. Additionally, the authors achieved high-quality welding of titanium alloys using this technique.

In narrow gap laser arc hybrid welding, addressing lack of fusion defects typically involves optimizing welding parameters and implementing beam oscillation techniques. Yu et al.[24] achieved high-quality welds in thick-plate titanium alloy narrow gap welding by optimizing laser power and wire feed speed, which improved arc stability and resulted in concave weld bead profiles. Yang et al.[25] employed a rotating laser as the heat source in narrow gap laser-MIG hybrid welding of aluminum alloys. This approach effectively resolved lack of fusion defects along the sidewalls, while the rotating laser agitation of the molten pool reduced porosity and significantly refined the grain structure.

The aforementioned narrow gap welding methods each demonstrate unique advantages in practical applications. However, in the field of engineering machinery, particularly for welding alloy steels or low-carbon steels, narrow-gap GMAW has gained the most extensive application due to its high welding efficiency, low cost, and broad range of process parameters. In Section 1.3, the author will provide a detailed analysis of the current research status of narrow gap GMAW.

1.3. GMAW narrow gap welding

1.3.1. Single-wire narrow gap GMAW

Currently, the most widely applied methods in single-wire narrow gap GMAW are

oscillating arc and rotating arc narrow-gap welding. Based on the principles of arc oscillation, these can be categorized into pre-bent wire oscillation and mechanical wire oscillation. Pre-bent wire oscillation is less commonly used in practical applications due to the complexity and higher cost of the welding system. Mechanical wire oscillation, on the other hand, is achieved by a motor directly driving the wire oscillation mechanism within the narrow gap GMAW torch. This generally involves two approaches: the wire oscillating left and right within the groove perpendicular to the welding direction, or the wire rotating around a central axis via a curved contact tube, as illustrated in Fig. 1.3. The curved contact tube deflects the wire from the groove center toward the sidewall. The motor-driven periodic oscillation of the curved contact tube enables cyclic heating of the sidewalls, thereby addressing lack of fusion defects. Numerous studies have been conducted by researchers worldwide on oscillating arc GMAW[9, 26-28]. Oscillation parameters, including amplitude and frequency, significantly influence weld bead formation and welding quality.

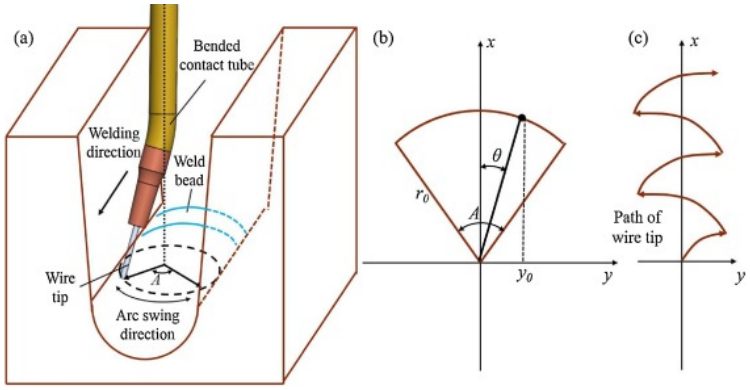


Fig. 1.3. Schematic diagram of the wire oscillating GMAW system[9]: (a) 3D view of the wire oscillation system, (b)oscillation parameters, (c) oscillation trajectory.

Yang et al.[29] investigated the stability of the welding process during overhead narrow-gap pulsed GMAW of thick plates by using high-speed photography and electrical signal acquisition systems to capture arc behavior and droplet transfer under different oscillation widths. The results revealed that as the oscillation width increased, the arc shape transformed from a symmetrical trumpet-like distribution around the groove center to a deflected arc increasingly toward the sidewall. The droplet transfer mode shifted from one droplet per pulse to multiple droplets per pulse, leading to

defects such as inadequate sidewall fusion and weld undercut. Su et al.[30] developed a passive infrared vision sensing method to measure groove width under intense welding interference, addressing the issue of poor bead formation caused by variations in groove width in oscillating arc narrow gap welding. Chen et al.[31] applied arc ultrasound technology to aluminum alloy oscillating arc narrow-gap GMAW and found that the arc expanded after superimposing ultrasonic current, with different arc behaviors observed at various positions within the narrow groove. At the sidewall, the expansion of the non-oscillating arc was significantly greater than that of the oscillating arc, while at the groove bottom, the oscillating arc exhibited greater expansion than the non-oscillating arc.

Another widely studied narrow-gap GMAW method is rotating arc GMAW[32-34]. This technique does not require a pre-set wire deflection angle. The rotation of the arc generates centrifugal force in the molten pool, which reduces the heat input to the base metal and enhances sidewall fusion. Guilherme M. S. Silveira et al.[35] employed a GMAW process with a rotating electrode for steel plate welding and investigated the effects of rotation frequency and diameter on the microstructure and mechanical properties of the weld metal. Li et al.[36] used finite element analysis to study multi-layer rotating arc narrow gap GMAW of medium-thick steel plates, calculating residual stresses based on temperature fields under four different welding conditions, providing important references for microstructure and structural analysis of rotating arc narrow-gap GMAW welds. However, due to the high requirements for mechanical control and the relatively poor structural stability of the torch, this method has not been widely adopted in practical production.

1.3.2. Double-wire narrow gap GMAW

With the increasing pursuit of welding efficiency, double wire narrow gap GMAW has emerged as a solution. Double wire narrow gap GMAW utilizes two independent welding power sources and two arcs, where two wires are ignited to generate separate arcs. The core technology lies in directing each wire towards a respective sidewall, allowing the arcs to partially burn on the sidewalls during welding to heat the base metal

and promote sidewall fusion[37]. Fig. 1.4 illustrates a schematic diagram of a typical double wire narrow gap GMAW experimental system and the corresponding wire arrangement.

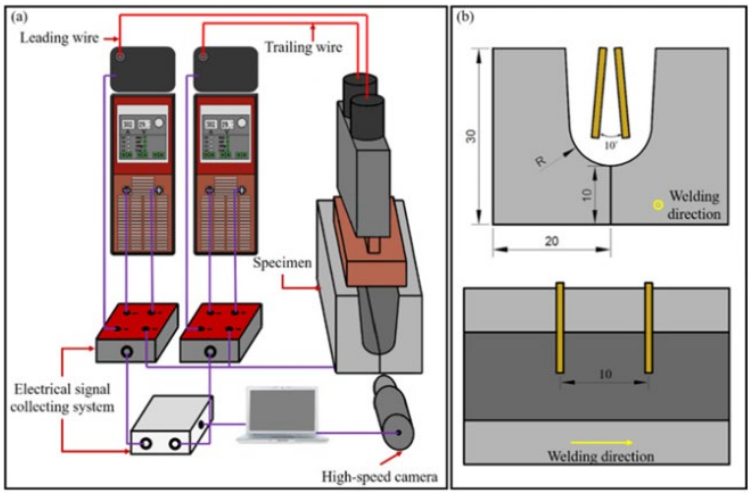


Fig. 1.4. (a) Schematic diagram of the double wire narrow gap GMAW system setup, (b) Schematic diagram of the wire arrangement[37].

Liu et al.[38] conducted experiments using a double wire narrow gap GMAW system to investigate the influence of the inter-wire angle on the formation of undercut defects and arc behavior. The results indicated that as the inter-wire angle increased, the stability of the welding process improved. However, the mutual electromagnetic attraction between the two arcs decreased with an increase in the inter-wire angle. The two arcs shifted from the groove bottom towards the sidewalls, transferring more heat to the sidewalls and thereby increasing the weld width. This could lead to severe undercut defects. Kang et al.[39] studied the arc and droplet transfer behavior in an asynchronous DC-AC pulsed double wire GMAW process. The authors demonstrated that spatter was generated by attractive and repulsive arc interactions. Attractive arc interference hindered stable droplet transfer, while repulsive interaction could induce short-circuiting of suspended droplets. Cai et al.[40] employed the double wire narrow gap GMAW method to perform welding in flat, overhead, and vertical-down positions, and investigated the characteristics of the narrow gap weld pool and bead formation. Furthermore, Cai et al.[41] examined the effect of shielding gas composition on arc behavior and weld bead morphology in double wire narrow gap GMAW. The shielding

gases included argon, carbon dioxide, and helium, and the results showed that arc behavior differed depending on the shielding gas used. Han et al.[42] performed simulations of double wire narrow gap GMAW based on computational fluid dynamics (CFD). The results revealed that lower wire feed speeds or higher travel speeds were prone to cause lack of fusion defects, while higher wire feed speeds could result in finger-like penetration. A clockwise vortex on the right sidewall and a counterclockwise vortex on the left sidewall enhanced lateral transport of fluid and heat, facilitating the formation of a concave weld bead.

In addition to the configuration where both wires act as electrodes, another variant of double wire narrow GMAW involves one wire serving as the electrode while the other is fed into the molten pool as a cold or hot wire. This approach has been reported in several studies[43-45].

Despite the existing body of research on double wire narrow gap GMAW, current systems often suffer from mechanically rigid structures, particularly in terms of limited flexibility in adjusting the positional parameters of the two wires, such as the double wire spacing and angle. Furthermore, studies on the metallurgical behavior of double wire narrow gap GMAW, especially when applied to welding dissimilar thick steel plates, remain relatively scarce.

1.4. Deposition for high-strength and low-alloy (HSLA) steel

HSLA steels typically offer advantages such as low manufacturing costs, excellent mechanical properties, and good weldability, and they have been extensively employed in large-scale structural components including engineering machinery, marine engineering structures, and petroleum transportation pipelines[46, 47]. These steels generally contain alloying elements such as Ni, Cr, Mn, and Mo with a total weight percentage below 3 wt%, along with carbon content under 0.2 wt%[48, 49]. As a core material for infrastructure construction, achieving synergistic optimization between exceptional mechanical properties and high deposition efficiency in HSLA deposited metal is critically important.

Performance enhancement remains a persistent research focus. To address diverse

application fields and component structures, various strength-grade wires such as ER70S-6, ER80S-G, ER90S-G, ER100S-G, ER110S-G, and ER120S-G have been developed[50-52]. Furthermore, Tiago A. Rodrigues et al.[53] developed a method for in-situ addition of SiC during the deposition of HSLA steel, effectively enhancing the mechanical properties of fabricated components.

The room-temperature microstructure of HSLA steel with identical composition is strongly dependent on deposition process parameters. Under rapid cooling rates, martensitic microstructures form at room temperature, whereas slower cooling rates produce ferritic or bainitic microstructures[54, 55]. It must be emphasized that even for ferritic microstructures, morphological variations exist under different processing conditions, significantly altering the material's mechanical behavior. Ben Weber et al.[56] investigated the tensile properties of HSLA steel (ER110S-G) structures deposited at different interlayer temperatures (150°C and 350°C), finding that lower interlayer temperatures resulted in faster cooling rates, thereby producing finer grains and higher strength. Li et al.[57] comparatively studied the microstructure and mechanical properties of wire-arc additively manufactured HSLA steel (ER120S-G) at interlayer temperatures of 100°C and 300°C, discovering that lower interlayer holding temperatures facilitated the dispersion of carbides, consequently enhancing yield strength. Fang et al.[58] examined the influence of heat input on the microstructure and mechanical properties of arc-deposited HSLA steel structures (800 MPa grade), revealing that both tensile strength and low-temperature impact toughness of the deposited structures decreased with increasing heat input, correlating with microstructural differences induced by varying heat inputs. Aravind Babu et al.[55] similarly identified the effect of heat input on deposited HSLA steel (LNM MoNiVa), fabricating bulk structures with graded mechanical properties by modulating heat input. Wang et al.[47] conducted post-deposition heat treatment studies on as-deposited HSLA steel (AWS E91T1), demonstrating that tempering or quenching + tempering processes significantly improved the tensile properties and fracture toughness of the deposited metal.

Previous studies show that controlling thermal processes (like heat input and interlayer temperature) and using post-deposition heat treatments can effectively adjust the microstructure and mechanical properties of HSLA steel. However, these strategies struggle to reconcile the fundamental conflict between high deposition efficiency and exceptional mechanical performance: excessive thermal control reduces productivity, while post-deposition heat treatments incur additional energy costs and extend manufacturing cycles. Moreover, multilayer deposition induces thermal accumulation, resulting in heterogeneous microstructures and mechanical properties from the bottom to top layers[59]. Compounding this challenge, current research predominantly focuses on single-wire deposition, leaving significant knowledge gaps in the microstructure-property relationships of double-wire GMA-processed HSLA steel. Furthermore, for thick-sectioned components, the potential of IDT control, an in-situ thermal management strategy requiring neither alloy redesign nor heat input adjustment, remains unexplored.

1.5. Dissimilar steels welding

With the advancement of science, technology, and engineering applications, the performance of traditional mechanical structures or equipment can no longer meet the demands in their respective fields. Moreover, various industries, such as aerospace, impose increasingly stringent requirements on structural and performance characteristics, leading to higher demands on materials themselves or structural designs. However, single materials often fail to meet these requirements. From the perspectives of resource utilization efficiency and economic benefits, the combination of multiple materials can not only deliver superior performance but also help control costs and generate value. The welding of dissimilar metals perfectly fulfills these conditions. By joining different metals, their excellent properties—such as outstanding mechanical performance, corrosion resistance, high-temperature resistance, and wear resistance—can be effectively combined to meet specific needs across various industries[60, 61]. Nevertheless, differences in weldability, chemical composition, and physical properties between the two metals can result in complex residual stress distributions, element

diffusion behaviors, and microstructural characteristics at the bimetallic interface.

The Marangoni effect is a critically important mass transfer phenomenon in which liquid metal flows due to variations in surface tension during the welding process[62]. In dissimilar metal welding, differences in the coefficients of thermal expansion and melting points lead to changes in surface tension at the molten pool interface, thereby affecting the stability of the molten pool and resulting in complex microstructural characteristics at the heterogeneous interface. Zhang et al.[63] observed a complex microstructure in laser-arc hybrid welded joints of low-alloy steel/stainless steel, where the formation of different phases depends on variations in alloy composition, thermal gradients, cooling rates, and elemental diffusion across the welding interface. Chen et al.[64] found significant elemental diffusion behavior at the stainless steel/low-carbon steel heterogeneous interface, specifically manifested as the diffusion of alloy elements such as Cr and Ni from stainless steel to low-carbon steel, while elements like C and Fe diffused from low-carbon steel to stainless steel. This elemental diffusion behavior leads to the formation of a martensitic transition layer at the interface, resulting in non-uniform softening and hardening characteristics, high residual stresses, and a reduction in the corrosion resistance of the stainless steel[65-67]. Secondary phases, which may include various compounds, carbides, or intermetallic compounds, can form due to elemental diffusion and chemical reactions [68, 69]. Inappropriate welding parameters often cause segregation of secondary phases at the heterogeneous interface of dissimilar steel joints, adversely affecting the joint performance[70].

You et al.[71] developed a novel flux-cored wire laser fillet welding technique for joining Q235B and 65Mn dissimilar steels used in mining machinery applications. A comparative study between FCAW and flux-cored laser welding (FCLW) demonstrated that the welding speed of the FCLW process was approximately 1.5 times that of the FCAW process. Furthermore, compared to FCAW specimens, the FCLW specimens exhibited superior shear strength in the load direction on both the Q235B and 65Mn steel sides. Feng et al.[72] investigated the feasibility of using 52M/308L dissimilar wire filler for multi-pass narrow-gap laser welding of SA508/316L dissimilar metals.

They also regulated the microstructure of the welded joint by adjusting the ratio of the 52M/308L dual-wire filler. Zhou et al.[73] studied the regulatory mechanism of a composite magnetic field method (longitudinal magnetic field + pointed magnetic field) on the base metal fusion ratio in Q345/316L dissimilar metal welds. The research found that composite magnetic field-assisted dissimilar steel welding can be used to control the base metal fusion ratio, effectively avoiding defects caused by incomplete weld penetration and significantly improving the quality of dissimilar steel welded components.

The welding of dissimilar joints between medium and thick plates of high-strength low-alloy steels is in substantial demand for engineering machinery applications such as mining equipment, pressure vessels, power plants, and bridges. Particularly for the chute structure of scraper conveyors, their manufacturing process involves the welding of dissimilar high-strength low-alloy steels (NM450 and ZG30SiMn). Although numerous researchers have investigated the metallurgical characteristics and mechanical behavior of dissimilar steel joints, studies focusing on the dissimilar joints in chute structure remain relatively limited. The present research on dissimilar steel double wire narrow gap GMAW plays a crucial role in enhancing the manufacturing capability and structural quality of chute structures

1.6. Wire arc cladding for enhancement in wear resistance

In the field of engineering, surface friction damage represents one of the most prevalent failure modes. Replacing entire damaged components not only escalates economic costs but also prolongs production cycles. Consequently, implementing localized repairs on affected surfaces or applying a preemptive wear-resistant coating prior to formal production can significantly mitigate failure risks while enhancing operational efficiency. This approach offers substantial advantages in terms of both cost-effectiveness and process optimization, making it a strategically valuable solution for industrial applications[74, 75].

Conventional surface treatment approaches typically employ welding technologies to fabricate cladding layers on target surfaces. Aslam et al.[76] successfully deposited

a 304 stainless steel coating on mild steel using tungsten inert gas (TIG) welding, leveraging the alloy's high chromium (Cr, 18-20 wt.%) and nickel (Ni, 8-10 wt.%) content to enhance surface hardness from 177 $HV_{0.5}$ to 335 $HV_{0.5}$, while simultaneously reducing the average wear depth from 146 μm to 57 μm. In a comparable study, Wang et al.[77] applied Fe105 powder containing approximately 17 wt.% Cr onto QT500-7 ductile iron substrates. Through optimized processing parameters, they achieved crack-free deposition with a 30% dilution ratio, resulting in a remarkable 103% improvement in surface hardness from 208.5 $HV_{0.2}$ to 424.2 $HV_{0.2}$. Zhang et al.[78] utilized an Fe-based powder containing 6.2 wt.% Cr and 6.3 wt.% V as wear-resistant material, achieving an exceptional surface hardness of 823.6 $HV_{0.025}$ — representing a 3.9-time increase over the base material hardness. This treatment also produced a dramatic two-order-of-magnitude reduction in wear rate, decreasing from 1.03×10^{-6} $mm^3/(N\cdot m)$ to 2.22×10^{-8} $mm^3/(N\cdot m)$.

The aforementioned methods primarily focus on enhancing hardness through selecting appropriate cladding materials to mitigate surface damage. Liu et al.[79] have demonstrated that post-treatment processes can further optimize wear resistance. They employed a low-temperature plasma nitriding process to post-treat AISI 316L cladding layers, achieving remarkable improvements in both surface hardness and wear performance. Their results showed that the nitriding treatment not only reduced the friction coefficient but also decreased the wear rate from 2.31×10^{-5} $mm^3/(N\cdot m)$ to 1.61×10^{-7} $mm^3/(N\cdot m)$. More significantly, the treatment induced a transformation in the dominant wear mechanism from abrasive and adhesive wear to oxidative and adhesive wear. Moreover, advanced modification of cladding material composition through the incorporation of non-metallic elements such as boron (B) can significantly enhance wear resistance by promoting the formation of additional hard phases within the cladding layer. Santana et al.[80] demonstrated this approach by employing B-enhanced Fe-based powder as cladding material on mild steel substrates. Their microstructural analysis revealed an α-(Fe, Cr) solid solution matrix containing numerous micron- and nano-scale (Fe, Cr)NbB and M2B (M=Cr, Fe) boride precipitates, which collectively

improved the wear resistance of the mild steel substrate by approximately tenfold. Further studies have shown that B addition to Fe-Cr-C alloys not only facilitated the formation of various boride phases (Fe2B, CrB2, Fe23B6, Cr5B3)[81], thereby increasing both the variety and quantity of hard phases, but also promoted the nucleation of primary Cr7C3 carbides while refining their grain size. This dual effect enabled the achievement of cladding layer hardness exceeding 1000 HV_{10}[82, 83]. However, it should be noted that excessive formation of these borides and carbides may lead to their network-like distribution within the matrix. While such microstructure demonstrated excellent wear resistance under relatively low loads (< 20 N), it became problematic under higher stress conditions (> 25 N) where these hard phases may act as stress concentration sites and initiate crack formation[84]. This phenomenon highlights the importance of optimizing hard phase content and distribution to balance wear resistance and mechanical integrity under varying service conditions, presenting a critical consideration for the design of advanced wear-resistant coatings in practical engineering applications.

Recent studies have revealed that the incorporation of nanoscale TiC particles produces multifaceted improvements in cladding layer performance. Beyond promoting equiaxed grain formation and microstructure refinement, these ceramic additions simultaneously enhanced hardness and Young's modulus, thereby improving both resistance to plastic deformation and elastic recovery capability[85-87]. Despite under severe loading conditions (100 N), TiC-reinforced coatings demonstrated a 5.4-time increase in hardness over the Q345C substrate[88], a 50% reduction in friction coefficient and a 40% decrease in mass loss compared to unreinforced counterparts[89]. Reinforcement with SiC particles induced formation of additional intermetallic phases including CrSi2 and Mn3Ni2Si alongside conventional carbides (Fe2C, Fe5C2, Cr7C3), resulting in remarkable 8.7-fold and 1.7-fold improvements in adhesive wear resistance and abrasive wear resistance for mild steel base materials, respectively[90]. WC particle addition similarly functioned as effective heterogeneous nucleation sites, facilitating columnar-to-equiaxed transition and grain refinement. While optimal WC content (30

wt.%) enhanced both impact resistance and sliding wear resistance, excessive addition (> 40 wt.%) tended to induce crack initiation due to increased brittleness[91, 92].

The research findings reveal important trade-offs in wear-resistant coating design. While alloying elements and ceramic particles can effectively increase hard phase content, these inherently brittle compounds may cause interfacial mismatch and crack initiation when present in excessive quantities[93]. Furthermore, the powder-based alloy modification approach, despite its compositional flexibility, faces inherent limitations including poor coating density, porosity formation[94, 95], and particle agglomeration/flotation issues that compromise microstructural homogeneity[89]. In contrast, wire-based Fe-Cr-C cladding offers distinct advantages through its simpler processing, higher coating density, and cost-effectiveness — factors that have made this system particularly attractive for industrial applications[96]. The wear resistance of Fe-Cr-C coatings primarily stems from M7C3 and M23C6 carbides (where M represents Cr and Fe), with their relative proportions being strongly composition-dependent. At lower carbon concentrations (1-3 wt.%), M23C6 predominates, while higher carbon levels (5-6 wt.%) favor M7C3 formation[97, 98]. Cr content plays a dual role: while it promotes carbide formation, excessive Cr (≥ 25 wt.%) leads to coarse primary carbides with reduced toughness that paradoxically diminish wear resistance[99]. The study by reference[100] further highlights that the high contents of Cr and C can trigger excessive hard phase formation, generating internal stresses that promote cracking and weaken coating-substrate bonding. These findings underscore the importance of balanced alloy design in Fe-Cr-C systems, where optimal wear performance requires careful control of both carbide volume fraction and morphology to achieve the desired combination of hardness and fracture resistance.

1.7. Numerical simulation for temperature field during GMAW

Issues such as deformation around the weld joint, residual stresses, and reduced mechanical strength have attracted significant attention. These problems directly stem from the thermal cycles induced by the intense heat input characteristic of fusion

welding[101]. The high temperatures generated by the heat source cause notable metallurgical damage and alterations in the region surrounding the weld zone. The heat flux in welding represents the time-dependent area where the arc interacts with the workpiece. However, quantitatively analyzing the temperature field proves highly challenging. Consequently, numerical simulation has emerged as a powerful tool for predicting the characteristics of the welding temperature field[102].The selection of appropriate process parameters and the resulting weld bead geometry determine the quality of the welded joint. Predictive factors during welding, such as the fusion zone, heat-affected zone, and transient temperature distribution, have consistently been the focus of extensive research. Investigating the welding temperature field is crucial for clarifying the thermal effects of the welding process, thereby reducing experimental time and optimizing welding procedures. Furthermore, the thermal process in welding often influences complex metallurgical and mechanical responses. Obtaining the thermal cycle curve of the welding process is also essential for establishing the process-structure-property relationship.

The Finite Element Method (FEM) has demonstrated its potential and reliability in solving various mathematical problems, particularly in the fields of heat transfer and welding simulation. Currently, mainstream software for temperature field simulation includes Abaqus[103], Simufact Welding[104], Sysweld[105], Marc[106], and Ansys[12], among others. Some of these commercial software packages offer dedicated modules for welding simulation, while others require engineers to program the thermal processes and mechanical behaviors. Overall, these commercial tools can effectively support practical engineering applications. In addition to large-scale commercial software, many researchers are committed to developing new software tailored for welding simulation, which offers certain advantages in terms of simulation accuracy and computational speed.

Xiong et al.[107] investigated the thermal behavior in GMAW-based additive manufacturing using finite element analysis. The simulated thermal cycle curves showed good agreement with experimental results. The validated model was employed

to study the influence of substrate preheating on thermal behavior. Amir Dadkhah et al.[108] evaluated the effect of heat input on residual stresses during GMAW through integrated simulation and hole-drilling measurements. The numerical simulation utilized Abaqus with Goldak's double ellipsoidal heat source model and the element birth and death technique. Aquiles S. Schauenberg et al.[103] developed a novel application using the finite element method and Abaqus software to predict thermal gradients induced by GMAW in T-joints. This more comprehensive approach reduced computational processing time while providing more accurate results for the fusion zone and heat-affected zone. Feng et al.[109] proposed a Newton-Raphson Method (NRM) that avoids calculating inverse matrices and a hybrid approach combining NRM with conventional implicit methods (IMP). The developed software demonstrated faster computation speed and higher efficiency compared to commercial software while maintaining computational accuracy. Ding et al.[110] revealed that the peak temperature experienced during the thermal cycle in WAAM determines the residual stress at a given point. Based on this finding, an efficient "engineering" finite element model was developed. This model achieved a 99% reduction in computational time compared to traditional transient thermomechanical methods, while producing residual strain and stress predictions nearly identical to those of the original transient model and experimental results.

In the double-wire narrow GMAW process, multi-layer deposition inevitably leads to complex temperature field characteristics, thereby resulting in intricate phase transformation behaviors in the welded joint. Therefore, it is essential to employ the finite element method for thermal modeling of the double-wire narrow GMAW process.

1.8. Purpose and outline

while double-wire narrow gap welding has been applied to thick-plate homogeneous materials, its application to chute structures remains unreported. Current chute manufacturing relies on single-wire methods[3]. Chute structures, composed of two thick-plate steels, involve dissimilar metal welding: the base metals (NM450 and ZG30SiMn) and the welding wire (ER70-G). Dissimilar materials welding inherently

presents challenges such as chemical element diffusion, mismatched mechanical properties, and non-uniform residual stress distribution, particularly when significant disparities exist in material properties[4, 73, 111]. These issues can lead to degradation of structural service life. Furthermore, operational failures of chute structures frequently arise from insufficient toughness in welded joints. Current research evaluating the metallurgical characteristics and mechanical properties of welded joints in chute structures remains limited. Thus, a comprehensive evaluation of double-wire narrow gap welding's process compatibility, along with the microstructure and mechanical properties of the joints, is essential.

Furthermore, existing research on surface strengthening has primarily focused on improving the wear resistance of homogeneous materials. However, actual engineering components are often composed of multiple material systems, such as the chute structure of a scraper conveyor. The interfaces between these different materials frequently undergo severe chain wear, leading to inevitable surface degradation. This highlights a critical research gap in addressing the wear behavior at the interfaces of heterogeneous materials.

To address the aforementioned scientific and engineering challenges, this study conducts a comprehensive investigation involving the fabrication and strengthening of heterogeneous joints in chute structures, as show in Fig.1.5. The research is divided into six chapters.

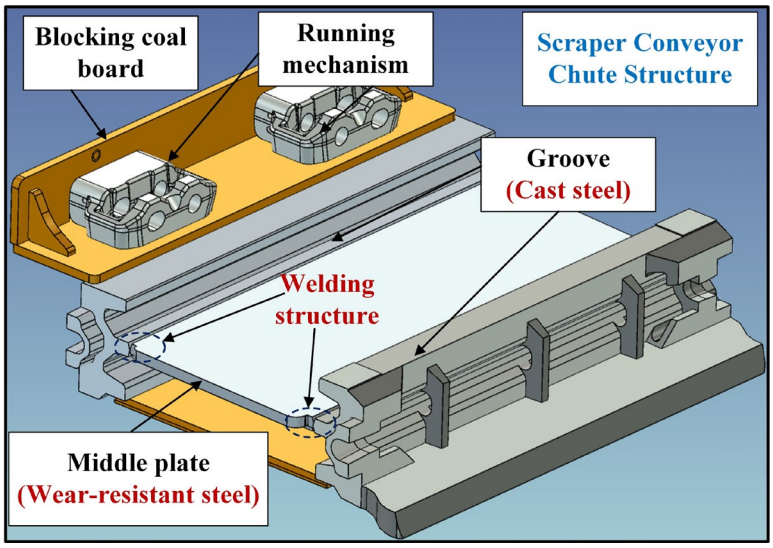


Fig. 1.5. Schematic diagram of the chute structure

Chapter 1: This chapter introduces the research background, significance, and the current state of research both domestically and internationally. It covers the definition, challenges, and classification of narrow-gap welding. Particular emphasis is placed on comparing single wire narrow gap GMAW with double wire narrow gap GMAW. The current status of high-strength low-alloy steel deposition is also elaborated, which relates to the study of weld metal in Chapters 3 and 4. As this research involves the welding of dissimilar high-strength steels, the current state of research on dissimilar steels is also discussed. Furthermore, the study summarizes existing research on wire arc surface strengthening. Additionally, the author reviews the current state of numerical simulation research in GMAW.

Chapter 2: This chapter focuses on the optimization of the double wire narrow gap welding process. In narrow gap welding, arc and droplet transfer characteristics are crucial for evaluating welding stability and quality. By optimizing process parameters, including wire feed speed, welding speed, and double-wire spacing, the author obtained process parameters suitable for narrow gap welding. This is significant for subsequent research and practical engineering applications.

Chapter 3: This section investigates the microstructure and mechanical properties of the filler metal (ER70-G). The author proposes a strategy using interlayer dwell time control to regulate the microstructure and mechanical properties of the deposited metal, achieving a synergistic improvement in strength and toughness. Furthermore, this study establishes a process-microstructure-property relationship model, which provides a valuable reference for research on high-strength low-alloy steels.

Chapter 4: This chapter provides a comprehensive evaluation of the microstructure and mechanical properties of narrow gap welded joints of dissimilar thick-plate steels, including both the filler metal and the heat-affected zone. Additionally, this section describes the evolution behavior of the microstructure in narrow-gap joints under thermal cycling. This is of great significance for studying the metallurgical characteristics of trough structures.

Chapter 5: The research objectives include characterizing dilution ratio level and

microstructure evolution across material boundaries, evaluating hardness gradients and their correlation with wear performance. This work seeks to establish fundamental principles for wear resistance control in complex multi-material components. The findings are expected to provide valuable insights for surface engineering of critical industrial equipment where dissimilar material joining is unavoidable.

Chapter 6: This chapter summarizes the key conclusions of this study and outlines directions for future research.

Fig. 1.6 presents the research roadmap of this study. The six chapters are structured in a progressive and interconnected manner, each building upon and complementing the others.

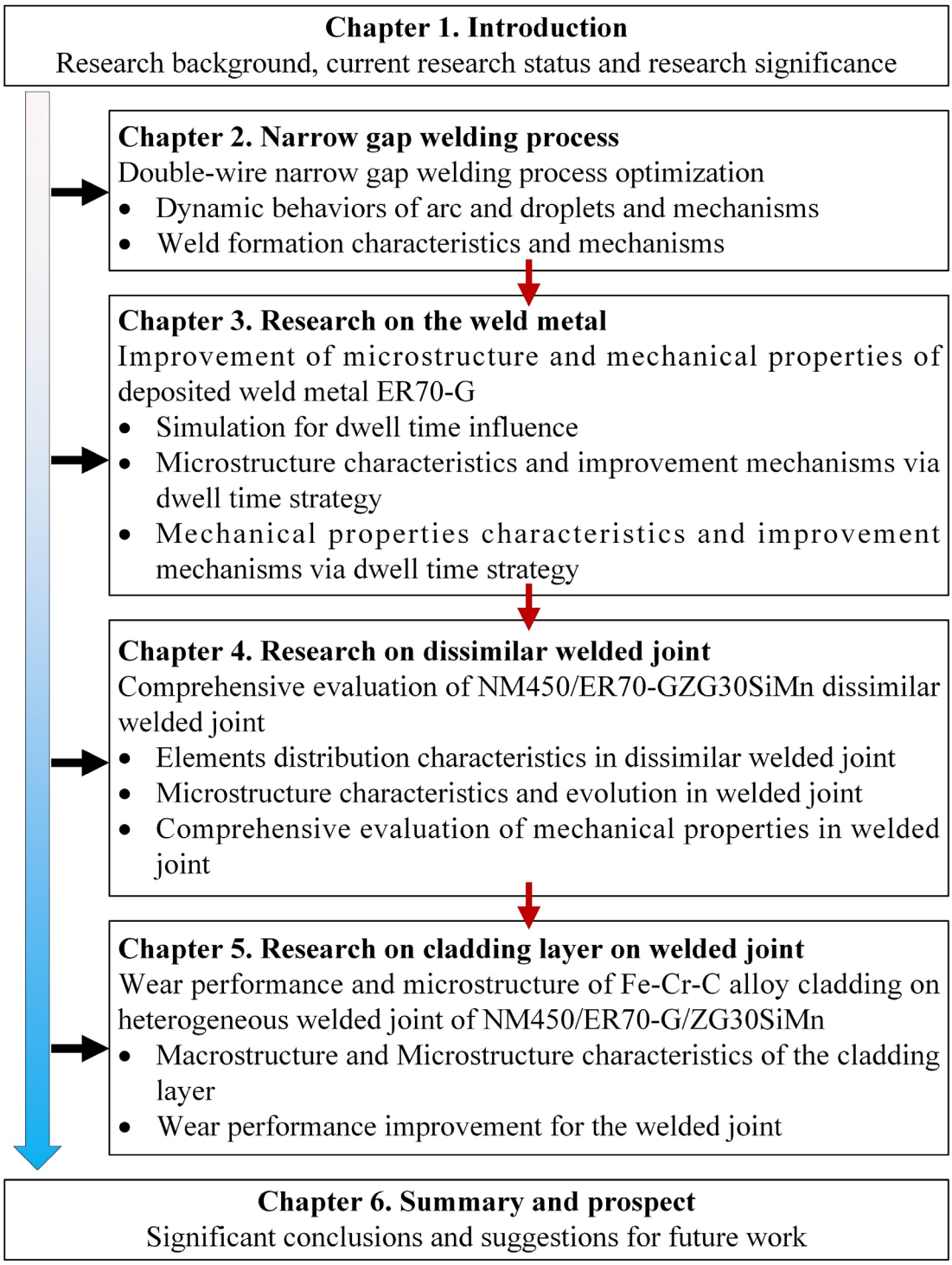


Fig. 1.6. Research roadmap of this study.

Chapter 2. Double-wire narrow gap welding process optimization

2.1. Research purpose and process conditions

2.1.1 Research purpose

Most of the current research focuses on the influence of a single parameter on welding. This research aims to investigate double-wire GMAW for the narrow-gap welding of low-alloy steel, systematically studying the welding process and weld formation and establishing the influence relationship between them. The findings of this study will enrich the understanding of narrow-gap welding processes and promote the practical application of double-wire narrow-gap GMAW in industrial settings, contributing to advancements in welding technology and practices.

2.1.2 Welding setup and materials

To achieve the high-efficiency narrow-gap welding of thick-walled structures, a double-wire GMAW system was employed in this study, as depicted in Fig. 2.1(a). The welding system consisted of a six-axis robot, a double-wire GMAW torch, two welding power sources, two wire feeders, and two bottles of shielding gas of 80% Ar and 20% CO_2. It is worth noting that the double-wire welding torch used in this study is composed of two single-wire welding torches. Two welding wires pass through these two single-wire welding torches, with process parameters controlled by two welding power sources. Constant voltage mode was used during welding, and both welding wires were melted simultaneously. The gas flow rate for both welding torches was set to 20 L/min to obtain a good protection effect. The hybrid torch was fixed on the six-axis robot to achieve the movement. The welding direction was along the X-axis. Figure 1(b) shows the projection of two wires on the ZX plane and ZY plane, clearly indicating the arrangement of the double wire. Along the welding direction, the two wires were arranged in front of one another, and they were tilted with an angle of 10° from the vertical direction. The distance between the ends of the two wires was 10 mm (under the condition of wire extension of 25 mm), and the distance between the ends of the welding wires and the substrate was 1 mm. It is worth noting that the two wires were

flexible in the direction perpendicular to the welding direction. The wires could be rotated around the X-axis, and the distance between the ends of the two wires varied from 0 mm to 8 mm (under the condition of constant wire extension of 25 mm).

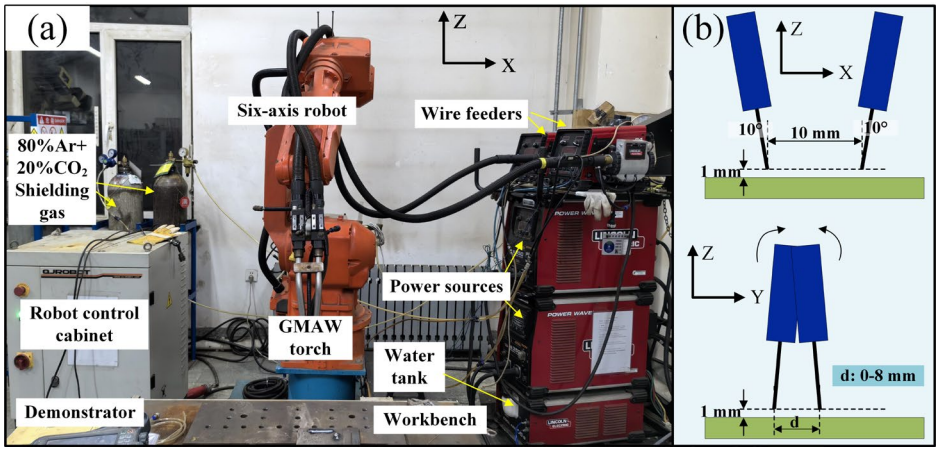


Fig. 2.1. (a) Double-wire narrow-gap GMAW system and (b) arrangement of the double wire.

The base material used in the welding processes was Q235, and the welding wire was ER70-G. The chemical compositions of the materials are shown in Table 2.1.

Table 2.1. Chemical composition of materials used in this work (wt.%)

Materials	C	Si	Mn	Cr	Ni	Mo	Fe
ER70-G	0.10	0.30	1.45	0.3	1.7	0.35	Bal.
Q235	0.22	0.23	0.56	-	-	-	Bal.

2.1.3 Welding parameters

In order to obtain suitable process parameters for narrow-gap welding, welding was first conducted on the Q235 substrate with a thickness of 10 mm to study the arc shape, droplet transition mode, and current–voltage waveforms. Firstly, welding experiments were conducted on a flat plate through single-wire welding using the parameters shown in Table 2.2, and the welding voltage was automatically matched with that of the welding power source. Then, double-wire welding was conducted using the optimized wire feeding speed. As shown in Fig. 2.2, a high-speed camera (OLYMPUS I-SPEED, Woburn, MA, USA) was used to capture the behavior of the arc and droplet transfer during the welding process. The camera was placed perpendicularly to the welding direction, and the camera frame rate and exposure time were 2000 fps and 2 μs, respectively. Simultaneously, an electrical signal acquisition device was used to collect

the current–voltage waveforms of the arc during welding. The electrical signal data of two arcs were collected simultaneously, with a sampling frequency of 1000 Hz. The information collected during the welding process was processed and analyzed to study the stability of the welding process and the interaction behavior between the double arcs.

Table 2.2. parameters for the single-wire welding process.

Group	Welding speed (mm/s)	Wire feeding speed (m/min)	Wire extension (mm)
1	8	5	25
2		6	
3		7	
4		8	

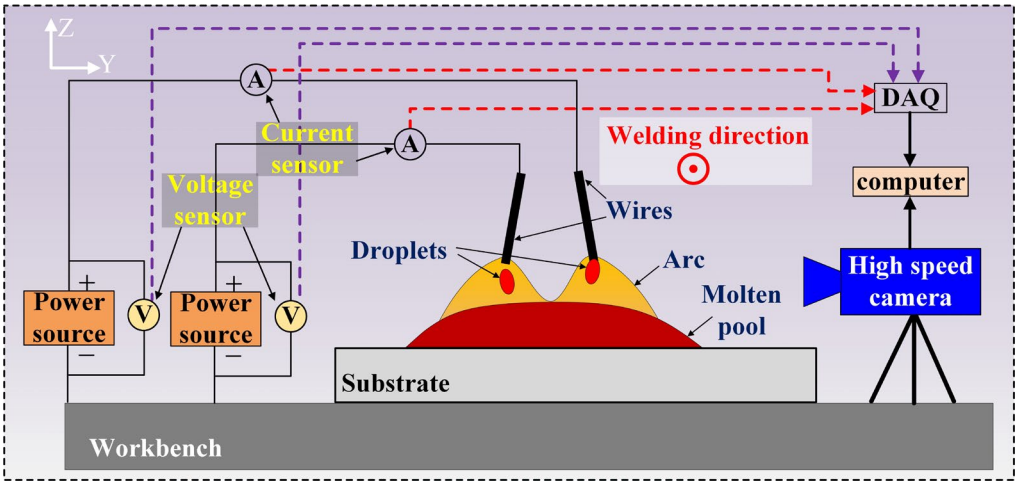


Fig. 2.2. Schematic diagram od welding process on plates.

Subsequently, narrow-gap groove filling was conducted using the double-wire welding process. The welded assembly comprised a narrow-gap groove with a width of 12 mm, which was created by joining two 30 mm thick steel plates as sidewalls with a 10 mm thick steel plate as substrate, as illustrated in Fig. 2.3(a) and (c). During the welding, changes were made to parameters such as the welding speed and double-wire lateral spacing at the wire feeding speed of 8 m/min for the front and back wires. The detailed parameters are shown in Table 2.3. The arc and droplet transition behavior under different double-wire lateral spacing were photographed, as shown in Fig. 2.3(b). After single-pass filling welding was completed, metallographic samples were taken using wire electrical discharge, and the samples' cross-section was polished

sequentially with 80# and 400# sandpaper and then etched with a nitric acid–alcohol solution. Data on various factors such as the welding width, filling height, and bottom fusion depth from the cross-section morphology of the weld bead were extracted to study the influence of the welding process on the formation of weld seams and defects.

Table 2.3. parameters for the double-wire welding process.

Group	Welding speed (mm/s)	Double-wire lateral spacing (mm)	Wire extension (mm)
1	5	0	25
2	8		
3	11		
4	14		
5	8	2	
6		4	
7		6	
8		8	

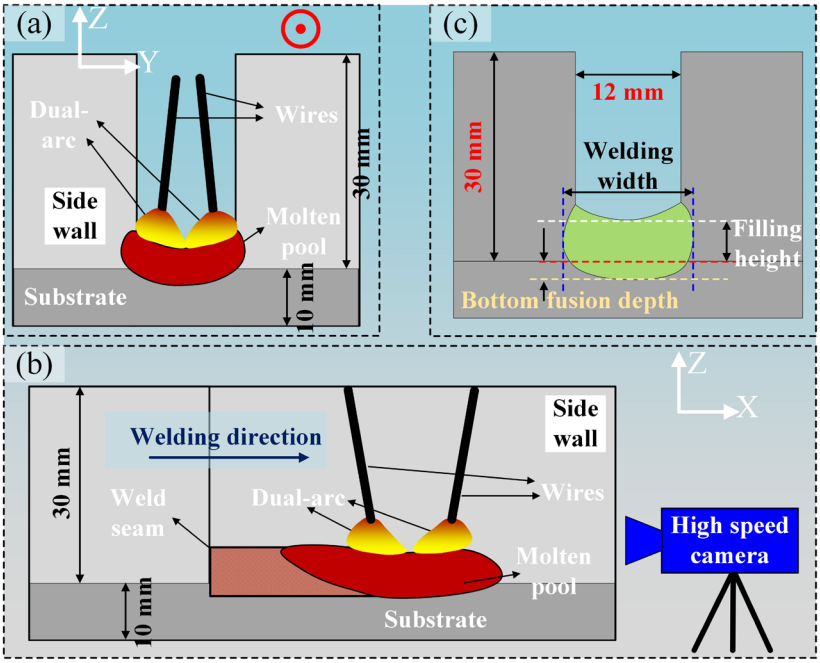


Fig. 2.3. Schematic diagram of (a, b) welding process in the narrow-gap groove and (c) measurement of the weld bead.

2.2. Dynamic behaviors of arc and droplets and their generation mechanism in single-wire welding

The photos captured under different wire feeding speeds are shown in Fig. 2.4. It can be observed that as the wire feeding speed increases, the arc becomes larger and brighter.

The corresponding current–voltage waveforms in Fig. 2.5 indicate that as the wire feeding speed increases, both the welding current and voltage increase.

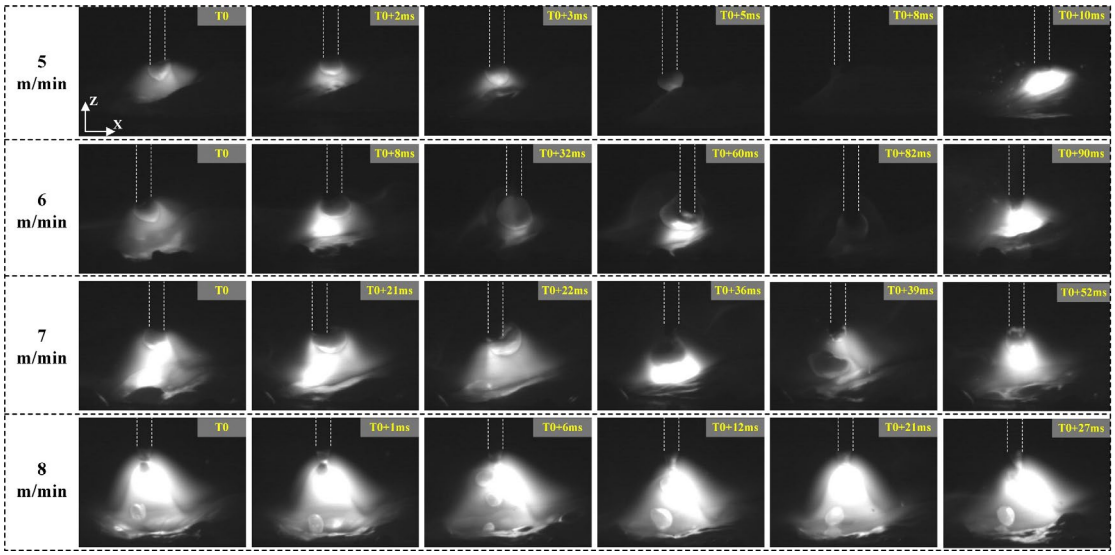


Fig. 2.4. Arc and droplet behaviors under different wire feeding speeds (5 m/min, 6 m/min, 7 m/min, and 8 m/min) from side view.

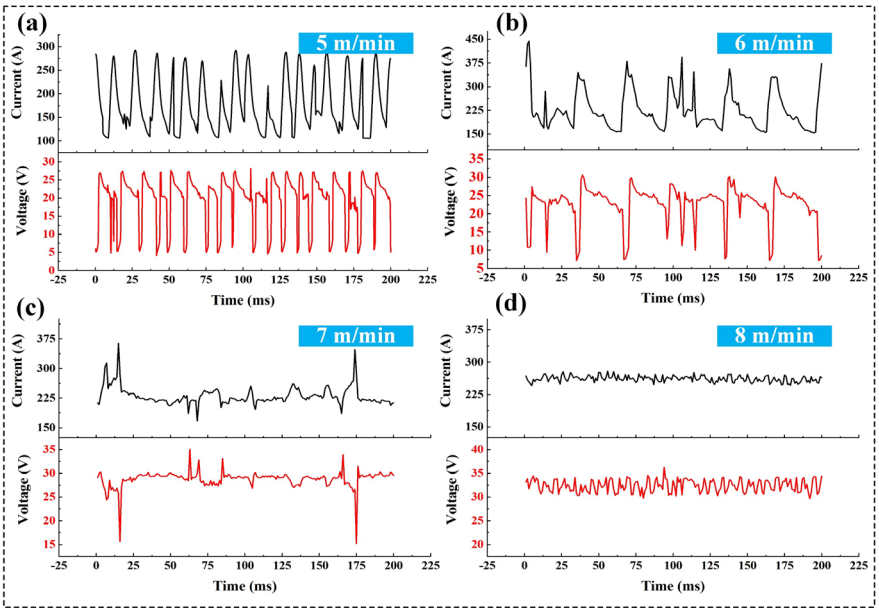


Fig. 2.5. Current–voltage waveforms under different wire feeding speeds: (a) 5 m/min; (b) 6 m/min; (c) 7 m/min; (d) 8 m/min.

At a wire feeding speed of 5 m/min, the wire end melts, and the droplet grows continuously. Due to the lower voltage, when the droplet grows to a certain size and touches the molten pool, the arc diminishes. At this moment, the voltage is at a

minimum, while the current is at a maximum. Subsequently, the arc spikes again, the voltage increases, and the current decreases (shown in Fig. 2.5(a)). The droplet at the wire end transitions to the molten pool in this periodic short-circuit manner. The increased wire feeding speed to 6 m/min maintains the short-circuit transition mode for the droplet. However, due to the higher voltage at this speed compared to that of 5 m/min, the droplet grows continuously before contacting the molten pool, with a larger volume than at 5 m/min. Moreover, the droplet at the wire end receives resistance from the anode spot, hindering its transition behavior, which also results in a larger droplet size and increased transition periods. The current–voltage waveforms in Fig. 2.5(b) clearly show the elongation of the droplet transition period. When the wire feeding speed increases to 7 m/min, the welding current and voltage further increase, causing the wire end to melt and grow. Although the droplet is still hindered by the anode spot, when it reaches a sufficient size, it detaches from the wire end and transitions to the molten pool. However, Fig. 2.5(c) shows that the droplet transition behavior at this speed was unstable. When the wire feeding speed reaches 8 m/min, the welding current and voltage are high enough for the wire to melt significantly, resulting in a pointed shape at the wire end, and the droplet with a diameter close to the diameter of the wire transitions to the weld pool in a spray-like manner. Fig. 2.5(d) demonstrates stable current–voltage waveforms, indicating a consistent spray transition mode at this parameter.

2.3. Dynamic behaviors of arc and droplets in double-wire welding and spacing influence

In order to ensure the successful progress of the narrow-gap welding, sufficient heat input must be provided to fill the narrow-gap groove without causing the defect of lack of fusion on the sidewalls. It is also necessary to adopt stable welding process parameters to ensure the stability of the welding operation. Therefore, the wire feeding speed of 8 m/min seems to be a very suitable process parameter. Subsequently, a welding experiment was conducted on the Q235 plate using double-wire welding. Both the wires were at a wire feeding speed of 8 m/min, and the welding voltage was

automatically set to 32.5 V using the welding power source. Fig. 2.6 shows the transition behavior of the arcs and droplets during the double-wire welding process, varying the double-wire spacing from 30 mm to 10 mm. At a wire feeding speed of 8 m/min, the droplets from the two wires transitioned to the molten pool in a spray manner. When the two welding wires are spaced far apart (30mm), they melt to form two separate molten pools. When the spacing between the two welding wires is reduced (<20mm), they melt to form a common molten pool. It is also worth noting that the two arcs attract each other, causing arc deflection.

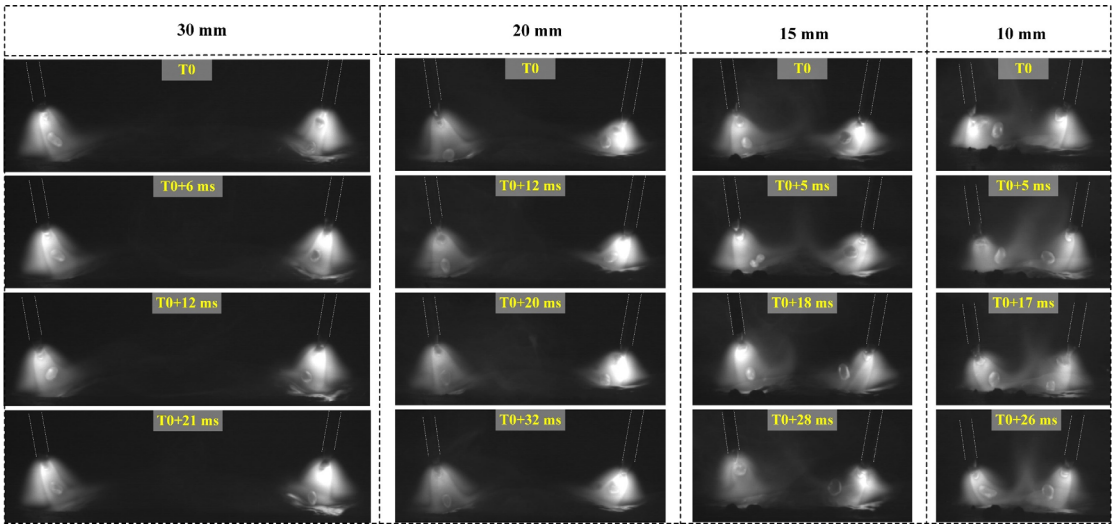


Fig. 2.6. The behaviors of double-wire arcs and droplets at a wire feeding speed of 8 m/min from side view.

The deflection angles of the two arcs (relative to the welding wires) were measured. The measurement method and results are shown in Fig. 2.7(a) and (b). The results indicate that the two arcs attract each other, manifested as the deflection angle of the arcs being greater than that of the welding wires. Moreover, as the twin-wire spacing decreases, the deflection angle of the arcs increases.

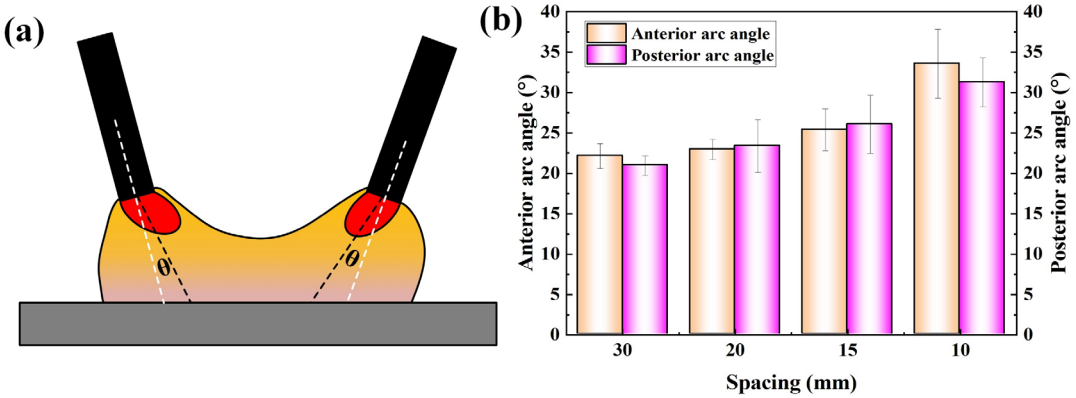


Fig. 2.7. (a) Schematic diagram of the arc deflection angle measurement, (b) Measurement results of the arc deflection angles.

In the double-wire welding process, the interference between the two arcs is the main factor affecting the stability of the welding process. However, in this study, no impact on welding stability was observed, as evidenced by the current–voltage waveforms shown in Fig. 2.8. The stability of the double-wire welding process may be attributed to the self-regulating function of the welding power source.

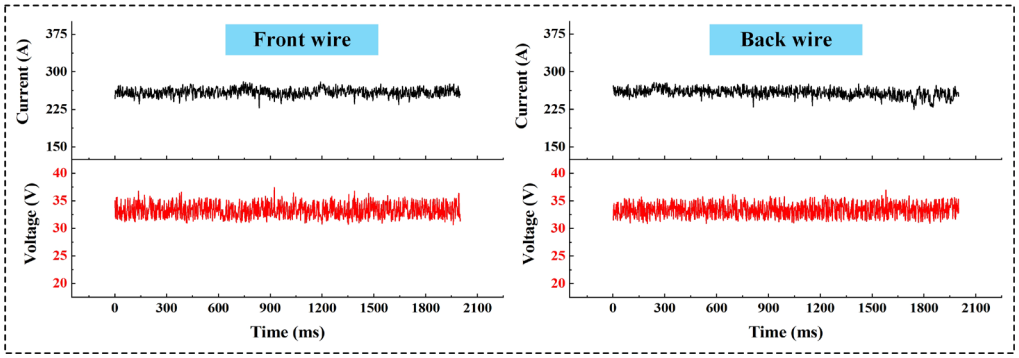


Fig. 2.8. Current–voltage waveforms during the double-wire welding process.

It is worth noting that during the double-wire welding process, the two arcs attract each other, resulting in a noticeable arc deflection. Additionally, the droplets exhibit a movement toward the center between the two arcs. This is the result of the interaction of magnetic fields produced by the two wires. During welding, the welding power sources are connected in a circuit with the wires and the workbench, with the current flowing from the wires through the arc to the workbench. Fig. 2.9 illustrates the behavior of the arcs and droplets in the magnetic field during the double-wire welding process. The red and blue symbols in the figure represent the magnetic field distribution

of the front and back wires, respectively. Additionally, the cross marks symbolize the direction perpendicular to the page inward, and the dot marks symbolize the direction perpendicular to the page outward. The plasma is ultimately deflected due to the action of the Lorentz force. The droplets detached from the end of the wires under the action of the electromagnetic pinch force (Fem), plasma flow force (Fd), gravity (G), frictional force (Ff), surface tension (Fγ), metal vapor recoil force (FJ), and Lorentz force (FL)[112, 113]As the resultant force on the droplets does not align with the axis of the welding wire, the droplets ultimately transition toward the center of the molten pool.

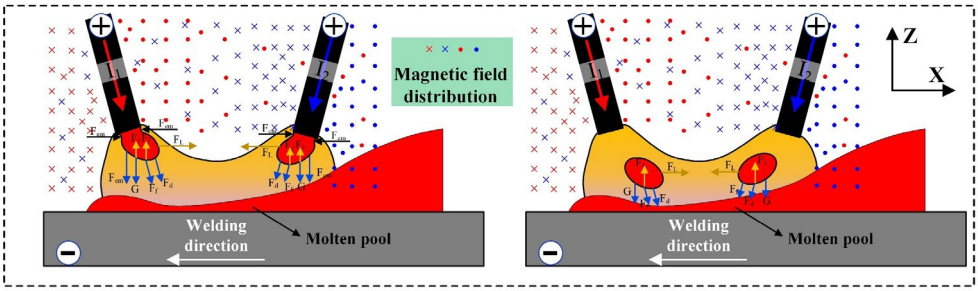


Fig. 2.9. Force analysis of the droplet transition during the double-wire welding process.

The images captured with a high-speed camera, as illustrated in Fig. 2.10, display the behaviors of the arc and droplets under varying lateral distances at a welding speed of 11 mm/s. At a lateral spacing of 0 mm between the double wires, the arc is confined to a small area within the narrow-gap groove, primarily concentrated in the center. The droplets transition to the molten pool via a spray transition method. As the lateral spacing of the double wires increases, the arc's influence expands gradually from the center of the groove to encompass the entire groove, resulting in varying distributions of the temperature field. When the spacing reaches 8 mm, the arc begins to interact with the side walls of the narrow-gap groove. Notably, the mode of droplet transition remains unchanged across different lateral spacings, consistently exhibiting a spray transition. It is evident that the droplets do not migrate to the molten pool along the wires; instead, they show a tendency to move toward the center of the molten pool.

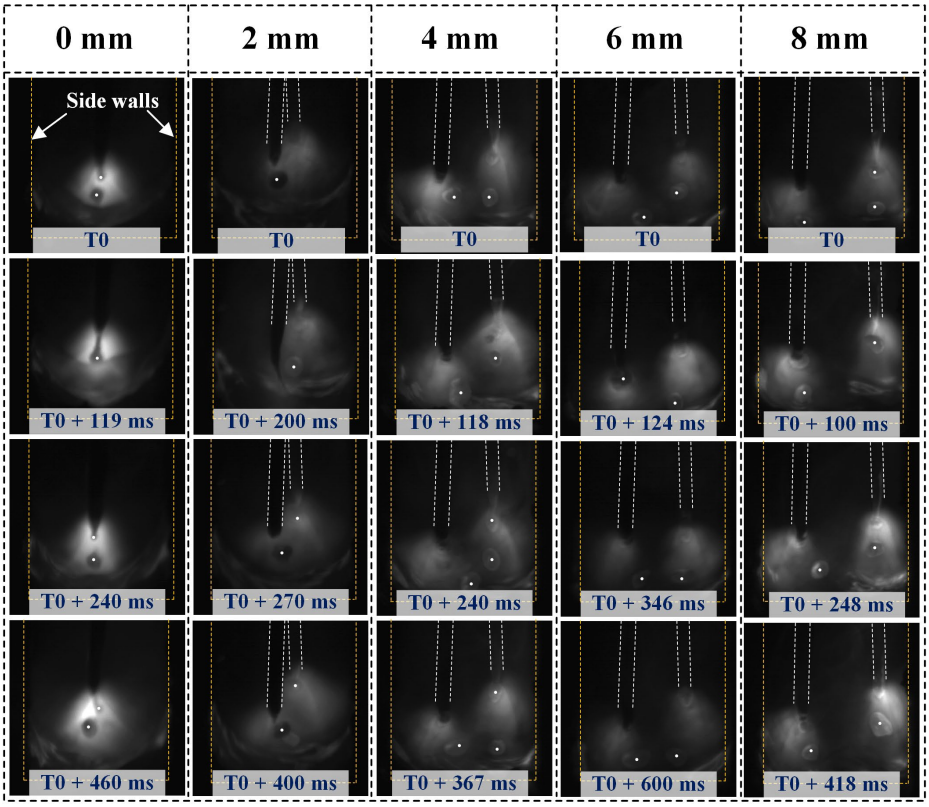


Fig. 2.10. Arc and droplet behavior under different lateral spacings (0 mm, 2 mm, 4 mm, 6 mm, and 8 mm) at a welding speed of 11 mm/s from the front view.

2.4. Weld formation in double-wire welding and spacing influence

Using the process parameters described above for narrow-gap welding, a wire feeding speed of 8 m/min was adopted for the two wires in the subsequent welding process. Initially, experiments were conducted without a double-wire lateral distance, meaning the two wires were in the same plane. Fig. 2.11 displays the weld seam formation and cross-sectional morphology under different welding speeds. It is clear from an overhead view that as welding speed increases, the scale-like patterns on the weld seam surface become denser. At welding speeds of 5 mm/s and 8 mm/s, the weld seam surface appears aesthetically pleasing. However, at higher welding speeds of 11 mm/s and 14 mm/s, insufficient heat input leads to the poor wettability of the filling metal on the sidewalls. The cross-sectional morphology clearly illustrates the weld seam. At a welding speed of 5 mm/s, with higher heat input and more filling metal deposition, an undercut is observed, and the defect of lack of fusion at the groove root corner occurs. Decreasing heat input may contribute to suppressing undercut defects,

but inadequate heat input will lead to the defect of lack of fusion on the sidewalls. Measuring was conducted on the filling height and welding width of the weld seam, with the results shown in Fig. 2.12. As the welding speed increases from 5 mm/s to 14 mm/s, the filling height of the weld seam is reduced from 7.7 mm to 2.5 mm, and the welding width is reduced from 14.6 mm to 11.3 mm.

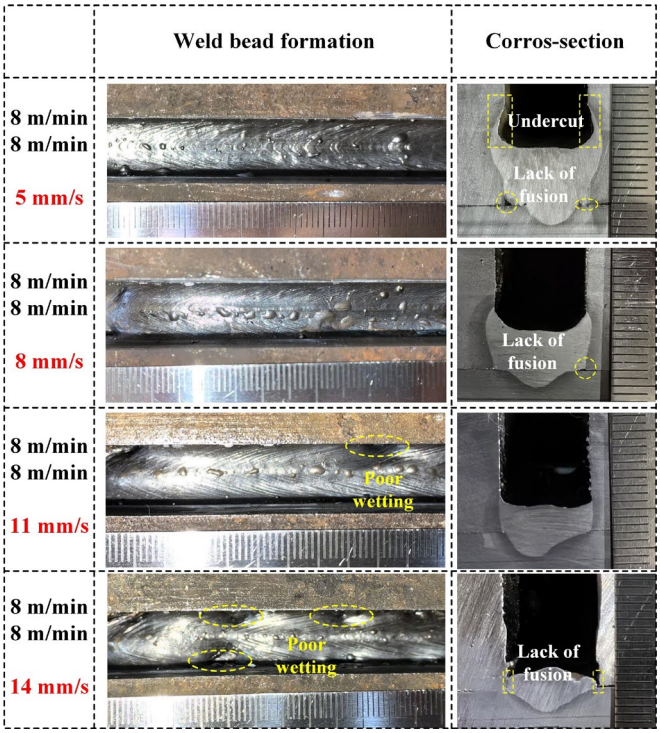


Fig. 2.11. Weld bead formation and cross-section under different welding speeds (5 mm/s, 8 mm/s, 11 mm/s, and 14 mm/s) at a wire feeding speed of 8 m/min for the double wires.

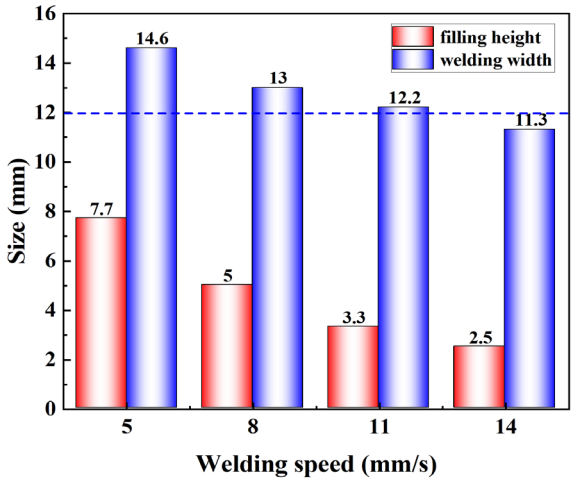


Fig. 2.12. Measurement results of the weld bead section.

Although undercut defects and lack of fusion on the sidewalls can be avoided at welding speeds of 8 mm/s and 11 mm/s, lack of fusion at the groove root corner and poor sidewall wettability may occur. This may result from the two wires being in the same plane, causing heat concentration at the center of the groove. If the two wires are angled laterally with each wire pointing toward a side wall of the groove, the temperature field distribution within the groove may be improved, potentially improving weld seam formation. The welding torch was then adjusted so that the two wires would have a certain lateral spacing. Experiments were conducted with different lateral distances between the two wires at welding speeds of 8 mm/s and 11 mm/s.

Fig. 2.13(a) and (b) illustrate the weld seam formation and cross-sectional morphology obtained under different lateral wire distances at welding speeds of 8 mm/s and 11 mm/s, respectively. It can be seen that with the presence of an angle between the two wires, the weld seam is well formed. When the welding speed is 11 mm/s, there is no poor wetting condition observed. Compared to the situation where the two wires are not angled, the presence of lateral spacing between the two wires effectively improves the weld seam formation, specifically manifested in an improvement in the weld seam cross-sectional morphology. The presence of lateral spacing between the two wires will effectively improve the temperature field inside the narrow-gap groove, allowing more heat to be utilized on both sides of the groove. As the lateral spacing between the two wires increases, the weld seam cross-section gradually becomes more rounded, and the shape of the fusion depth at the bottom of the groove changes from finger-like to bowl-shaped. Additionally, as the lateral spacing between the two wires increases, the welding width of the weld seam increases, and the bottom fusion depth decreases. However, when the lateral spacing between the two wires becomes too large, it can lead to undercut defects, a phenomenon observed at welding speeds of both 8 mm/s and 11 mm/s. Fig. 2.1(4)a and (b) show the specific information on the weld seam size under different lateral spacing conditions at welding speeds of 8 mm/s and 11 mm/s, respectively, which clearly demonstrate regular shapes. When the welding speed is 8 mm/s, the bottom fusion depth of the weld seam decreases from 2.5 mm to 1.7 mm, and

the welding width increases from 13 mm to 16 mm with the increase in spacing. When the welding speed is 11 mm/s, the bottom fusion depth of the weld seam decreases from 2.4 mm to 1.6 mm, and the welding width increases from 12.5 mm to 13.8 mm with the increase in spacing. Furthermore, at a welding speed of 8 mm/s, the lack of fusion at the bottom corner of the narrow-gap groove still exists, but they are not present when welding at a speed of 11 mm/s. It is worth noting that the weld bead exhibits a concave shape under the influence of the narrow-gap groove and the double-wire arc, which is a desired result in narrow-gap welding[22].

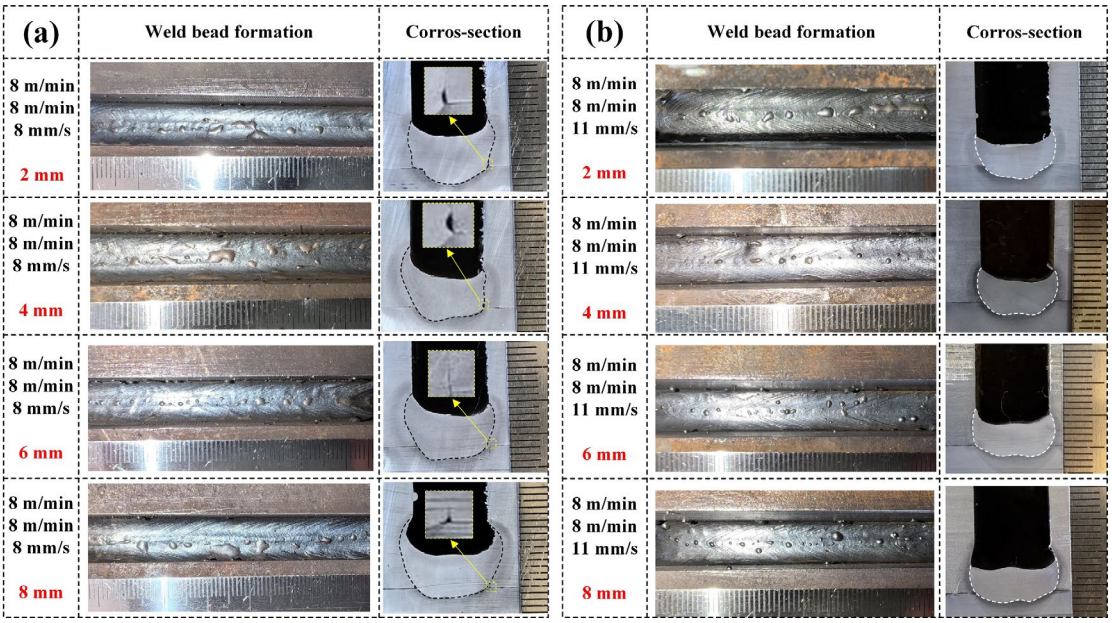


Fig. 2.13. Weld bead formation and cross-section under different lateral spacings (2 mm, 4 mm, 6 mm, and 8 mm) at a wire feeding speed of 8 m/min for the double wires and welding speeds of (a) 8 mm/s and (b) 11 mm/s.

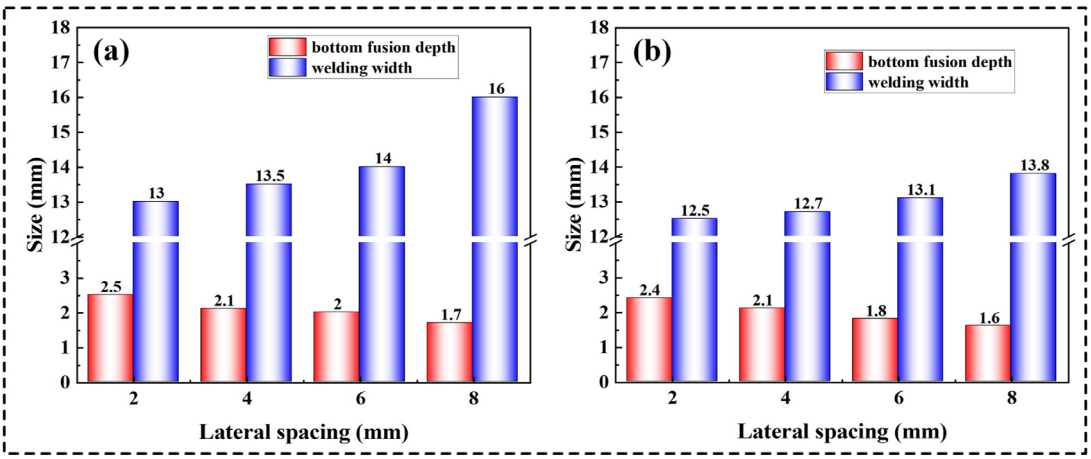


Fig. 2.14. Measurement results of the weld bead section at the welding speed of (a) 8 mm/s and (b) 11 mm/s.

The effects of different heat inputs and lateral spacing between the two wires on weld seam formation are illustrated in Fig. 2.15. With a higher heat input, there is more weld metal deposition and a greater filling height, but the high heat of the arc and the molten pool is mainly concentrated on the upper part of the weld seam, making it difficult for the liquid metal to effectively melt the bottom corner of the groove root. With a lower heat input, the weld metal deposition is lower, and the heat from the arc and molten pool can melt the bottom corner of the groove. When there is no lateral spacing between the two wires, the heat from the arc and molten pool is mainly focused on the bottom of the weld seam, making it difficult for the liquid metal to flow to the bottom corner of the narrow-gap groove and achieve metallurgical bonding. When the two wires form a certain angle with each other, the heat from the arc and molten pool can effectively act on the sidewalls, resulting in an increase in welding width and a decrease in bottom fusion depth. Under lower heat input conditions, in particular, the increase in welding width can effectively prevent the occurrence of the lack of fusion during welding.

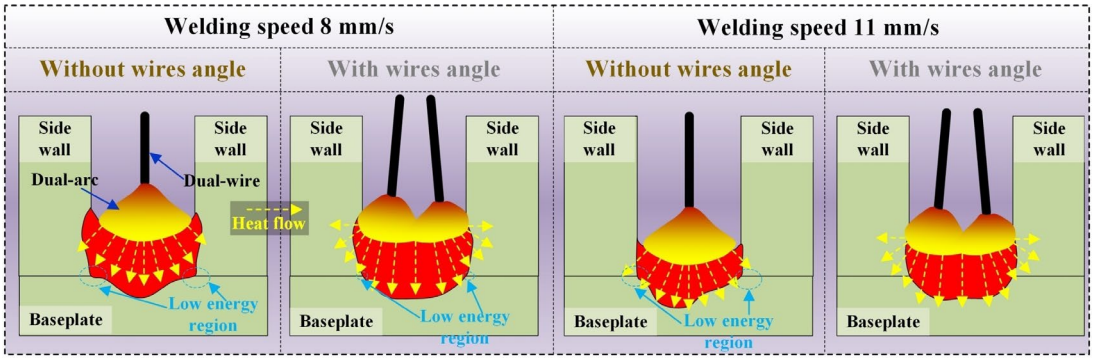


Fig. 2.15. The influence of welding speed and double-wire lateral spacing on weld formation.

In the case of a type I groove, a larger filling height (about 5 mm) leads to the occurrence of the defect of lack of fusion at the root corner, which may result from the limitation of the groove shape. To address this issue, the groove was machined to have a triangular bottom, as shown in Fig. 2.16(a), with the bottom corner of the groove raised 2 mm above the lowest point of the groove, and the width of the gap was 12 mm.

Single-pass filling was conducted at the welding speed of 11 mm/s and 8 mm/s using the optimized welding parameters, wire feeding speed of 8 m/min, and lateral spacing of 6 mm at the ends of the two wires. The resulting weld seam formation and cross-sectional morphology are shown in Fig. 2.16(b1)–(c2). It can be observed that under this groove shape, the weld seams are well formed. The weld seams obtained under both higher and lower heat input conditions are concave weld seams. It is worth noting that the lack of fusion at the root corner did not occur, which is attributed to the raised bottom corner of the groove, eliminating the issue of insufficient heat for melting.

Furthermore, filler welding was performed on a 30 mm thick narrow-gap groove using optimized process parameters (Fig. 2.17(a)). Fig. 2.17(b) and (c) show the cross-sectional morphology of the welded joints at travel speeds of 11 mm/s and 8 mm/s, respectively. The difference in travel speed resulted in a variation in the thickness of a single weld pass. Consequently, at a travel speed of 11 mm/s, the 30 mm thick plate was welded with a total of 9 passes, while at 8 mm/s, it was completed with 6 passes. It is noteworthy that no defects, such as lack of fusion, were observed in the welded joints under either set of parameters.

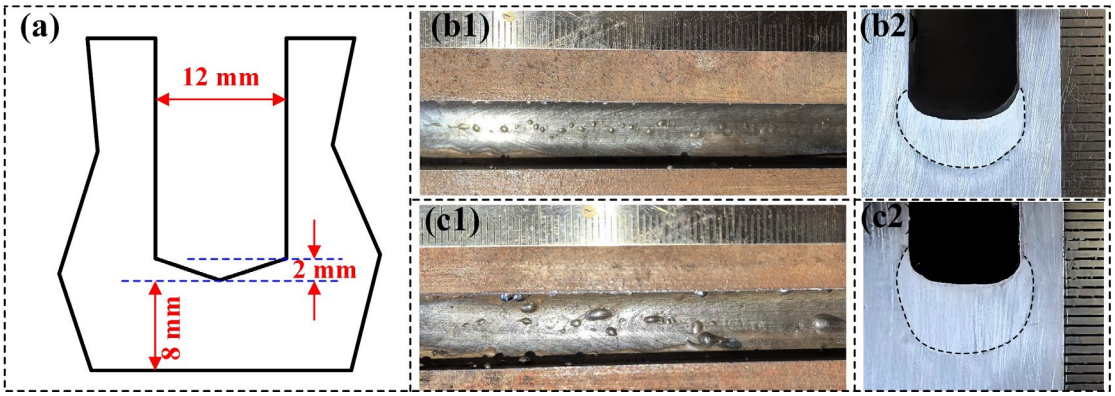


Fig. 2.16. (a) The size of the narrow-gap groove and the weld bead formation and cross-sectional morphology at the welding speed of (b1,b2) 11 mm/s and (c1,c2) 8 mm/s.

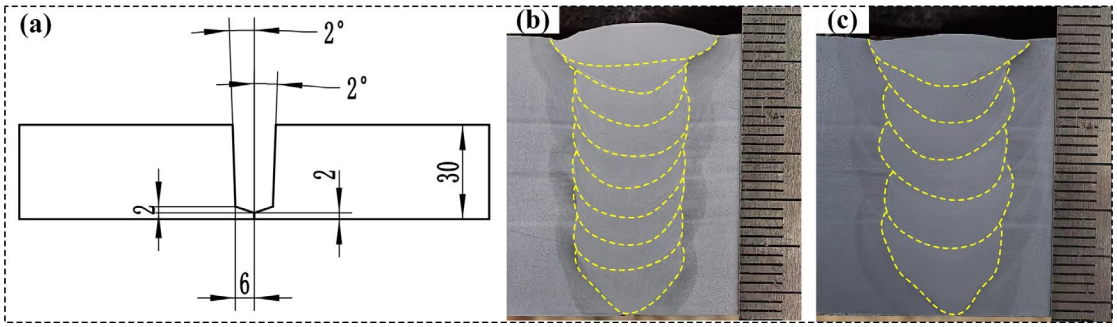


Fig. 2.17. (a) Schematic diagram of the narrow-gap groove dimensions and the cross-sectional morphology of the narrow-gap welded joint at travel speeds of (b) 11 mm/s and (c) 8 mm/s, respectively.

2.5. Summary

This research delves into the application of double-wire narrow-gap gas metal arc welding in low-alloy steel welding. A comprehensive study was conducted on the welding process and weld formation of the double-wire narrow-gap GMAW. The following conclusions can be drawn:

(1) With the increase in the wire feeding speed from 5 m/min to 8 m/min, the welding current and voltage increase, and the welding arc becomes more and more expanded and more and more bright. The droplet transition mode changes from short-circuit transition mode to spray transition mode.

(2) The gradual increase in welding speed from 5 mm/s to 14 mm/s leads to a reduction in metal filling height and welding width. Lower welding speed leads to undercuts, and higher welding speed leads to a lack of fusion.

(3) The gradual increase in double-wire lateral spacing from 0 mm to 8 mm leads to a larger arc area in the narrow-gap groove, improving the weld formation from finger-like to bowl-shaped. However, the larger lateral spacing of 8 mm would cause the arc to fully burn the sidewall, resulting in undercuts.

Chapter 3. Improvement of microstructure and mechanical properties of deposited weld metal ER70-G

3.1. Welding conditions and welding material

3.1.1 Materials and method

This study utilizes ER70-G welding wire, a commonly used 690 MPa grade HSLA steel in practical engineering, with a diameter of 1.2 mm. Since the research focuses primarily on the microstructure and mechanical properties of the deposited metal, Q235 mild steel, a common engineering-grade material with a thickness of 40 mm, is used as the base metal. The chemical compositions of the deposited metal are presented in Table 3.1. The base metal was machined into a narrow-gap groove, the shape and dimensions of which are shown in Fig. 3.1(a). The deposition of the HSLA steel was performed using the double-wire GMA technique, as illustrated in Fig. 3.1(b). The two wires melt to form a common molten pool, shielded by an 80% Ar + 20% CO_2 mixture gas with gas flow rate at 20 L/min. A total of 12 layers were deposited to achieve a thickness of 40 mm. This study aims to investigate the effect of IDT on the microstructure and mechanical properties of the multi-layer deposited HSLA steel. Three sets of comparative experiments were conducted, with the corresponding process parameters listed in Table 3.2. During deposition, parameters including wire feed speed (WFS), welding voltage, and welding travel speed (WTS) were kept consistent across all three groups. The difference lay solely in the IDT. 1# group employed a baseline IDT of 2 minutes, primarily for cleaning the deposited metal surface and repositioning the robotic arm before the next layer. 3# group employed a 22-minute cooling time to ensure the deposited metal cooled to near ambient temperature (based on pre-experimental results and numerical simulations). For comparison, 2# group used a 12-minute cooling time, which was 10 minutes longer than 1# group and 10 minutes shorter than 3# group.

Table 3.1. Chemical composition of the metal wire used in this work. (wt.%)

Elements	C	Si	Mn	S	P	Cr	Ni	Mo	Fe

ER70-G	0.073	0.30	1.45	0.007	0.012	0.052	0.62	0.31	Bal.

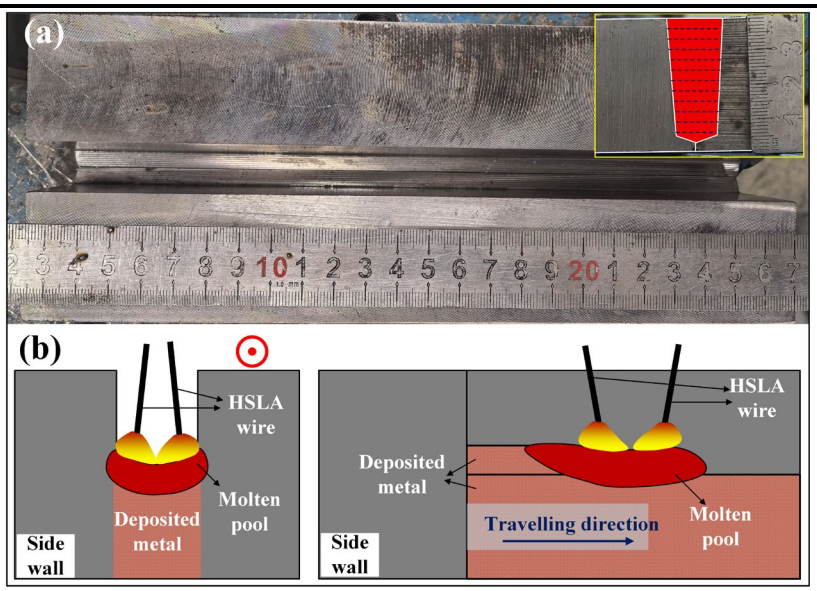


Fig. 3.1. (a) Actual photograph of narrow-gap groove for deposition. (b) Schematic diagram of deposition process.

Table 3.2. Double-wire GMA deposition process parameters ("1" and "2" referred to the front wire and the rear wire, respectively).

Group	WFS-1	WFS-2	WTS	Voltage-1	Voltage-2	IDT
1#	8 m/min	8 m/min	11 mm/s	33.5 V	33.0 V	2 min
2#	8 m/min	8 m/min	11 mm/s	33.5 V	33.0 V	12 min
3#	8 m/min	8 m/min	11 mm/s	33.5 V	33.0 V	22 min

During the deposition process, a temperature measuring device was employed to measure the temperature of each deposited layer after cooling, as shown in Fig. 3.2(a). Fig. 3.2(b) shows the interlayer temperature measurements for the three experimental groups. It can be observed that as deposition progressed, the interlayer temperature of 1# group and 2# group gradually increased, while the interlayer temperature for 3# group increased minimally, remaining near ambient temperature. Fig. 3.2(c) presents the cross-sectional morphologies of the deposited metal obtained for the three groups.

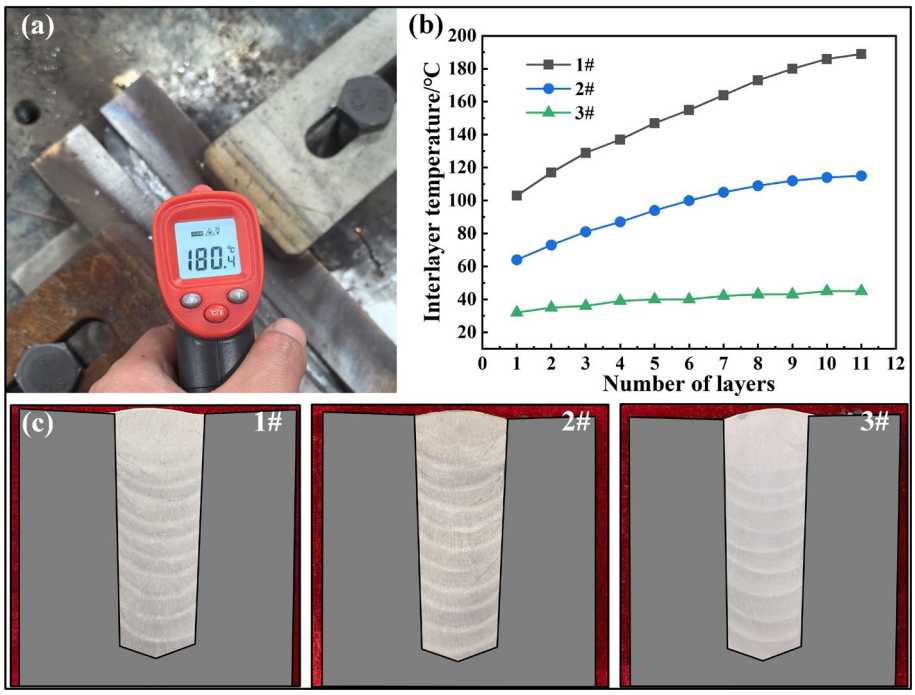


Fig. 3.2. (a) Deposition temperature measurement results for the 9th layer in 1# group. (b) Interlayer temperature variation across the three groups. (c) Cross-sectional morphology of deposited metal from the three groups.

3.1.2 Microstructure and mechanical properties characterization

Electrical discharge machining was used to extract samples for microstructural and mechanical tests. These included metallography, Electron Backscatter Diffraction (EBSD), X-ray Diffraction (XRD), tensile, and Charpy impact samples. The relative locations of the test samples within the deposited metal are illustrated in Fig. 3.3(a). The effective testing region of all samples were located within the central region of the deposited metal. Moreover, to establish an effective microstructure-property relationship, the center height of all samples was maintained at a consistent distance from the bottom of the structure. Fig. 3.3(b) shows the observation area for the metallographic sample, while Fig. 3.3(c) and (d) shows the dimensions of the tensile and Charpy impact samples, respectively.

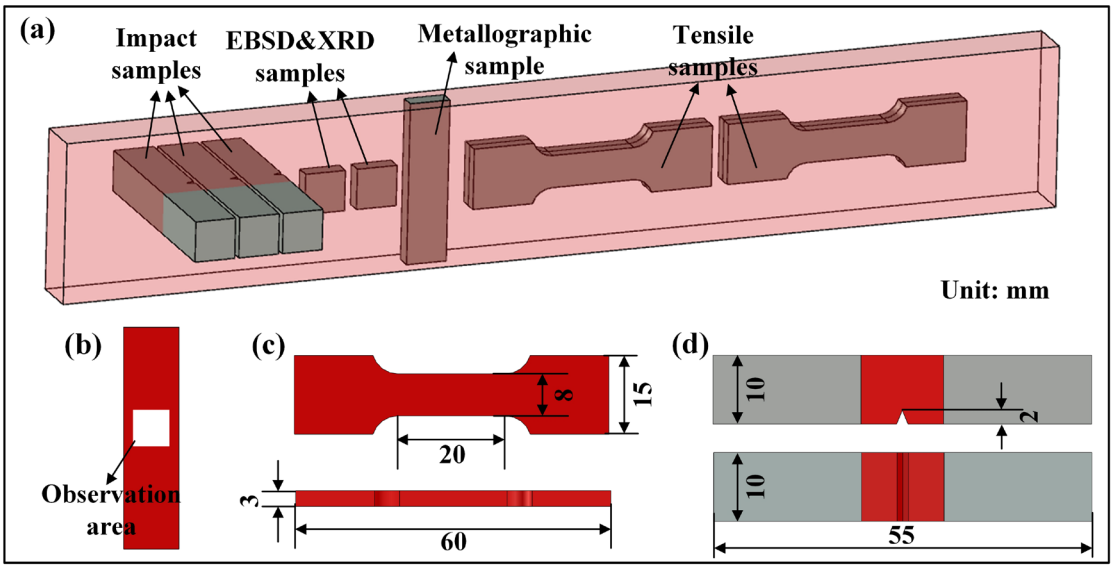


Fig. 3.3. (a)Test samples cutting strategy. (b) Schematic diagram of observation area for microstructure in metallographic sample. Schematic diagrams of geometry and dimensions for (c) tensile and (d) impact samples.

Samples for metallography, XRD, and EBSD were initially ground using abrasive papers and polished with diamond paste. The metallographic sample was then etched using a nitric acid-based etchant. EBSD sample underwent an additional electrolytic polishing step in a solution of 20 vol% perchloric acid in 80 vol% ethanol, conducted at a current of 1.5 A and a voltage of 15 V. Phase identification of the deposited metal was performed via XRD within a 30° to 100° 2θ range, employing a scanning speed of 2°/min. Microstructure characterization was conducted using both Optical Microscopy (OM) and Scanning Electron Microscopy (SEM), the latter operated at an accelerating voltage of 20 kV. Additionally, Energy Dispersive Spectroscopy (EDS) was employed to analyze elemental distribution characteristics within the deposited metal. To obtain detailed crystallographic information, EBSD analysis was performed.

Mechanical properties testing encompassed microhardness, tensile, and impact evaluations. Microhardness measurements were conducted on a Vickers microhardness tester, starting from the second deposited layer and progressing toward the top layer with an indentation spacing of 1.5 mm. A test load of 200 gf was applied with a dwell time of 15 seconds. Tensile testing was performed using an electronic universal testing machine, where dog bone-shaped samples were securely gripped at both ends and

pulled at a constant crosshead displacement rate of 2 mm/min. Charpy V-notch impact testing was carried out using a pendulum-type impact tester. To ensure reproducible results, four tensile and three impact samples were tested per condition. Following the tensile and impact tests, fracture surfaces of the failed samples were examined using SEM.

3.1.3 Thermal modeling

To analyze the thermal processes during deposition and establish the process-microstructure-properties relationship, a numerical simulation of the deposition process was performed using ABAQUS software. Fig. 3.4(a) shows the meshed model constructed according to the actual welded structure dimensions. To balance computational accuracy with efficiency, the deposited metal and adjacent base metal regions were meshed with fine elements, while areas farther from the deposition zone employed a coarse mesh. A transitional mesh connected these two regions.

The double-ellipsoid heat source model, commonly used for GMAW simulations, was adopted as the equivalent heat source, as depicted in Fig. 3.4(b). The heat flux distribution equations for this model are given by Eq. (3-1):

$$\begin{cases} q_f(x,y,z) = \dfrac{6\sqrt{3}f_f Q}{\pi\sqrt{\pi}a_f bc} exp\left[-3\left(\dfrac{x^2}{a_f^2}+\dfrac{y^2}{b^2}+\dfrac{z^2}{c^2}\right)\right] \\ q_r(x,y,z) = \dfrac{6\sqrt{3}f_r Q}{\pi\sqrt{\pi}a_r bc} exp\left[-3\left(\dfrac{x^2}{a_r^2}+\dfrac{y^2}{b^2}+\dfrac{z^2}{c^2}\right)\right] \end{cases} \quad (3-1)$$

Where q_f and q_r represent the heat flux density in the front and rear ellipsoids, respectively. The distribution coefficients f_f and f_r were set to 0.66 and 1.34. The parameters a_f, a_r, b, and c, defining the heat source dimensions, were calibrated to 7 mm, 14 mm, 8 mm, and 5 mm, respectively. Q corresponds to the effective heat input during deposition.

A hybrid heat source model, combining two double-ellipsoid heat sources via a user subroutine written in FORTRAN, was implemented to simulate the double-wire arc deposition process (Fig. 3.4(b)). Fig. 3.4(b) also compares the simulated molten pool shape with experimental results, demonstrating good agreement between the hybrid heat source model and the physical experiments.

The governing equation for transient heat transfer in this model is given by Eq. (3-2):

$$C_p\rho\frac{dT}{dt}=\frac{\delta}{\delta x}\left(k\frac{\delta T}{\delta x}\right)+\frac{\delta}{\delta y}\left(k\frac{\delta T}{\delta y}\right)+\frac{\delta}{\delta z}\left(k\frac{\delta T}{\delta z}\right)+q \qquad (3-2)$$

Where Cp, ρ, k, T, and q represent specific heat capacity, density, thermal conductivity, temperature, and heat input, respectively. Both the initial temperature of the base metal and the ambient temperature were set to 293 K.

Heat exchange between the metal and the environment during deposition occurs primarily through convection (Eq. (3-3)) and radiation (Eq. (3-4)):

$$q_c = \mathrm{h}_c(T_S - T_0) \qquad (3-3)$$

$$q_r = \varepsilon\sigma(T_S^4 - T_0^4) \qquad (3-4)$$

Where h_c, ε, σ, T_S, and T_0represent the convective heat transfer coefficient (15 $W\cdot m^{-2}\cdot K^{-1}$), emissivity (0.8), Stefan-Boltzmann constant (5.67×10^{-8} $W\cdot m^{-2}\cdot K^{-4}$), surface temperature, and ambient temperature, respectively. Additionally, h_c is defined as 100 $W\cdot m^{-2}\cdot K^{-1}$ at the bottom surface of the base metal.

Fig. 3.4(c) presents the simulated temperature field results for the 3# group, showing the cross-sectional morphology after each deposited layer.

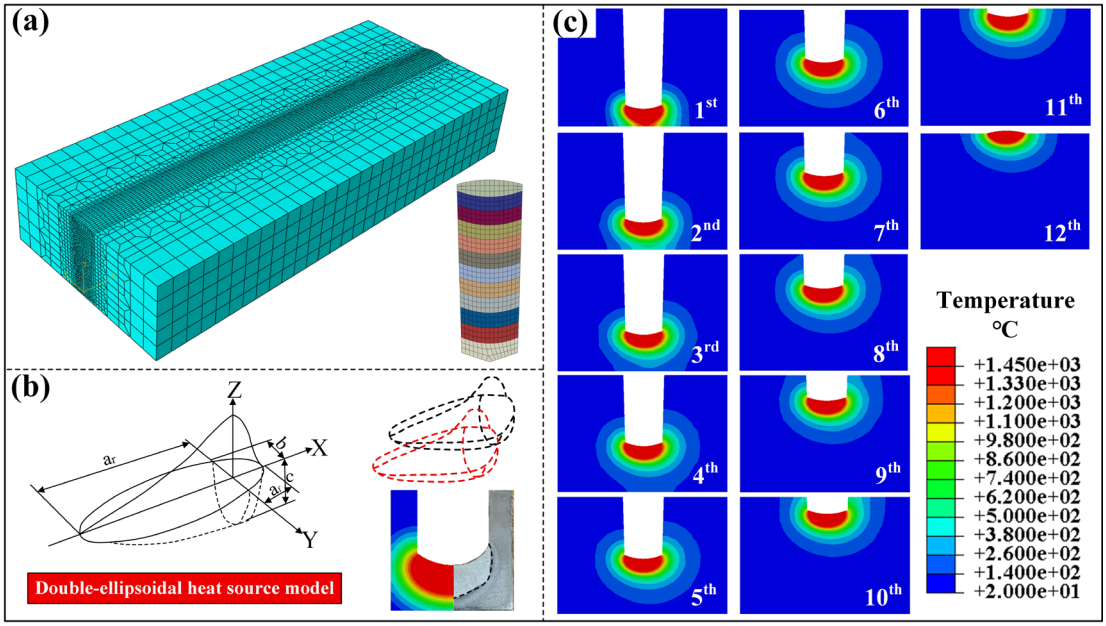


Fig. 3.4. Temperature field simulation modeling: (a) double-wire arc deposition mesh model, (b) double-wire arc deposition heat source model, (c) temperature field contour plot of deposition for 3# group.

3.2. Simulation for dwell time influence

Fig. 3.5 presents the temperature field simulation results for the three experimental groups. Fig. 3.5(a) shows thermal cycle curves plotted using temperature field data extracted from the central region of the sixth deposited layer across all three groups. It can be observed that with increasing IDT, the interlayer temperature decreases, consistent with experimental observations. The microstructure of HSLA steel is significantly influenced by the cooling rate, particularly within the temperature range from 800°C to 500°C[114]. The thermal cycle curves reveal that the deposited metal in all three groups undergoes complete austenitization during the first and second thermal cycles, as the peak temperature exceeds the Ac_3 temperature. During this process, the microstructure of previously deposited solid metal transforms into austenite and subsequently reverts to a BCC phase upon cooling. Therefore, besides the cooling rate during initial solidification, it is essential to also consider the cooling rate during the second thermal cycle.

Fig. 3.5(b) provides magnified views of the sections labeled "First" and "Second" in Fig. 3.5(a). With prolonged IDT, $t_{8/5}$ (cooling time between 800°C and 500°C) decreases. Notably, during the second thermal cycle, $t_{8/5}$ is longer than that during initial solidification. Fig. 3.5(c) displays the calculated cooling rates for the three experimental groups. As IDT increases, the cooling rate due to the first thermal cycle accelerates from 28.1 ℃/s in 1# group to 57.3 ℃/s in 3# group. Additionally, the cooling rate during the second thermal cycle rises from 26 ℃/s in 1# group to 48.1 ℃/s in 3# group.

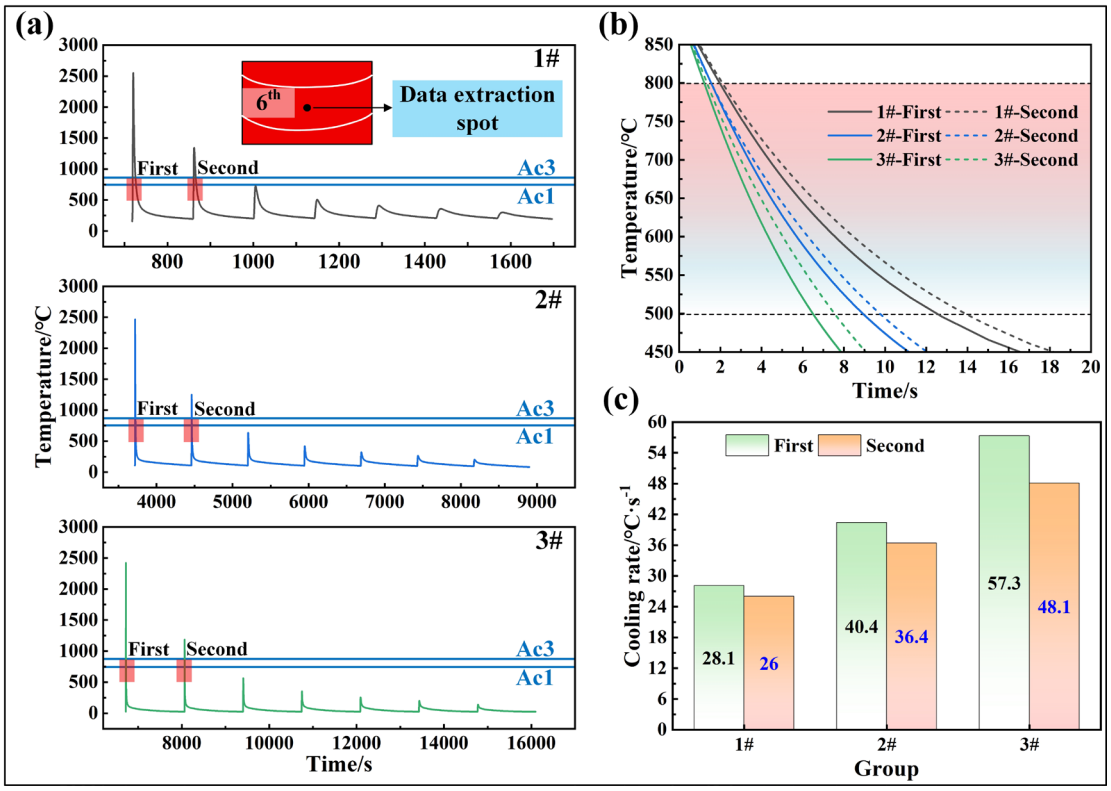


Fig. 3.5. Temperature field simulation results: (a) thermal cycles of the center plot in 6th deposition layer for the three groups, (b) magnified views of the regions marked as "First" and "Second", (c) comparison of cooling rates for the three groups.

3.3. Improvement of microstructure via dwell time strategy

3.3.1 Phase composition

Fig. 3.6(a) presents the XRD patterns of the deposited metal for the three experimental groups. The results indicate that distinct α-phase peaks were detected in all deposited metals, along with corresponding γ-phase peaks. Altering the IDT did not change the phase composition of the deposited metal across the three experimental groups. Fig. 3.6(b) displays the fitted results of ΔK versus $K(C)^{1/2}$ obtained using the modified Williamson-Hall (MWH) method[47]. The horizontal axis represents the corrected effective strain variable, while the vertical axis represents the total broadening effect of the diffraction peak. In the fitted linear relationships, 1# group exhibits the shallowest slope, while 3# group shows the steepest slope, indicating the following ranking of dislocation density in the deposited metal across the groups: 1# < 2# < 3#. These results demonstrate that prolonging the IDT increases the cooling rate of the

deposited metal, subsequently leading to higher dislocation density.

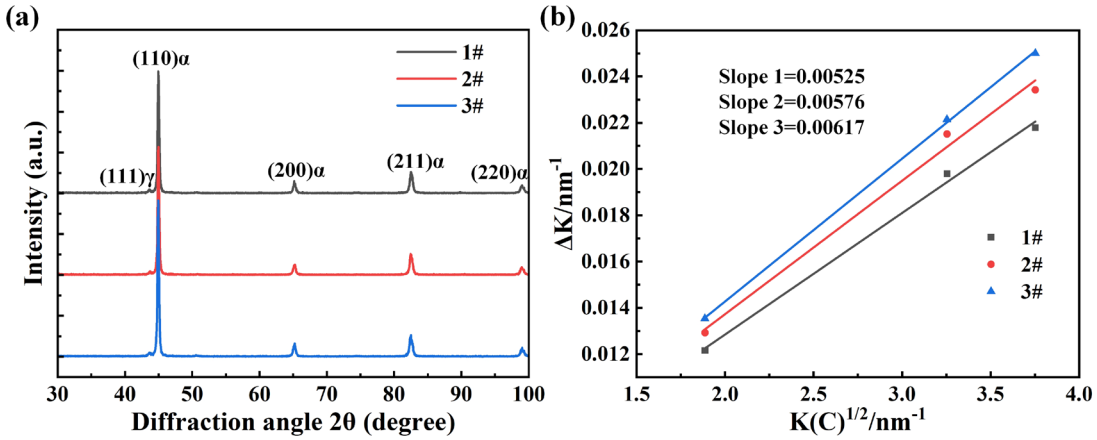


Fig. 3.6. (a) XRD Patterns under different IDT conditions. (b) Fitted lines of ΔK vs. K $(C)^{1/2}$.

3.3.2 Microstructure characteristics

For this HSLA steel, the wire arc deposited metal predominantly consists of ferrite microstructure or bainite microstructure. Fig. 3.7(a)-(c) presents the OM pictures of the intermediate layers within the deposited metal for the three experimental groups, respectively. The microstructural constituents align with studies by other researchers, comprising AF (dark regions in the micrographs) and GBF (light regions in the micrographs)[115, 116]. It is readily apparent that the relative content of GBF differs among the deposited metal from 1#, 2#, and 3# groups. The three micrographs were binarized using ImageJ software, resulting in the images shown in Fig. 3.7(a1)-(c1), where the elongated black strips represent the GBF. ImageJ software was also used to calculate the area fraction of the black regions, representing the proportion of GBF. 1# sample exhibited the highest GBF content at 15.7%, followed by 2# sample at 11.2%, and 3# sample showed the lowest content at only 5.3%. These results demonstrate that prolonging the IDT effectively reduces the GBF content.

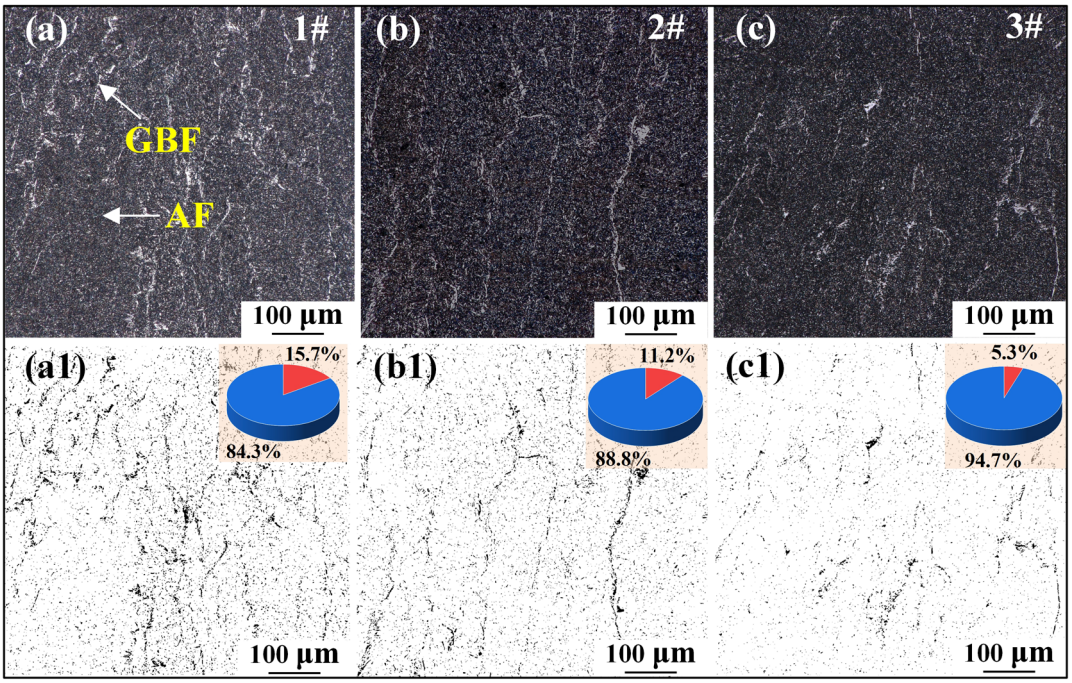


Fig. 3.7. OM images of deposited metal: (a) 1# group, (b) 2# group, and (c) 3# group. GBF proportion statistics: (a1) 1# group, (b1) 2# group, and (c1) 3# group.

Fig. 3.8 presents the high-magnification SEM images of the deposited metal from 1#, 2#, and 3# groups, clearly revealing the morphology of AF. AF nucleates and grows within austenite grains during cooling, with its growth behavior influenced by multiple factors[117]. As the IDT increased from 2 minutes (1# group) to 22 minutes (3# group), significant differences emerged in AF characteristics. The AF in 1# group appeared notably coarse (Fig. 3.8(a)). With prolonged IDT, the ferrite became elongated and exhibited interlocking configurations (Fig. 3.8(b)). Further IDT extension refined the ferrite and intensified interlocking between laths (Fig. 3.8(c)). As shown in Fig. 3.8(d), AF typically encapsulates spherical particles. EDS analysis identified these as oxide inclusions. Studies confirm that dispersed inclusions frequently serve as nucleation sites for AF[118].

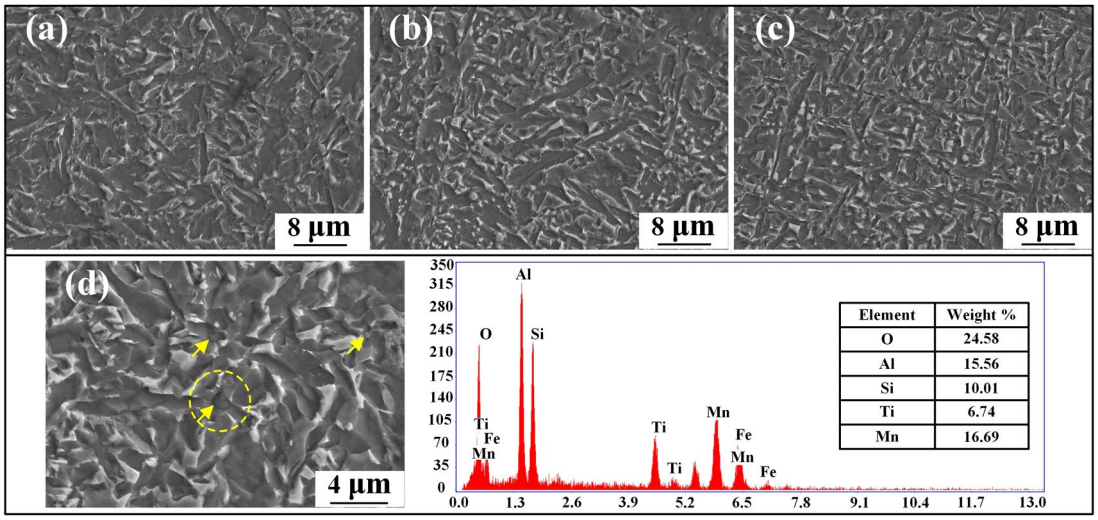


Fig. 3.8. SEM images of the deposited metal: (a) 1# group, (b) 2# group, and (c) 3# group. (d) High-magnification SEM micrograph revealing AF encapsulating oxide inclusions.

Figs. 3.9 and 3.10 show the EBSD results of deposited metal from the three experimental groups, providing further crystallographic details about AF and clarifying microstructural differences in HSLA deposits under varying IDT conditions. Fig. 3.9(a)-(c) displays inverse pole figures (IPFs) for 1#, 2#, and 3# groups, respectively, revealing AF with diverse orientations. As IDT prolonged, the elongated, needle-like characteristics of AF became more pronounced and interlaced with each other, consistent with SEM results. Grain size statistics using AztecCrystal software showed that with IDT extending from 2 min to 22 min, the average grain size refined from 9.96 μm (Fig. 3.9(a1)) to 5.13 μm (Fig. 3.9(c1)). Additionally, grain boundary misorientation angles were statistically analyzed, as shown in Fig. 3.10(a), (b), and (c). The results indicate that prolonging the IDT significantly increased the proportion of HAGBs, rising from 52.8% in 1# group to 68.7% in 3# group. As a reliable indicator of localized strain, Kernel Average Misorientation (KAM) quantifies the average orientation difference (<5°) between a given point and its nearest neighbors within the same grain. For 1#, 2#, and 3# groups, KAM values were 0.73 (Fig. 3.10(a1)), 0.83 (Fig. 3.10(b1)), and 0.91 (Fig. 3.10(c1)). KAM is commonly used to calculate geometrically necessary dislocations (GNDs) by Eq. (3-5)[23].

$$\rho_{\mathrm{GND}} = \frac{2\Theta}{\mu b} \qquad (3-5)$$

Where, Θ represents the radian value of KAM, μ is the EBSD measurement step size (0.2 μm), and b denotes the Burgers vector (0.248 nm). The calculated dislocation densities for the samples in 1# group, 2# group, and 3# group are 5.138×10^{14} m^{-2}, 5.844×10^{14} m^{-2}, and 6.404×10^{14} m^{-2}, respectively. The results indicate that the dislocation density increases with prolonged IDT, which is consistent with the XRD measurements.

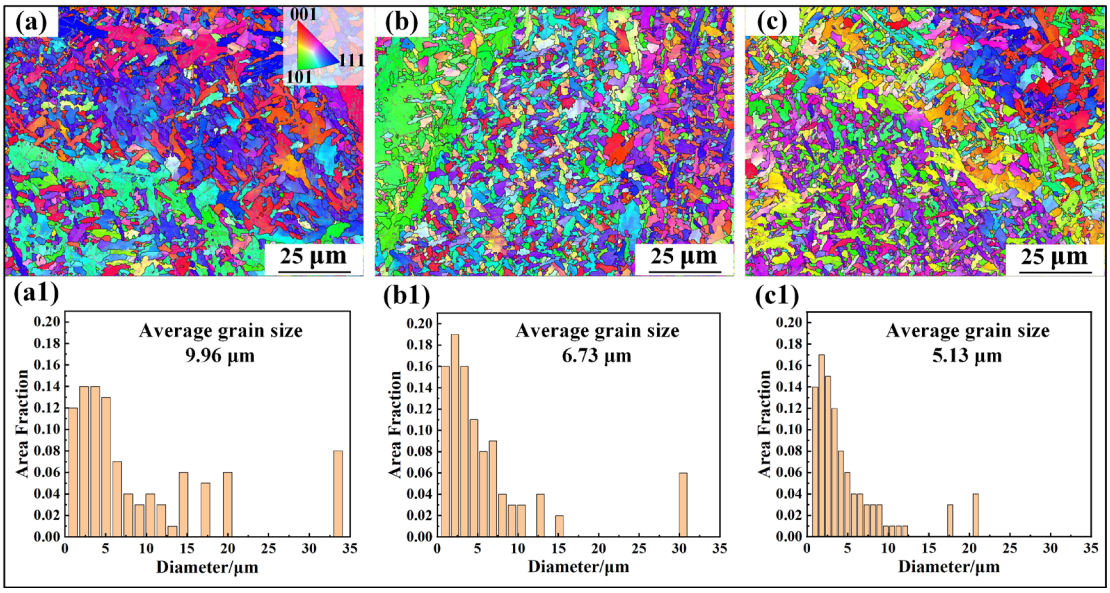


Fig. 3.9. Comparison of IPF maps and grain size distribution charts for samples with different IDT: IPF maps for (a) 1# group, (b) 2# group, and (c) 3# group. Grain size distribution charts for (a1) 1# group, (b1) 2# group, and (c1) 3# group.

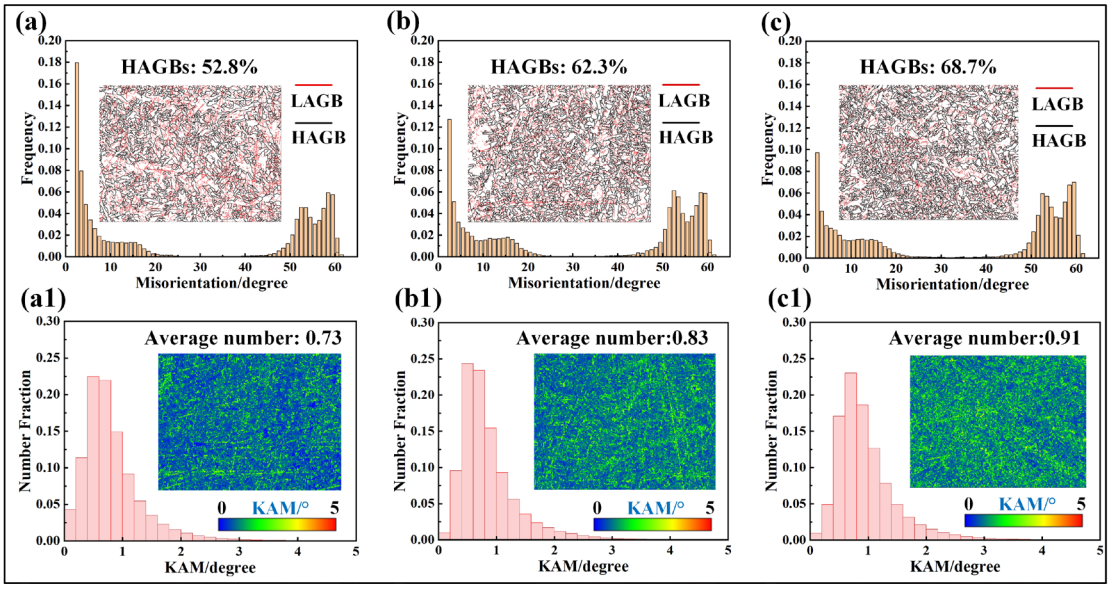


Fig. 3.10. Comparison of grain boundary misorientation and kernel average misorientation for samples with different IDT: Grain boundary misorientation statistics for (a) 1# group, (b) 2# group, and (c) 3# group. Kernel average misorientation statistics for (a1) 1# group, (b1) 2# group, and (c1) 3# group.

3.4. Improvement of mechanical properties via dwell time strategy

3.4.1 Microhardness

Fig. 3.11(a) presents the microhardness distribution across the second layer to the top layer of the deposited metal in 1#, 2#, and 3# groups. It can be observed that for the deposited metal in 1# group, the microhardness distribution exhibits a progressive decrease from the bottom to the top layer, specifically declining from 270.21 HV0.2 at the second layer to 234.27 HV0.2 at the top layer. 2# group similarly demonstrates a progressively decreasing pattern. However, the magnitude of reduction is diminished, with values decreasing from 270.08 HV0.2 at the second layer to 247.28 HV0.2 at the top layer. In contrast, the deposited metal in 3# group displays a relatively uniform microhardness distribution from the bottom to the top layer. This microhardness distribution pattern corresponds to interlayer temperature conditions. In 1# and 2# groups, the interlayer temperature progressively increases, concurrently driving a gradual reduction in microhardness. Furthermore, 1# group exhibits a larger magnitude of interlayer temperature increase compared to 2# group, resulting in a correspondingly

greater microhardness reduction in 1# group. For 3# group, the interlayer temperature essentially remains constant throughout the deposition process, leading to a uniformly distributed microhardness in its deposited metal. The average microhardness values for the deposited metal across all three experimental groups were calculated. Results conclusively indicate that prolongation of IDT increases the average microhardness of the deposited metal, as quantitatively confirmed in Fig. 3.11(b).

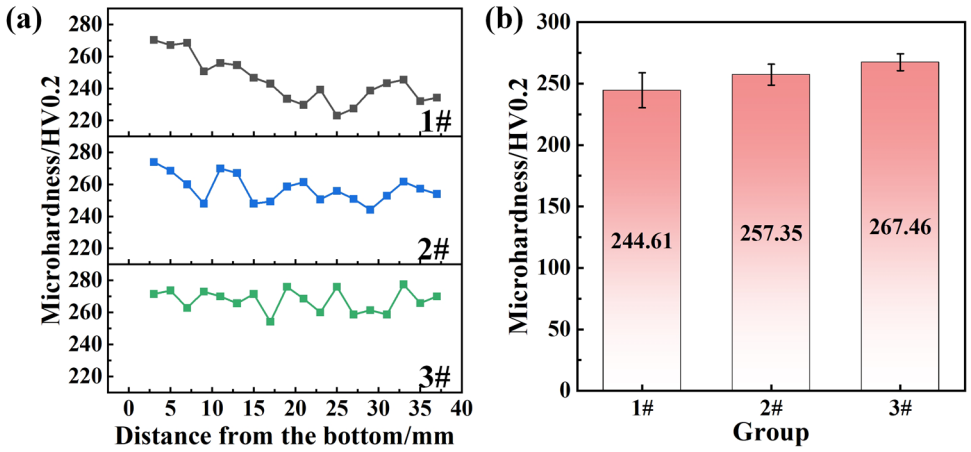


Fig. 3.11. Microhardness measurement results for the three groups: (a) microhardness distribution from the bottom to the top, (b) comparison of average microhardness values.

3.4.2 Tensile properties

Fig. 3.12(a) presents typical engineering stress-strain curves for the tensile samples from the three experimental groups. Fig. 3.12(b) compares the tensile properties of these samples. When IDT increased from 2 to 22 minutes, the ultimate tensile strength increased from 692.3 to 805.4 MPa, and the yield strength increased from 611.9 to 712.1 MPa. However, the post-fracture elongation (EL) across the three groups did not exhibit significant differences, increasing slightly from 24.2% for 1# group to 26.5% for 3# group. Examination of the fractured tensile samples revealed significant plastic deformation in all three groups, characterized by obvious necking. Fracture surfaces of samples from all three groups were observed using SEM, with results displayed in Fig. 3.12. Different IDT conditions resulted in substantial variations among the fracture surfaces. Macroscopically, the measured thickness at the fracture location was 2.04 mm for 1# group (Fig. 3.13(a)), 1.88 mm for 2# group (Fig. 3.13(b)), and 1.73 mm for 3#

group (Fig. 3.13(c)). This progressive decrease in sample thickness confirms an increasing degree of necking. Higher-magnification SEM images were taken of the central region of the fracture surfaces to reveal fracture features. The root of all fracture surfaces exhibited numerous dimples (Fig. 3.13(a1), (b1), (c1)), a signature characteristic of ductile fracture. However, high-magnification SEM images highlight distinct differences in fracture morphology. Dimples in the 1# group sample were generally shallow and cleavage facets, indicative of brittle fracture, were also present (Fig. 3.13(a2)). The 2# group sample exhibited entirely dimpled features (Fig. 3.13(b2)). However, the dimensions of the dimples were notably smaller compared to those in 3# group (Fig. 3.13(c2)). These results demonstrate that the 3# group specimen possessed the highest plasticity. Prolonged IDT improves the plasticity of the deposited HSLA steel, as evidenced by fractographic features. However, no significant difference was observed in elongation, despite a slight improvement. This may be attributed to the relatively small dimensions of the tensile samples. Additionally, all three experimental specimen groups exhibited a predominantly AF microstructure, which ensures good ductility across all samples.

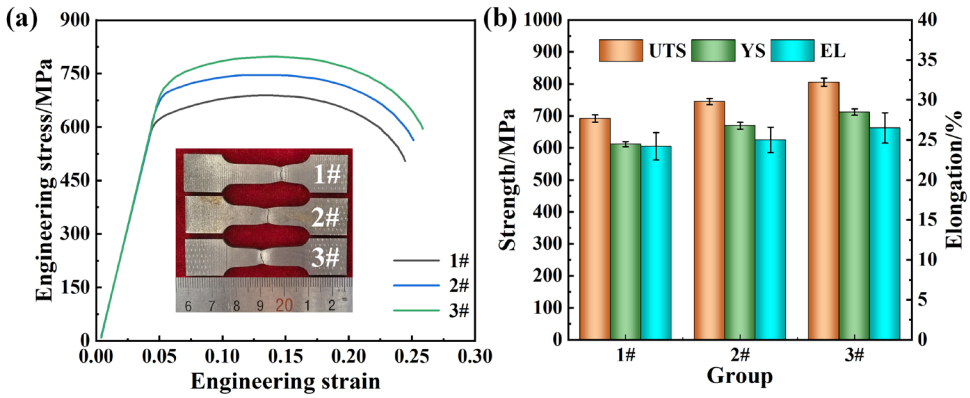


Fig. 3.12. Tensile tests results for the three groups: (a) engineering stress-strain curves and appearance of fractured samples, (b) comparison of UTS, YS and EL.

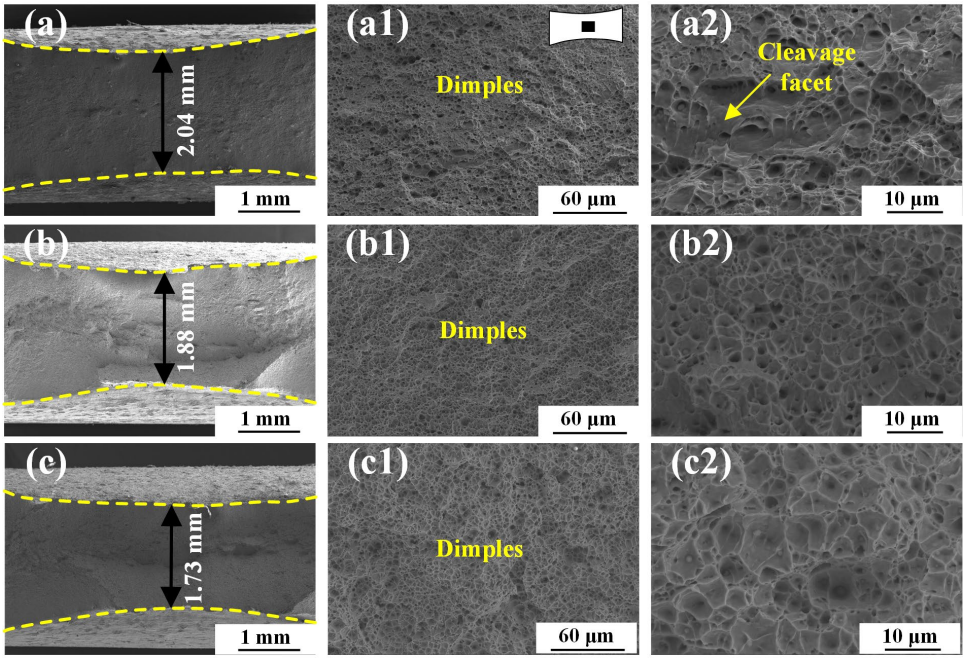


Fig. 3.13. SEM images of the tensile samples fracture surfaces under different IDT conditions: (a)-(a2) 1# group, (b)-(b2) 2# group, (c)-(c2) 3# group.

3.4.3 Impact toughness

Fig. 3.14 presents the Charpy V-notch impact tests results. Fig. 3.14(a) displays the appearance of the impact samples after testing. All three groups of samples exhibited incomplete fractures with significant plastic deformation at the notch. However, the impact absorption energies for samples from 1#, 2#, and 3# groups were 135.67 J, 160.00 J, and 172.67 J, respectively, as shown in Fig. 3.14(b). These results indicate that prolonging the IDT effectively improved the fracture toughness of the deposited metal. SEM was employed to observe the impact fracture surfaces, and the results are presented in Fig. 3.15. Fibrous zones occupied a large proportion of the fracture surfaces in all three groups of deposited metal, as shown in Fig. 3.15(a), (b), and (c). Further SEM observations of the central region of the fracture surfaces revealed that the impact fracture surface of 1# group contained a large area proportion of cleavage facets, calculated as approximately 35.7% using ImageJ software, with the remaining areas exhibiting dimple features (Fig. 3.15(a1)). The proportion of cleavage facets on the impact fracture surface of 2# group was significantly reduced, accounting for about 5.9% (Fig. 3.15(b1)). The impact fracture surface of 3# group showed no large cleavage facets and displayed numerous dimples (Fig. 3.15(c1)). Detailed characterization of the

dimple regions at higher magnification revealed that the dimples on the 1# group impact fracture surface were small in size and exhibited cleavage characteristics (Fig. 3.15(a2)). The dimples on the 2# group impact fracture surface were larger in size and deeper (Fig. 3.15(b2)). The dimples in 3# group further increased in size (Fig. 3.15(b3)). These results also demonstrate that prolonging the IDT effectively enhanced the impact toughness of the deposited HSLA.

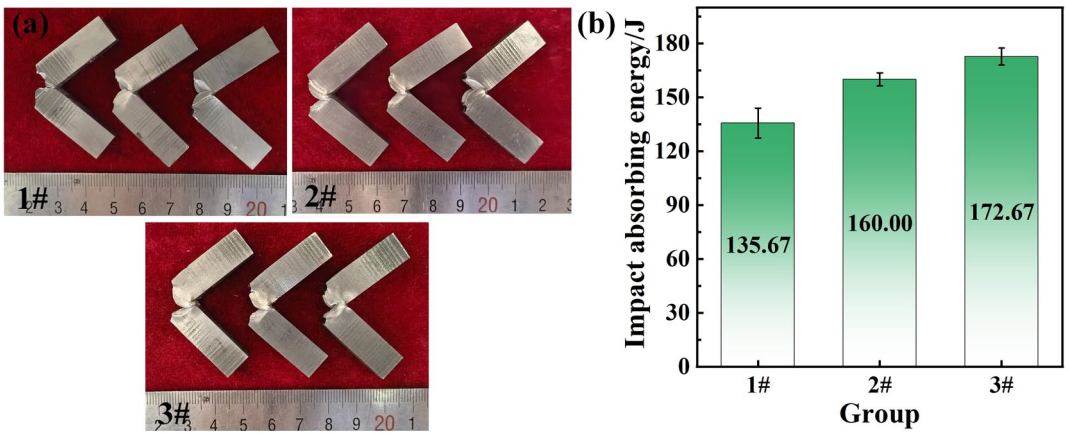


Fig. 3.14. Charpy V-notch impact test results for the three groups: (a) appearance of the fractured samples, (b) comparison of the impact absorbing energy.

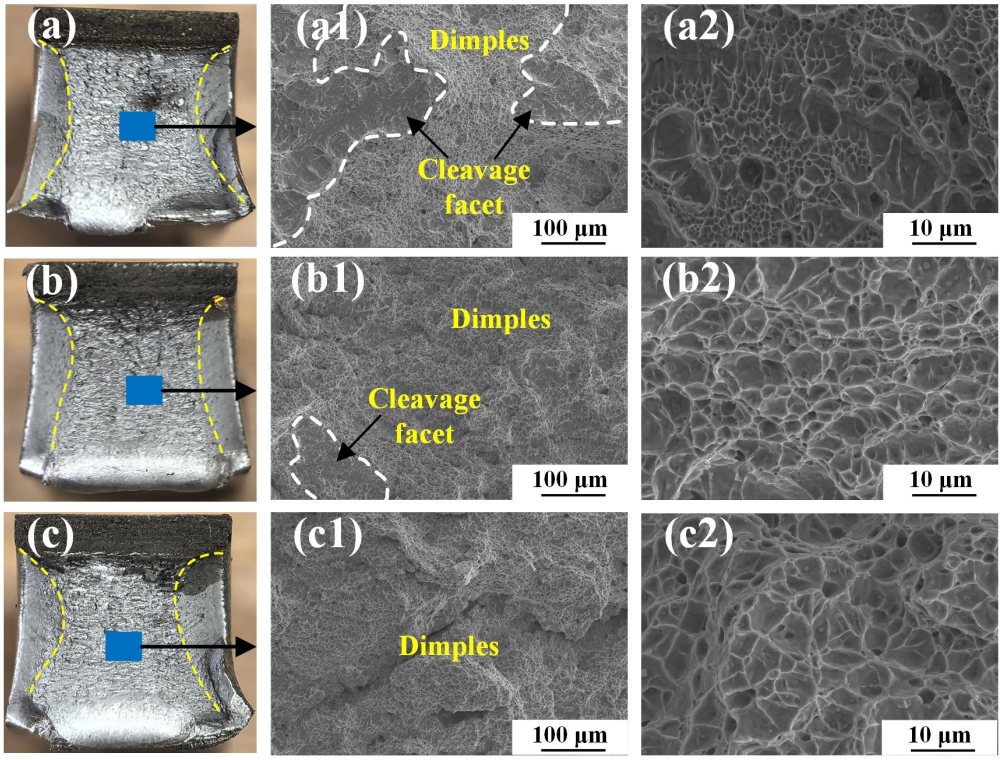


Fig. 3.15. SEM images of the impact samples fracture surfaces under different IDT

conditions: (a)-(a2) 1# group, (b)-(b2) 2# group, (c)-(c3) 3# group.

3.5. Mechanisms of mechanical properties improvement

Table 3.3 summarizes the tensile and impact properties of the deposited HSLA steel under different IDT conditions. As observed, prolonging the IDT leads to a synergistic improvement in both strength and toughness of the steel.

Table 3.3. Statistical analysis of mechanical properties of deposited HSLA steel under different IDT.

Mechanical properties		1# group	2# group	3# group
Ultimate tensile strength/MPa	Mean	692.3	744.8	805.4
	Standard deviation	11.3	9.9	12.5
	range	22.5	15.7	24.2
Yield strength/MPa	Mean	611.9	669.5	712.1
	Standard deviation	7.8	10.75	9.88
	range	15	19.3	21.1
Elongation/%	Mean	24.2	25	26.5
	Standard deviation	1.7	1.6	1.9
	range	2.5	2.6	2.9
Impact toughness/J	Mean	135.67	160	172.67
	Standard deviation	8.33	3.61	4.73
	range	16.4	7.6	12.1

Controlling interlayer dwell time emerges as a key strategy for achieving strength-toughness synergy in double-wire GMA-deposited HSLA steel. This study demonstrates that prolonging IDT effectively optimizes the microstructure and enhances mechanical properties of deposited HSLA steel.

Experimental and numerical simulation results confirm that extended IDT mitigates heat accumulation and significantly accelerates cooling rates in the deposited metal. The elevated cooling rate profoundly influences the nucleation and growth mechanisms of both GBF and AF in HSLA steel[119]. Notably, this research specifically highlights the cooling rate during the second thermal cycle—where peak temperatures exceeded austenitization thresholds—leading to reoccurrence of the γ-austenite to α-ferrite phase

transformation during subsequent cooling.

During cooling from the high-temperature molten pool, ferrite forms from austenite across a broad temperature range. At relatively higher temperatures, GBF nucleates along prior austenite grain boundaries and grows via a diffusion-controlled mechanism[120]. With further cooling, AF nucleates on dispersed inclusions within austenite grains and grows in an acicular morphology[121]. Prolonged IDT increases cooling rates, which affects GBF formation. Higher temperatures allow carbon to diffuse from ferrite to austenite, promoting GBF growth along grain boundaries[122]. However, accelerated cooling shortens the high-temperature dwell time, restricting carbon diffusion and impeding GBF growth. Additionally, increased cooling rates induce greater undercooling, diminishing the dominance of diffusion kinetics required for GBF nucleation and growth. For AF, finely dispersed particles provide nucleation sites, as highlighted in Fig. 3.8(d). Di et al.[118] demonstrated that an increased cooling rate elevates the inclusion density in deposited metal, thereby promoting intragranular nucleation of AF. Additionally, although greater undercooling lowers the nucleation temperature, it significantly enhances the phase transformation driving force and improves the nucleation capability of AF. Mutual impingement between differently oriented AF plates hinders their coarsening. Prolonged IDT effectively refined the microstructure of the deposited metal, manifested as reduced GBF content, finer AF dimensions, and increased proportion of HAGBs, as evidenced in Figs. 3.7, 3.8, 3.9 and 3.10.

The microstructure of deposited HSLA steel determines its mechanical properties. In this study, synergistic enhancement of strength and toughness was realized through prolonging the IDT. The increase in strength is attributable to grain refinement (Hall-Petch relationship) and elevated dislocation density. Refined grains enhance strength by intensifying resistance to dislocation motion[123], while higher dislocation density obstructs plastic flow[124]. The contributions of grain refinement strengthening and dislocation strengthening to the yield strength can be calculated using Eq. (3-6) and Eq. (3-7), respectively[125].

$$\Delta\sigma_{GB} = Kd^{-\frac{1}{2}} \quad (3-6)$$

$$\Delta\sigma_{Dis} = \alpha MGb\rho^{\frac{1}{2}} \quad (3-7)$$

Where, K is the Hall-Petch constant (~17.402 N/mm$^{3/2}$), d is the average grain size, α is a constant (0.435), M is the Taylor factor (2.75), G is the shear modulus (80.3 GPa), b is the Burgers vector (0.248 nm), and ρ is the dislocation density. The grain size and dislocation density data were obtained experimentally, while the remaining data were taken from references[126, 127].

EBSD statistical analysis revealed that the average grain sizes for the 1#, 2#, and 3# experimental samples were 9.96 μm, 6.73 μm, and 5.13 μm, respectively. Calculation using Eq. (3-6) showed that the grain refinement strengthening contribution of 2# sample relative to 1#sample was 38 MPa (212.1 MPa - 174.1 MPa), and that of 3# sample relative to 2# sample was 31.1 MPa (243.2 MPa - 212.1 MPa).

The dislocation densities of the 1#, 2#, and 3# experimental samples obtained from EBSD were 5.138×10^{14} m^{-2}, 5.844×10^{14} m^{-2}, and 6.404×10^{14} m^{-2}, respectively. Calculation using Eq. (3-7) indicated that the dislocation strengthening contribution of 2# sample relative to 1# sample was 12.9 MPa (209.48 MPa - 196.53 MPa), and that of 3# sample relative to 2# sample was 9.82 MPa (219.3 MPa - 209.48 MPa).

In this study, a yield strength increase of 100.2 MPa was achieved through IDT control, with grain refinement strengthening contributing 69.1 MPa and dislocation strengthening contributing 22.72 MPa. In addition to these two primary strengthening mechanisms, the improvement in the yield strength of the deposited metal may also involve other minor influencing factors.

Improved impact toughness benefits from reduced GBF content and increased proportion of HAGBs. Decreased GBF minimizes weak interfacial paths for crack propagation[34]. Furthermore, HAGBs possess higher resistance to crack propagation, deflecting and branching cracks to increase fracture path tortuosity[128]. Fig. 16 displays microstructures near the impact fracture surfaces of 1# and 3# samples. In the deposited metal of 1# group, crack paths extending along GBF exhibit the straightest trajectory (Fig. 3.16(a)). While AF demonstrates superior crack propagation resistance

compared to GBF, coarse AF provides limited resistance, resulting in relatively flat fracture paths (Fig. 3.16(a1)). Conversely, the deposited metal in 3# group features finer grains and distinctly interlocked AF, significantly improving crack propagation resistance. As shown in Fig. 3.16(b), its fracture paths are tortuous compared to those in 1# group. In conclusion, the synergistic improvement in strength and toughness of deposited HSLA steel correlates intrinsically with decreased GBF content, refined AF, and heightened dislocation density, as schematically presented in Fig. 3.16(c). Although this study did not directly investigate the fracture toughness of the three groups deposited metal, literature reports suggest that the microstructural improvements achieved in this study may also contribute to enhanced fracture toughness[129].

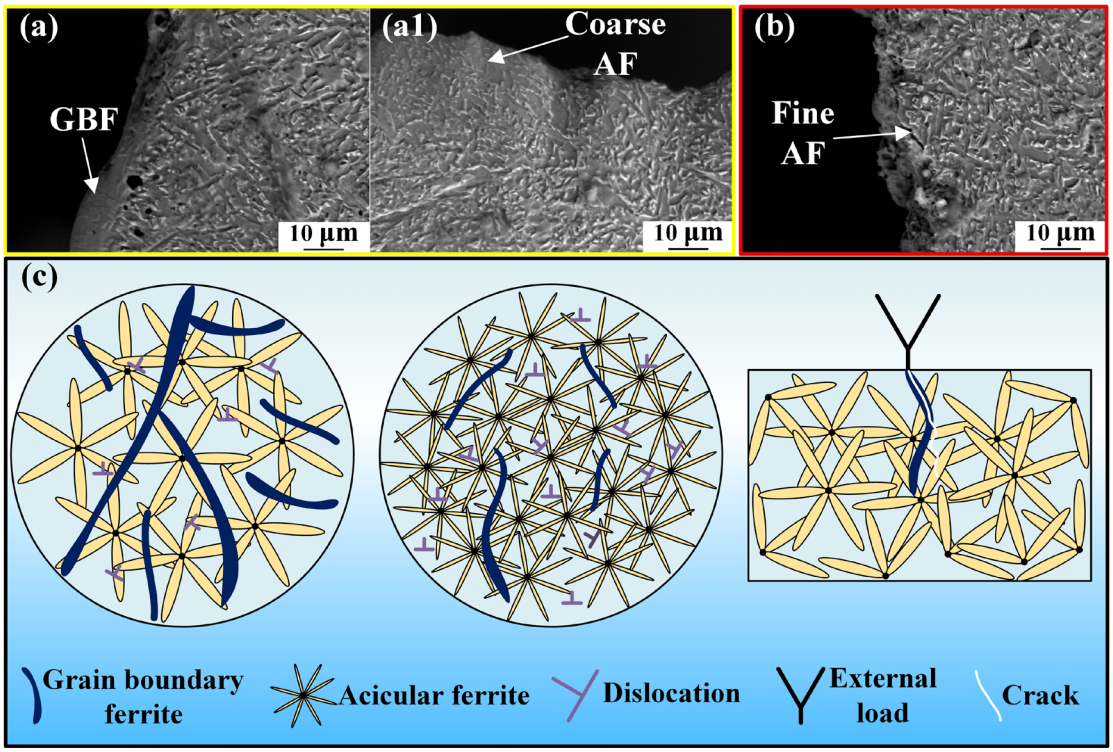


Fig.3.16. SEM images of the crack path for (a), (a1) 1# group and (b) 3# group. (c) Schematic diagram of microstructure-mechanical property relationship.

3.6. Summary

This study shows that controlling interlayer dwell time effectively enhances both strength and toughness in double-wire multilayer GMA-deposited HSLA steel. The key findings are summarized as follows:

(1) Prolonged IDT stabilizes interlayer temperature, mitigates thermal accumulation, and thereby increases cooling rate by 85% (from 26 °C/s to 48.1 °C/s).

(2) The microstructure of deposited metal across all three groups comprises GBF and AF, with GBF content decreasing from 15.7% to 5.3%, grain size refining from 9.96 μm to 5.13 μm, and HAGBs proportion increasing from 52.8% to 68.7% as IDT extends from 2 min to 22 min.

(3) Reduced thermal accumulation ensures uniform microhardness distribution in 40-mm-thick deposits, eliminating property gradients in multilayer deposition.

(4) With IDT extension, UTS increases by 16.3% (from 692.3 to 805.4 MPa), impact toughness improves by 27.3% (from 135.67 to 172.67 J), and fracture mode transitions from ductile-brittle mixed to fully ductile. Strength enhancement can be attributed to grain refinement and elevated dislocation density, while toughness improvement is linked to reduced GBF content and increased HAGBs proportion.

Chapter 4. Comprehensive evaluation of NM450/ER70-G/ZG30SiMn dissimilar welded joint

4.1. Welding conditions and welding material

4.1.1. Materials and Methods

In this study, 40-mm-thick cast steel ZG30SiMn and wear-resistant steel NM450 served as the base materials (BMs). A 1.2-mm-diameter low-alloy high-strength steel wire (ER70-G) was chosen as the filler material. The rationale for adopting mismatched filler metals lies in minimizing the risk of welding cracks. The chemical compositions and mechanical properties of the materials are listed in Table 1 and Table 2. The chemical composition and mechanical properties of BMs, verified through testing, conformed to the standards GB/T 24186-2009 (NM450) and JB/T 5000.6-2007 (ZG30SiMn). According to the equation of the International Institute of Welding for carbon equivalent, the carbon equivalent values of NM450 and ZG30SiMn were 0.65 and 0.6, respectively, indicating cold cracking susceptibility. To mitigate this, the BMs were preheated to 120°C. A shielding gas mixture of 80% argon (Ar) and 20% carbon dioxide (CO_2) was employed during welding.

Table 4.1. Chemical compositions of the BMs and welding wire used in this work.

(wt.%)

Elements	C	Si	Mn	S	P	Cr	Ni	Fe
NM450	0.21	0.35	1.61	0.008	0.009	0.86	0.015	Bal.
ZG30SiMn	0.28	0.64	1.39	0.02	0.02	0.43	0.06	Bal.
ER70-G	0.073	0.30	1.45	0.007	0.012	0.052	0.62	Bal.

Table 4.2. Mechanical properties of the BMs and welding wire used in this study.

Properties	Ultimate tensile strength	Elongation	Impact absorbing energy
NM450	1307.6 ± 34.96 MPa	13.2 ± 1.2%	62.3 ± 8.5 J
ZG30SiMn	1083.3 ± 4.72 MPa	9.8 ±1.1%	42.6 ± 5.7 J
ER70-G	690-890 MPa	≥14%	≥147 J

A custom-built double-wire narrow gap GMAW system was utilized in this study. The welding system comprised a six-axis robot, a double-wire GMAW torch, two welding power sources, two wire feeders, and two shielding gas cylinders, as depicted

in Fig. 4.1(a). The NM450 and ZG30SiMn base materials were machined into a narrow gap groove for wire filling. The groove featured a 12-mm bottom width, a 2-mm root face thickness, and a top-widening geometry to compensate for welding-induced thermal shrinkage. The sidewalls formed an included angle of 6°, as shown in Fig. 4.1(b). A 10-minute interlayer cooling period was imposed after each layer deposition, with a total of 8 filler layers applied. Fig. 4.1(c) shows the interlayer temperature monitored using an infrared thermometer.

Fig. 4.2 illustrates the welding process. the two welding wires were positioned in a tandem configuration, inclined at a specific angle relative to the welding direction, with each wire directed toward opposite groove sidewalls. A high-speed camera and electrical data acquisition system were employed to analyze arc morphology, droplet transfer behavior, and current-voltage waveforms for process stability assessment. In this work, both wire feeding speeds were set at 8 m/min, and the robot arm travel speed (welding speed) was 8 mm/s. The welding parameters used were optimized in our prior research.

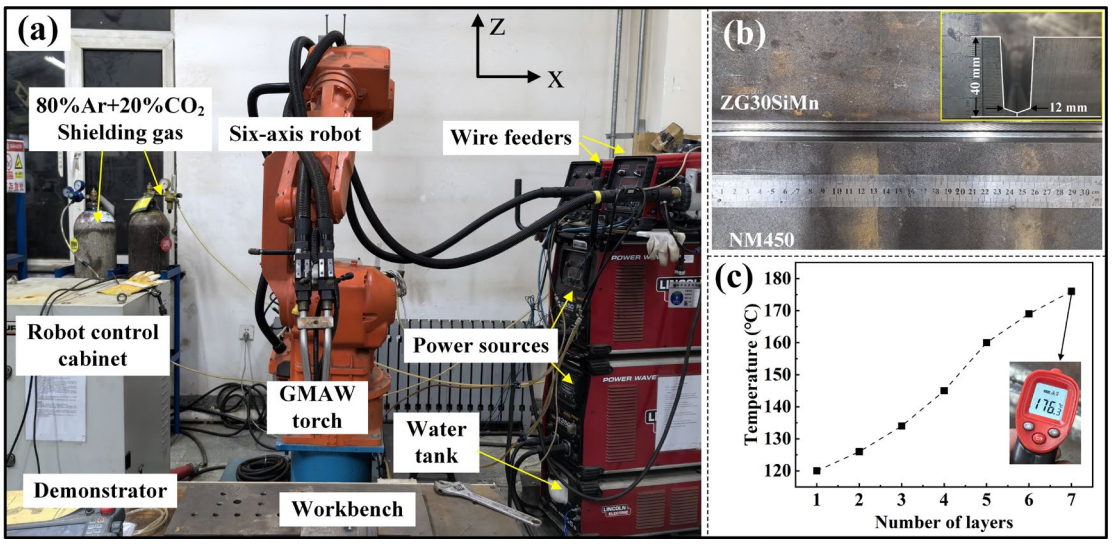


Fig. 4.1. (a) Double-wire narrow gap welding system. (b) Base metals and weld groove geometry. (c) Interlayer temperature measurement during welding.

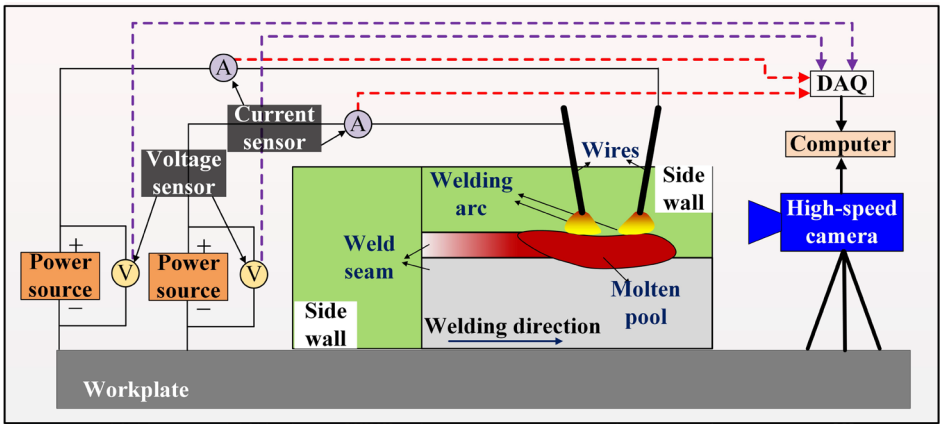


Fig. 4.2. Schematic illustration of the welding process.

Metallographic sample, electron backscattering diffraction (EBSD) sample, X-ray diffraction (XRD) sample, impact samples, and tensile samples were machined from the middle layers of the welded component via electrical discharge machining, as shown in Fig. 4.3(a) and (b). The metallographic sample encompassed the whole welded joint, including WM, HAZ, and BM. The EBSD and XRD samples were extracted from the WM. Additionally, the central axis of the impact samples (WM) and tensile specimens coincided with the WM centerline, while the HAZ impact samples were positioned with their centers 1 mm from the fusion line on each side. These samples were prepared to evaluate weld quality. Fig. 4.3(c)-(e) show the dimensions of the metallographic sample, EBSD sample, XRD sample, tensile samples, and impact samples, respectively.

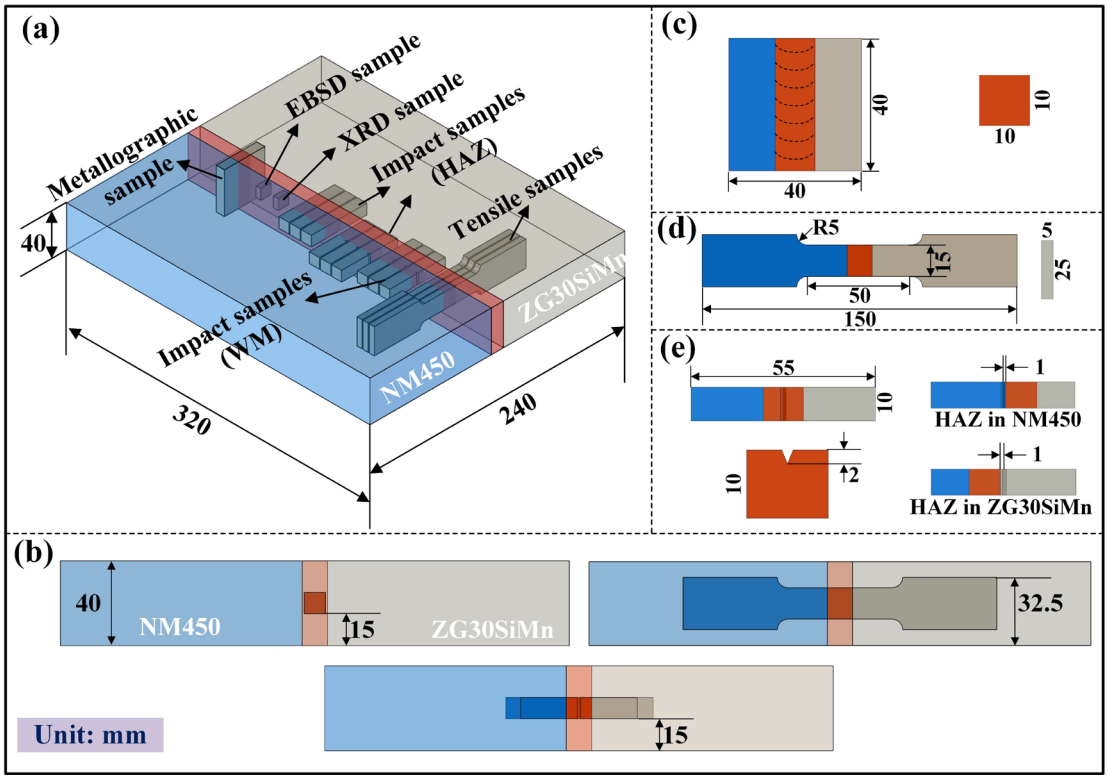


Fig. 4.3. (a), (b) Cutting schematics for testing samples. (c)-(e) Geometric dimensions of the metallographic sample, EBSD & XRD samples, tensile samples and impact samples, respectively.

4.1.2. Microstructure analysis

The metallographic sample, EBSD sample and XRD sample were polished using sandpapers and diamond grinding paste. The polished metallographic sample was etched with nital (4 vol%), and the microstructure was observed via optical microscope (OM) and scanning electron microscopy (SEM). Besides, elemental distributions in the WM and at the fusion interface were analyzed by energy-dispersive spectroscopy (EDS). In order to obtain more crystallographic information, EBSD analysis was performed. The EBSD sample was further electropolished using a solution composed of 20 mL perchloric acid and 80 mL alcohol, with an applied voltage of 15 V and current of 1.5 A for 30 s. Additionally, the phase composition of the WM was analyzed by XRD at a scanning speed of 2°/min over a 2θ range of 10° to 100°.

4.1.3. Mechanical properties analysis

Microhardness measurements across the welded joint were performed using a Vickers hardness tester in accordance with GB/T 2654-2008. Tests were conducted

along and perpendicular to the weld seam, with a load of 200 gf applied for a holding time of 15 s. Uniaxial tensile tests were executed using an electronic universal testing machine compliant with GB/T 2651-2008. Samples were loaded at a constant crosshead speed of 2 mm/min until fracture. Charpy V-notch impact tests were carried out on a pendulum impact testing machine in accordance with GB/T 2650-2008. The fracture surfaces of the failed tensile and impact samples were examined by SEM, and EDS was used to analyze the chemical compositions of microstructural particles.

4.1.4. Thermal modeling

To acquire temperature field data during the welding process and establish the process-microstructure-property relationship, a thermal simulation was conducted using ABAQUS software. Fig. 4.4 presents the physical properties of the materials used in the study—including density (Fig. 4.4(a)), thermal conductivity (Fig. 4.4(b)), and specific heat (Fig. 4.4(c)),which were calculated using JMatPro software.

Fig. 4.5(a) shows the mesh generation for the narrow gap welded structure, where hybrid meshing was employed to balance simulation accuracy and computational efficiency. During mesh generation, the element size gradually transitioned from the weld metal (WM) to the base metal (BM), with fine hexahedral meshes applied to the WM and its adjacent heat-affected zone (HAZ). Coarse hexahedral meshes were utilized in regions with minimal temperature gradients to reduce computational load. The double-ellipsoid heat source model is widely used for simulating arc welding and additive manufacturing processes. In this work, a hybrid heat source model comprising two double-ellipsoid heat sources was adopted to simulate the double-wire narrow gap welding process. The validation of the heat source model in Fig. 4.5(a) demonstrates close agreement between the simulated and experimental molten pool characteristics, confirming its accuracy. Fig. 4.5(b) presents the temperature field simulation results, where the gray region denotes the molten pool. The maps illustrate the temperature distribution during welding, which is in good agreement with the thermal behavior observed in the actual welding process.

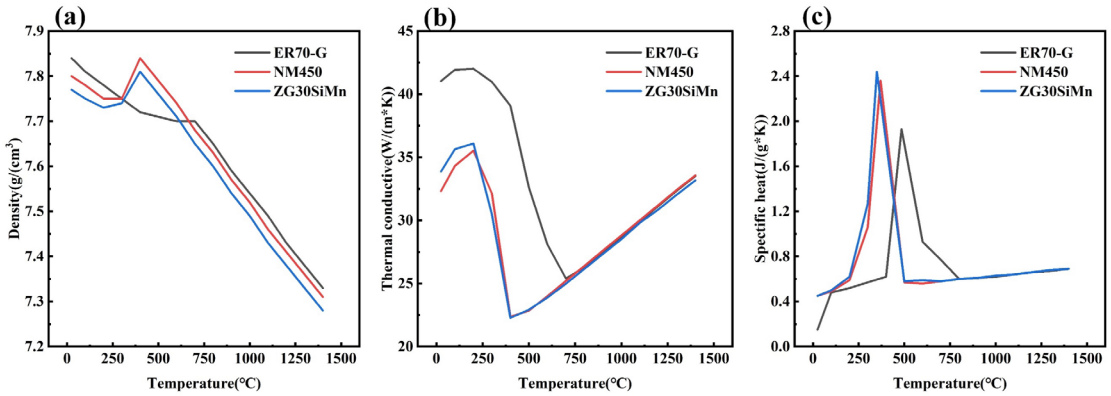


Fig. 4.4. Physical properties of the material: (a) density, (b) thermal conductive, and (c) specific heat.

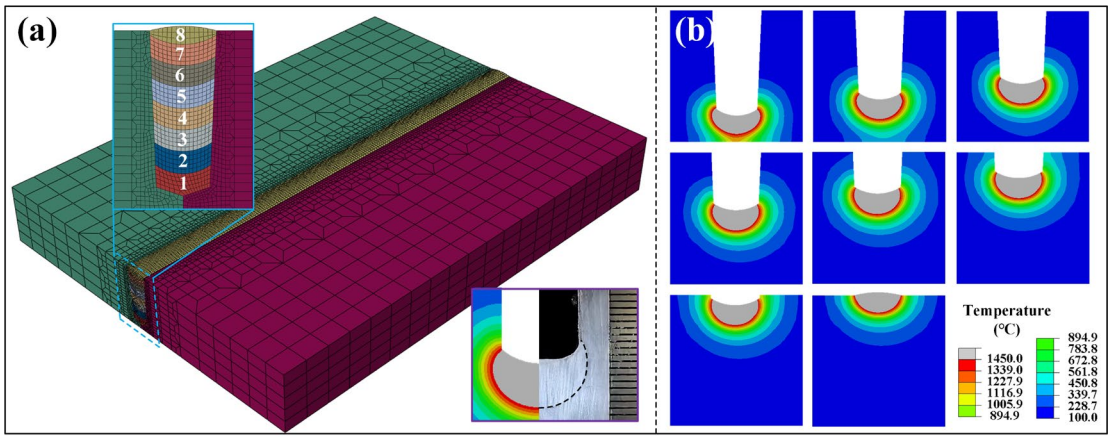


Fig. 4.5. Numerical simulation of temperature fields: (a) mesh model and heat source verification, (b) temperature distribution map during welding.

4.2. Elements distribution characteristics in welded joint

Owing to the chemical composition disparities among the three materials (NM450, ZG30SiMn, and ER70-G), elemental diffusion occurred at the fusion interface between the WM and BMs, as illustrated in Fig. 4.6. Line-scan EDS results revealed that C and Cr from the NM450 steel diffused into the WM, while Ni from the WM migrated toward the NM450. From the WM to the ZG30SiMn steel, the concentrations of C, Si, and Cr slightly increased, whereas Ni content decreased. The elemental diffusion trend generally followed the concentration gradient, forming a chemically graded transition zone near the fusion line[130]. Additionally, the WM exhibited greater elemental inhomogeneity compared to the BMs, likely attributable to the rapid cooling rate of the molten pool, which suppresses elemental homogenization. Studies have shown that

such elemental redistribution may lead to complex microstructures at the interface, potentially compromising mechanical properties[131].

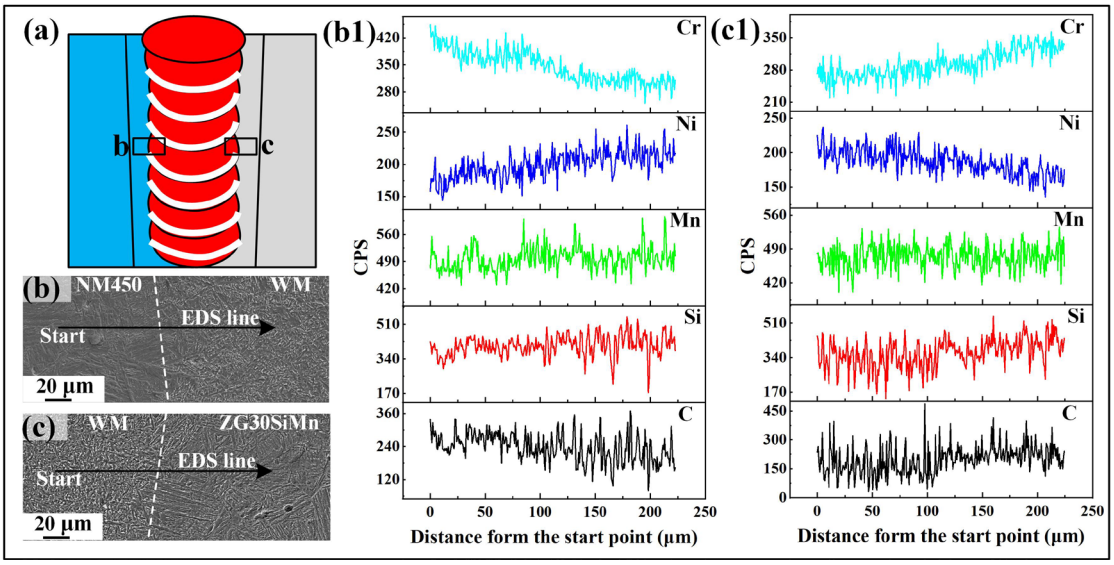


Fig. 4.6. EDS characterization at the weld interfaces: (a) schematic of the detection locations, (b), (b1) elemental distribution across the filler metal–NM450 interface, (c), (c1) elemental distribution across the filler metal–ZG30SiMn interface.

4.3. Microstructure characteristics and evolution in welded joint

4.3.1 Macroscopic forming of welded joints

Fig. 4.7(a) shows the weld seam appearance of root layer, middle layer, and capping layer during the narrow gap welding process. It can be seen that the filling materials achieved sound metallurgical bond with the base metals. Fig. 4.7(b) presents the cross-sectional of the welded joint, which can be divided into five parts, including the WM, two HAZs, and two BMs. The boundaries between these regions are clearly distinguishable in Fig. 4.7(b). It is worth noting that the WM can be further subdivided into zones characterized by distinct coloration. Due to the welding thermal cycles, the previous weld beads underwent re-melting, re-solidification and solid-state phase transformations. It appeared as a periodic white band, which was common in multi-layer welding or additive manufacturing structures[49, 55]. Interestingly, the white bands appeared almost between each two layers, but this did not mean that the white band was caused by the thermal effect on the previous weld seam. the first white band

originated at the bottom of the first filler layer, rather than the fusion line between the first and second layers. Besides, the absence of a white band between the seventh and eighth layers suggests that the band between the sixth and seventh layers was induced by thermal cycle from the eighth layer. HAZ experienced more complex thermal cycles, with varying peak temperatures and dwell times driving microstructural and property evolution. Fig. 4.7(c) and (d) shows the typical microstructures of NM450 and ZG30SiMn, respectively. NM450 consists of martensite and bainite at room temperature, while ZG30SiMn exhibits a martensitic matrix[132, 133].

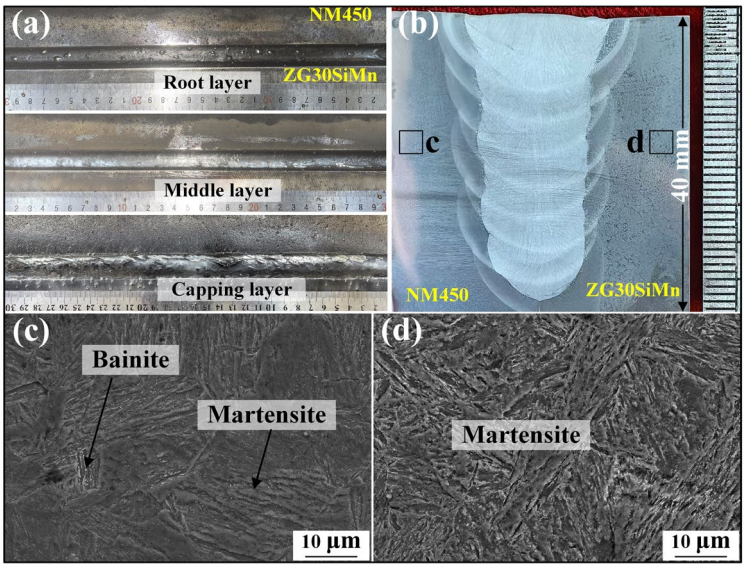


Fig. 4.7. (a) Weld surface appearance and (b) macroscopic cross-section morphology of the welded joint. (c), (d) Microstructures of NM450 and ZG30SiMn, respectively.

4.3.2 Phase and microstructure characteristics of the weld seam

Fig. 4.8(a) presents the macroscopic cross-section of the single-pass welded joint, showing a well-formed appearance. Besides, the base metals melt and mixed with the filler metal, forming a defect-free joint. It is worth noting that the upper surface of the weld seam was concave, a feature conducive for multi-layer welding. Moreover, the grain growth exhibited a distinct orientation, with columnar grains extending from the weld boundary toward the center. Fig. 4.8(b) shows the low-magnification metallographic image obtained via OM, clearly resolving the growth direction. The WM microstructure displayed two distinct zones, evident as dark and bright regions in Fig. 4.8(b). The elongated bright regions were likely identified as proeutectoid ferrite.

Fig. 4.8(c) presents a SEM image of the dark zone marked in Fig. 4.8(b). This region consisted of polygonal ferrite and acicular ferrite. Fig. 4.8(d) shows a magnified view of the acicular ferrite, which exhibited a slender, needle-like morphology. Significantly, oxide particles were embedded within the cores of these acicular ferrite structures, as confirmed by the EDS mapping results. The oxide particles may act as nucleation sites for the acicular ferrite. During austenite cooling, acicular ferrite nucleated at these particles and grew randomly within the austenite grains. Acicular ferrite is an ideal micromorphology, with its nucleation and growth influenced by chemical composition, thermal conditions, and the distribution of nucleating particles[117].

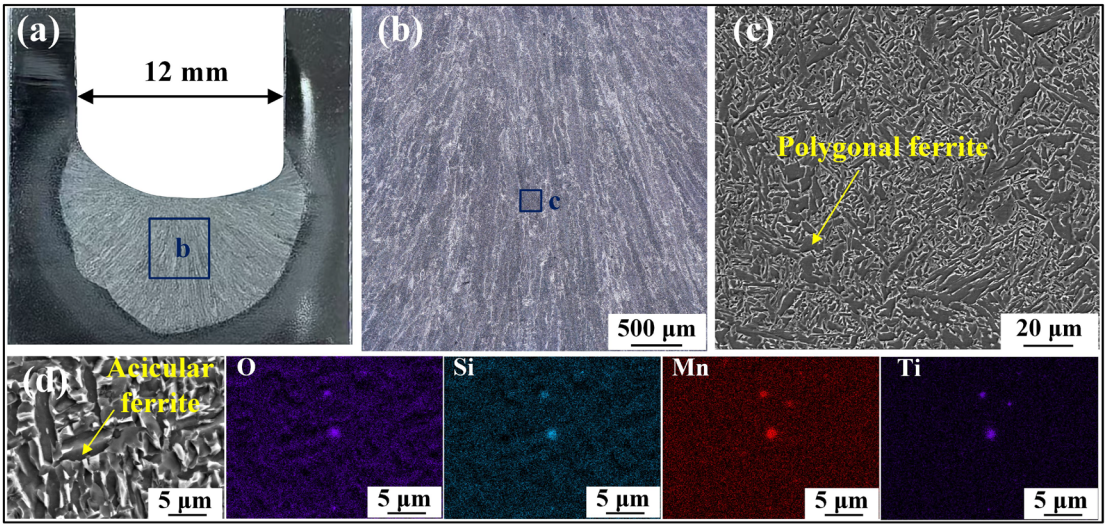


Fig. 4.8. (a) Macrograph of the welded joint cross-section, (b) low-magnification metallographic image of the single-pass filler metal, (c) and (d) high-magnification metallographic images and EDS mapping results, revealing the microstructural details of the single-pass weld deposit.

Fig. 4.9 presents the XRD test results, showing the phase composition of WM. It can be seen that α-phase was the dominant phase in the WM, and γ-phase also exist in the WM, as indicated by the faint peak. The volume fractions of the α-phase and γ-phase, quantified using Jade software, were 97.9 vol%% and 2.1 vol%, respectively.

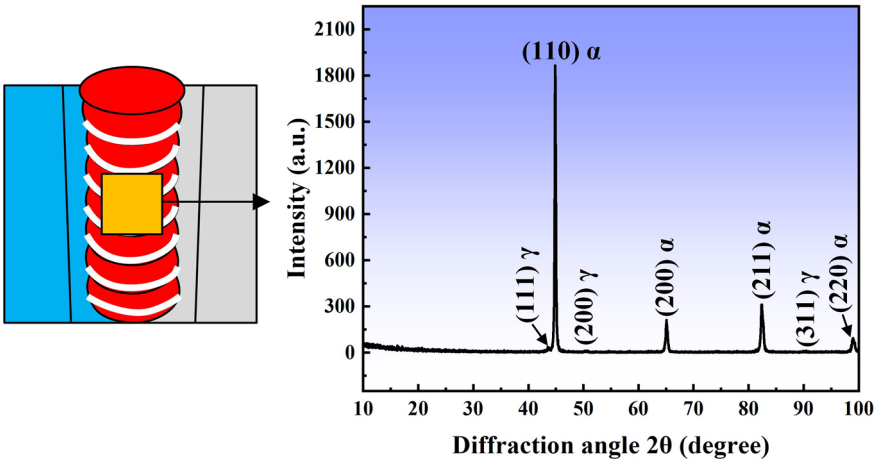


Fig. 4.9. XRD pattern of the WM.

Fig. 4.7(b) shows the periodic white band between the two filling layers from a macroscopic perspective, indicating distinct microstructural characteristics. Fig. 4.10 clearly reveals the microstructures of the white band and filling layer. Fig. 4.10(a) presents a low-magnification metallographic image of the fourth and fifth layers captured by OM. The white band can be clearly seen between the two layers, characterized by color contrast differences. It is worth noting that the grain growth characteristics were different. The filler metal in the fourth and the fifth layers exhibits pronounced columnar growth, whereas the zone between them displays equiaxed grain features. Besides, proeutectoid ferrite is present in the fourth and fifth layers, while it is nearly absent in the central equiaxed zone. Fig. 4.10 (b1), (b2) and (c1), (c2) shows the metallographic images of the columnar grain zone (the area marked “b” in Fig. 4.10 (a)) and equiaxed grain zone (the area marked “c” in Fig. 4.10 (a)), respectively, which were obtained by SEM. In the fifth layer, polygonal ferrite persists, exhibiting a microstructure similar to that of the single-layer WM, whereas it is rarely observed in the equiaxed grain zone. Additionally, the morphology of acicular ferrite changed. Compared to the acicular ferrite in the columnar grain zone (Fig. 4.10 (b2)), the acicular feature in the equiaxed grain zone was weakened and showed a granular feature (Fig. 4.10 (c2)). N. Jousset et al.[134] proposed that the formation of white bands may be attributed to incomplete austenitization during thermal cycling.

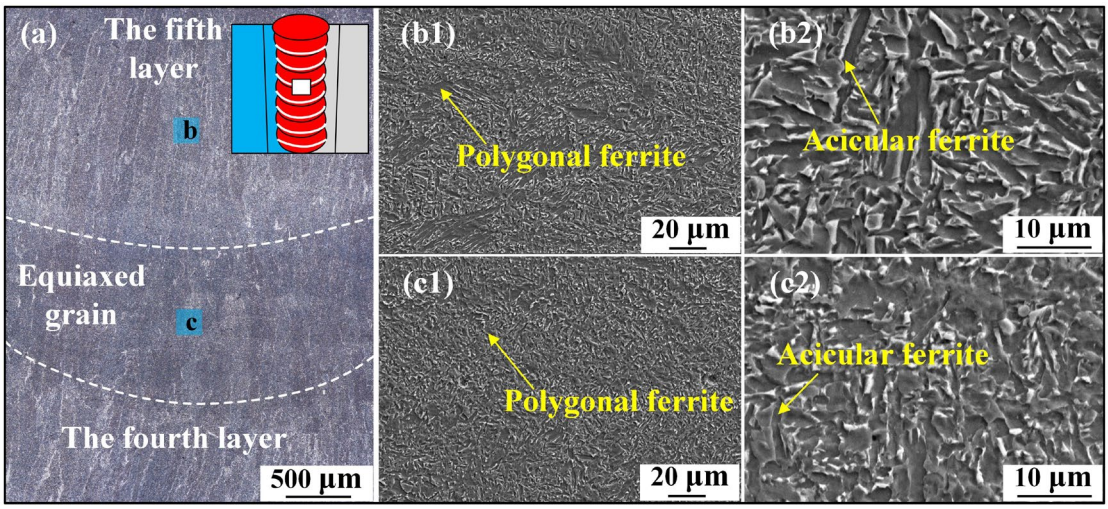


Fig. 4.10. (a) Typical microstructure of the WM, exhibiting columnar grain zone and equiaxed grain zone. (b1), (b2) Microstructure of the columnar grain zone. (c1), (c2) Microstructure of the equiaxed grain zone.

Fig. 4.11 shows the EBSD results, providing more crystallographic insights into the WM of the narrow gap welded joint. Fig 4.11 (a) and (d) depict the inverse pole figures (IPFs) of the columnar grain zone and the equiaxed grain zone, respectively. In Fig. 4.11 (a), large-sized proeutectoid ferrite and polygonal ferrite are visible, with acicular ferrite comprising the remaining phase. In the equiaxed grain zone (Fig. 4.11 (d)), acicular ferrite also displays multiple orientations, but its interlocking characteristics are less pronounced. Fig. 4.11 (b) and (e) present the phase maps of the columnar grain zone and equiaxed grain zone, where green denotes the BCC phase and red denotes the FCC phase. It is worth noting that the phase composition remains consistent across zones. The BCC phase dominates, with only trace FCC phase dispersed in the matrix. This phenomenon may be attributed to retained austenite preserved under faster cooling rates. Fig. 4.11 (c) and (f) shows the kernel average misorientation (KAM) maps and values of the columnar grain zone and equiaxed grain zone. The KAM value of the acicular ferrite is higher than that of the proeutectoid ferrite and polygonal ferrite, as evidenced by color gradients in the KAM map (Fig. 4.11 (c)). Besides, the KAM average values for the columnar grain zone and the equiaxed grain zone are 0.89 and 0.82, respectively. Following thermal cycle and subsequent structural transformation, the KAM value reduces, indicating a reduction in the degree of deformation inside the

crystal.

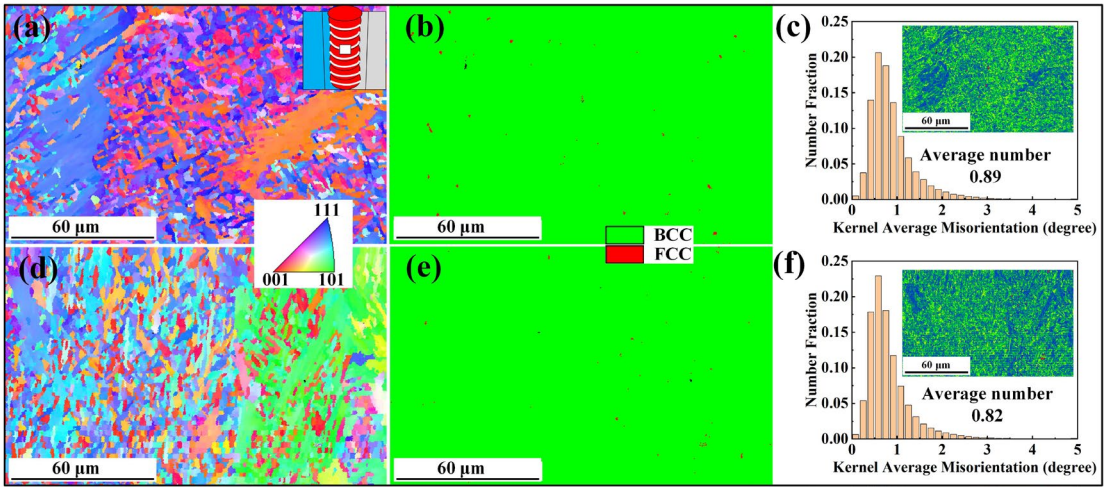


Fig. 4.11. EBSD results of the WM: (a)-(c) IPF map, phase map, and KAM map of the columnar grain zone. (d)-(f) IPF map, phase map, and KAM map of the equiaxed grain zone.

4.3.3 Microstructure characteristics of the HAZ

The WM, HAZ, and BM together constitute the welded joint. Fig. 4.12 (a) and (g) present the low-magnification metallographic images of the welded joint obtained by OM, showing partial WM, the entire HAZ, and partial BM. The HAZ is the region of BM where no melting or solidification occurs, but solid-state phase transformations arise due to welding-induced heat. The HAZ is typically divided into four sub-zones from the WM to the BM based on thermal cycle differences: coarse-grained HAZ (CGHAZ), fine-grained HAZ (FGHAZ), inter-critical HAZ (ICHAZ) and sub-critical HAZ (SCHAZ)[135]. This is because peak temperatures during thermal cycling vary with distance from the heat source. In Fig. 4.12 (a), the zones near NM450 are labeled “b”, “c”, “d”, and “e”, corresponding to CGHAZ, FGHAZ, ICHAZ, and SCHAZ, respectively. Similarly, Fig. 4.12 (f) marks “g”, “h”, “i”, and “j” for the analogous zones near ZG30SiMn. Fig. 4.12 (b)–(e) display SEM images of the NM450 HAZ sub-zones, revealing their typical microstructural features. Both the CGHAZ and FGHAZ exhibit lath martensite, formed from undercooled austenite during rapid cooling. However, differing peak temperatures lead to variations in prior austenite grain size, resulting in larger martensite packet sizes in the CGHAZ compared to the FGHAZ[136]. The

ICHAZ microstructure consists of bainite and martensite[132, 137], while the SCHAZ is dominated by tempered martensite, with white spots observable within martensite laths. As proposed by Xue et al.[135], these spots likely represent carbides precipitated during martensite tempering. For the ZG30SiMn HAZ, the CGHAZ (Fig. 4.12 (g)) and FGHAZ (Fig. 4.12 (h)) feature coarse and fine martensite, respectively. The ICHAZ (Fig. 4.12 (i)) comprises a mixture of martensite and bainite, while the SCHAZ (Fig. 4.12 (j)) also contains tempered martensite, consistent with the NM450 SCHAZ microstructure.

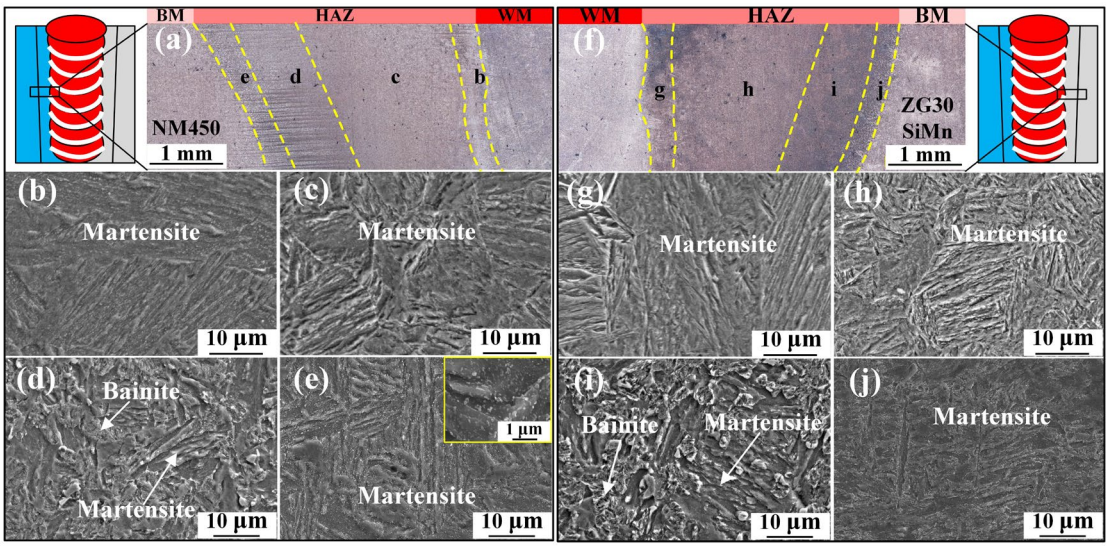


Fig. 4.12. (a), (f) Low-magnification OM images of the welded joint, depicting partial WM, entire HAZ, and partial BM. (b)-(e) CGHAZ, FGHAZ, ICHAZ and SCHAZ of NM450. (g)-(j) CGHAZ, FGHAZ, ICHAZ, and SCHAZ of ZG30SiMn.

4.3.4 Thermal induced microstructure evolution of the welded joint

In order to study the effects of thermal cycles on the microstructure of the welded joint. The temperature data of the WZ fourth layer and the two HAZs were extracted (Fig. 4.13(a)) and plotted into curves. Fig. 4.13 (b) was the thermal cycle curve of the center of the WZ. It can be seen that the filling metal underwent a process of melting, solidification and solid phase transformation. Besides, the temperature values of the thermal cycle gradually decreased with the increase of filling height. This rule applied to the eight filling layers. However, it should be noticed that the filling thickness of each layer is about 5mm, resulting in the differences in the thermal cycles experienced

from the top to the bottom of one weld seam, especially the difference in temperature peak values. The inset in Fig. 4.13 (b) showed the subsequent thermal cycles of the fourth filling layer from top to bottom at every 1 mm. It was worth noting that the temperature peak values were significant different. The peak value decreased from 1586 ℃ at 1 mm area to 747 ℃ at 5 mm area, indicating that the states of different areas in the weld seam were different. At the top area, the temperature peak value exceeded the melting point of the filling metal, resulting in the remelting of the weld seam. The area where the temperature peak value exceeded the Ac3 temperature was completely austenitized and transformed into proeutectoid ferrite and acicular ferrite again. The area with the peak temperature between Ac3 temperature and Ac1 temperature underwent incomplete austenitization, and the austenite transformed into acicular ferrite with granular characteristics, which contributed to the appearance of the white strips. Additionally, the area with the peak temperature lower than Ac1 temperature may not undergo significant solid-state phase transition. Since the subsequent thermal cycle temperature peak values were smaller than the Ac1 temperature, all subsequent thermal cycles do not have a significant effect on the fourth layer

Unlike the filling layer, BM underwent the thermal cycles of each welding. Fig. 4.13 (c)-(f) showed temperature field data extracted in the 0.5 mm, 1 mm, 2 mm, and 2.5 mm regions beyond the fusion line, which correspond to CGHAZ, FGHAZ, ICHAZ and SCHAZ, respectively. It can be seen that the temperature peak values increased first and then decreased with the progress of welding, which depended on the distance from the heat source. The thermal cycle temperature peak values of the third filling, fourth filling and fifth filling welding were worth noting because the three temperature peak values were higher, which may result in phase transformation. In CGHAZ, the temperature peak value of the third filling was much higher than the austenitizing temperature, and the material underwent phase transition. At the fourth filling, the temperature peak value of the thermal cycle was the highest, the material is re-austenitic, and the austenite was coarse due to the higher peak temperature value. In the subsequent

cooling process, austenite transformed into coarse martensite at a faster cooling rate. At the fifth filling, the temperature is lower than the austenitizing temperature, and no significant microstructure changes occur. However, the tempering effect was generated on the martensite, which would also occur in subsequent filling processes. FGHAZ underwent a similar thermal cycle as CGHAZ, but the lower temperature peak value resulted in a finer martensite structure. The temperature peak value of the thermal cycle of ICHAZ is between Ac3 temperature and Ac1 temperature, and part of the material undergo austenitic transformation and form bainite during cooling. At SCHAZ, the peak temperature of the thermal cycle is lower than AC1. At this time, the martensitic structure is subjected to tempering effect and transforms into tempered martensite. It is worth noting that the temperature characteristics of only one spot were analyzed in each zone of HAZ, and the characteristics of different parts would be different. The above analysis was applicable to both NM450 and ZG30SiMn because of the slight differences between the two materials.

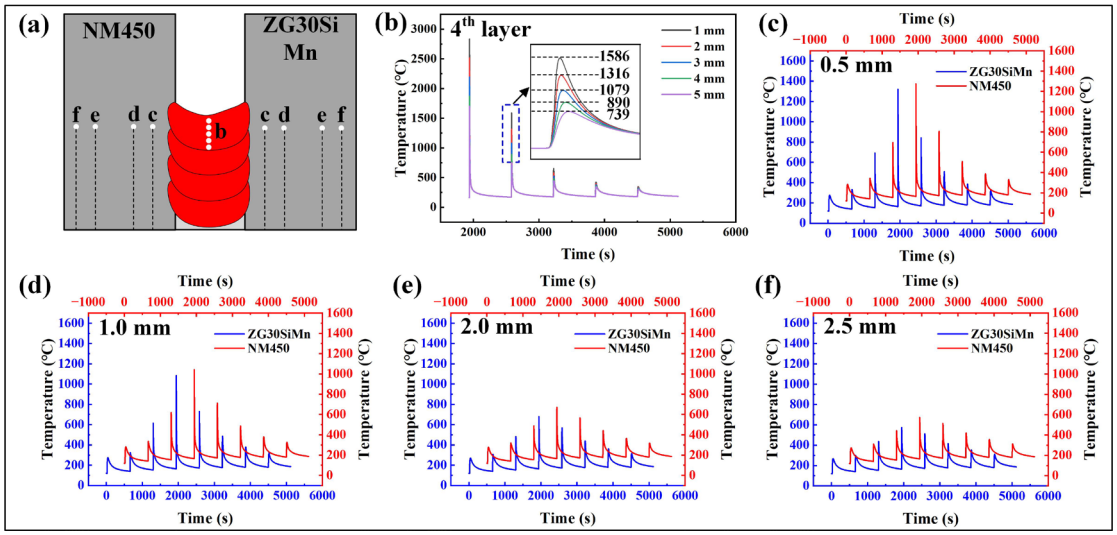


Fig. 4.13. Thermal cycle curves of different areas of thick plate joints: (a) Schematic diagram of temperature data extraction position, (b) fourth layer weld seam, (c) CGHAZ, (d) FGHAZ, (e) ICHAZ, (f) SCHAZ.

4.4. Comprehensive evaluation of mechanical properties in welded joint

4.4.1 Microhardness

Fig. 4.14(a) shows the microhardness distribution of the WM from the root layer to

the capping layer. The microhardness values exhibit a decreasing trend from the bottom to the top of the weld. This trend is correlated with grain size evolution, which compares the microstructures of the bottom, middle, and top layers. The microstructures transition from relatively dense and fine-grained in the bottom layer to progressively coarsened in the top layer. This structural coarsening is likely attributed to progressively elevated interpass temperatures (Fig. 1(c)), promoting heat accumulation during multi-layer welding. Such thermal conditions facilitate grain growth and degrade mechanical properties. Fig. 4.14 (b) shows the microhardness distribution across different zones of the welded joint. The WM exhibits the lowest microhardness value. In the HAZ, the microhardness follows the order: CGHAZ > FGHAZ > ICHAZ > SCHAZ, which is closely linked to the HAZ's complex microstructural characteristics. Variations in prior austenite grain size and the presence of tempered microstructures are key factors influencing these hardness differences[7]. This hardness distribution pattern aligns with findings reported by Zhang et al.[132]. Notably, this distribution characteristic is consistent for both BMs.

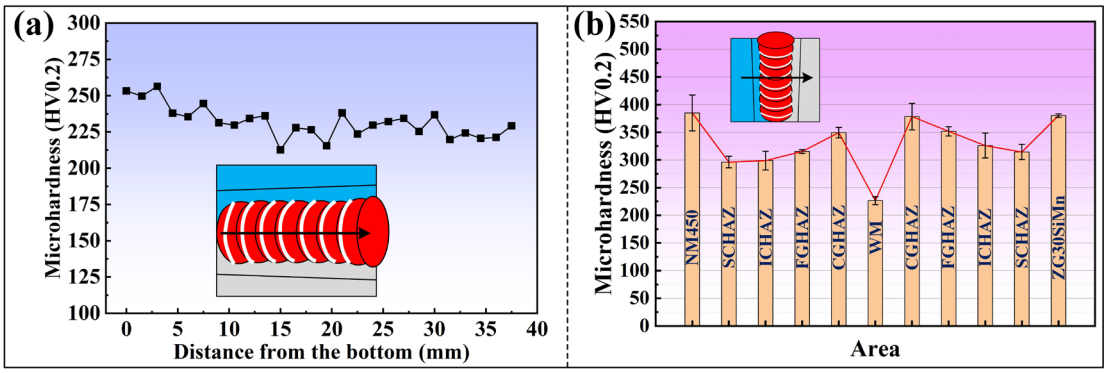


Fig. 4.14. (a) Microhardness distribution from the bottom to the top of the WM. (b) Average microhardness values of different welded joint zones.

4.4.2 Tensile properties

Fig. 4.15 shows the tensile test results for the welded joint. Fig. 4.15(a) illustrates the engineering stress-strain curve, indicating that the welded joint withstood high loads and exhibited significant deformation before fracture. The average ultimate tensile strength (UTS) of three test samples was 708.11 ± 9.85 MPa, matching the specified strength of the welding wire, The average elongation (EL) was 25.42 ± 1.48 %,

exceeding the wire's nominal value. Fig. 4.15(b) depicts the appearance of the fractured tensile samples. The samples failed at the center of the WM, displaying evident plastic deformation. Fig. 4.15(c) shows a SEM image of the fracture morphology. The necking phenomenon is clearly observable, which is manifested as a reduction in the tensile samples's cross-sectional area. Fig. 4.15 (d) provides a magnified view of the area marked "d" in Fig. 4.15(c). Notably, the fracture surface is characterized by numerous dimples. Additionally, particles visible at the base of these dimples were identified via EDS as oxide particles (Fig. 4.15(e)). These particles likely formed from oxygenophilic elements combining with oxygen in the high-temperature molten pool and becoming embedded in the matrix. The pronounced necking and abundant dimples indicate a ductile fracture mode. During deformation, microvoids nucleated at these particle, progressively grew, and coalesced under tensile stress until final fracture occurred. Table 4.3 summarizes the tensile properties of the welded joint. In this study, the use of mismatched weld metal resulted in fracture within the weld region. The selected low-alloy high-strength steel welding wire exhibited varying tensile properties under different heat input conditions, as heat input influences acicular ferrite size and proeutectoid ferrite volume fraction. While the deposited metal's strength met the specified wire strength and service requirements, future work will focus on optimizing heat input to further enhance tensile strength.

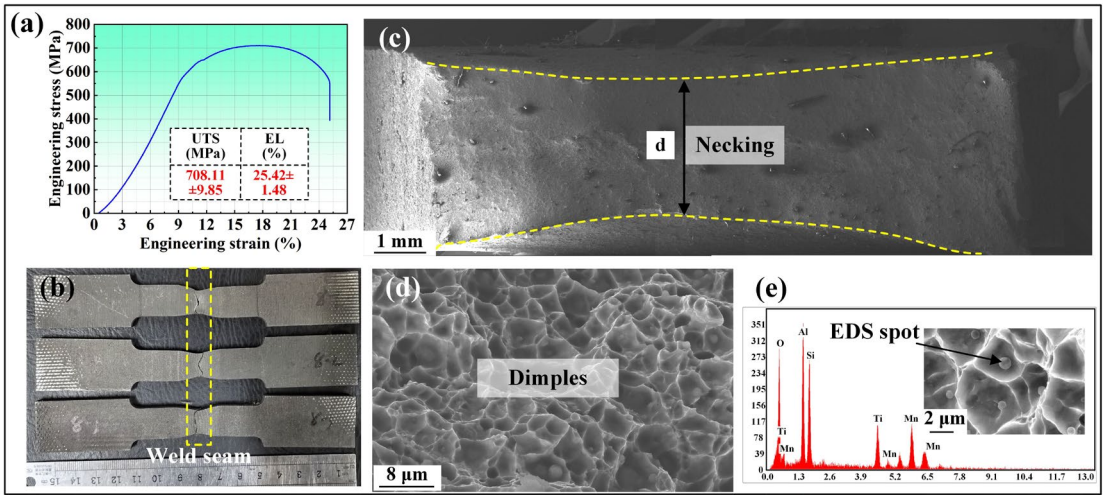


Fig. 4.15. Tensile test results of the welded joint: (a) engineering stress-strain curve, (b) appearance of the fractured tensile samples, (c), (d) SEM observations of the fracture

surface, (e) EDS result of the fracture surface.

Table 4.3. Summary of the tensile test results.

UTS (MPa)	EL (%)	Fracture location	Joint efficiency (%)
708.11 ± 9.85	25.42 ± 1.48	Weld	65.4

4.4.3 Impact toughness

Fig. 4.16(a)-(c2) show the appearance and fracture surfaces of the fractured impact samples from the WM, HAZ near NM450, and HAZ near ZG30SiMn, respectively. The impact absorption energy values for the three regions were, 167.8 ± 9.4 J, 52.5 ± 3.8 J, and 46.5 ± 9.4 J, respectively. Within the entire welded joint, the WM exhibited the highest impact toughness. The HAZ impact toughness was comparable to that of the BMs, achieving 86%–110% of the BMs' toughness, thereby meeting the service requirement (≥80% of BM). Macroscopic fracture morphology of WM and HAZ impact samples (Fig. 4.16(a1), (b1), and (c1)) revealed distinct behaviors: the WM sample displayed significant plastic deformation with a large fibrous zone, whereas both HAZ samples exhibited flat fracture surfaces with smaller fibrous zone proportions, indicating different fracture modes. SEM observations of the fracture surfaces for the three samples were shown in Fig. 4.16(a2), (b2), and (c2). The WM fracture surface was dominated by abundant dimples, indicative of a ductile fracture mode, which correlates with its acicular ferrite microstructure[117]. In contrast, the HAZ samples exhibited a ductile-brittle mixed fracture mode, characterized by predominant cleavage facets and sparsely distributed small dimples. The presence of cleavage facets is associated with reduced crack initiation and propagation energy, leading to lower impact toughness. This is a common phenomenon in the HAZ of high-strength steels[138].

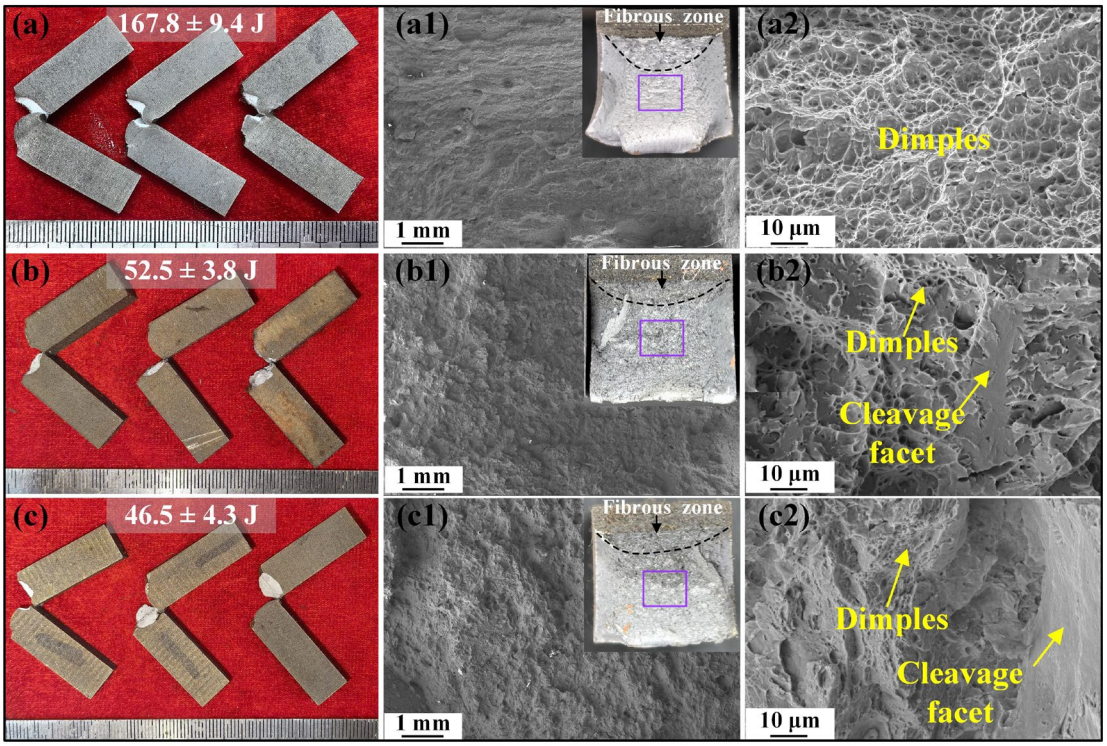


Fig. 4.16. Impact test results for (a-a2) WM, (b-b2) HAZ near NM450, and (c-c2) HAZ near ZG30SiMn.

4.4.4 Bend properties

Bend samples were extracted from the welded structure via wire-cut electrical discharge machining, and three-point bending tests were performed with a universal testing machine in accordance with GB/T 2653-2008 to assess the metallurgical bonding between the filler metal and base metals. As shown in Fig. 4.17(a), the schematic illustrates the cutting location and dimensions of the bend samples. During the bending test, the crosshead displacement was set to 30 mm. Comparative visual inspection of the samples before and after bending (Fig. 4.17 (b)) revealed no detectable cracks or delamination at the filler metal–base metal interface. This absence of interfacial failure confirms the robustness of the welding process and the effective metallurgical bonding achieved.

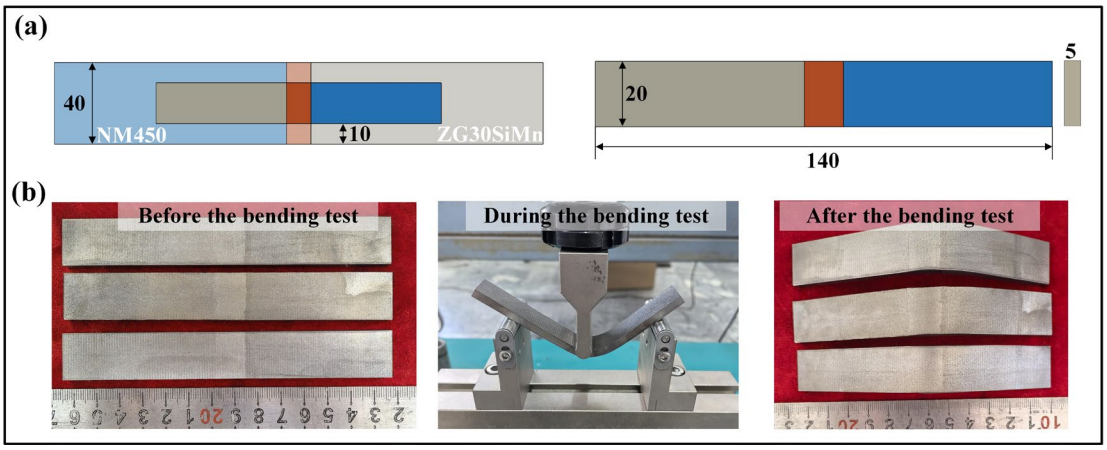


Fig. 4.17. (a) Samples cutting location and dimensions for the bending test. (b) Appearance of the samples before, during, and after the bending test.

4.5. Summary

This study utilized double-wire GMAW to weld 40-mm-thick chute structure materials namely wear-resistant steel NM450 and cast steel ZG30SiMn. An in-depth exploration was carried out on the welding process, microstructure, and properties of the welded joint. The detailed findings are as follows:

(1) Under the selected process parameters, the continuous spray transfer of the molten welding wire was successfully achieved, which in turn ensured a stable welding process. As a result, a welded joint free of defects was obtained.

(2) The WM microstructure comprised proeutectoid ferrite, polygonal ferrite, and a large amount of acicular ferrite. Owing to the thermal cycles, a white band emerged between the filling layers. In this region, the content of proeutectoid ferrite dropped, and the acicular feature of the acicular ferrite was less distinct.

(3) The microhardness shows a gradual downward trend from the bottom layer to the top layer. This phenomenon is related to the coarsening of the microstructure, which is caused by heat accumulation during the welding process. Moreover, the weld metal demonstrates better ductility and toughness.

(4) Based on the distinct microstructures resulting from the characteristics of the thermal cycle, the HAZ can be divided into four zones: the CGHAZ, FGHAZ, ICHAZ, and SCHAZ. The main microstructures of these four zones are coarse martensite, fine martensite, a mixture of bainite and martensite, and tempered martensite, respectively. In the HAZ, the microhardness of the CGHAZ is the highest, followed by that of the FGHAZ, ICHAZ, and SCHAZ. The HAZ exhibits higher strength, and its toughness

reaches 86%-110% of that of the BMs.

(5) Compared with the conventional welding process used in production, the double-wire narrow gap welding enhances welding efficiency while ensuring defect-free joints. The performance of the welded joints meets the specified requirements, notably with toughness exceeding 80% of BMs' values. The application of double-wire narrow gap welding in the manufacturing of chute structures holds significant practical importance.

Chapter 5. Wear performance and microstructures of Fe-Cr-C alloy cladding on heterogeneous welded joint of NM450/ER70-G/ZG30SiMn

5.1. Cladding conditions and material

5.1.1 Cladding experiment setup

The substrate material for the arc cladding experiment was a narrow-gap welded joint (NM450/ZG30SiMn dissimilar steel joint filled with ER70-G weld metal (WM)). Both the NM450 and ZG30SiMn base metals (BMs) were 400 mm in length, 100 mm in width, and 40 mm in thickness; whereas the width of the rectangular narrow-gap groove was 12 mm. The NM450/ER70-G/ZG30SiMn dissimilar steel narrow-gap welded joint was prepared by gas metal arc welding (GMAW). To simulate actual production conditions, the welded joints underwent heat treatment. A KB968 solid wire with a diameter of 1.2 mm was employed as the cladding filler material, the chemical compositions of which are listed in Table 5.1. The KB968 wire contains moderate levels of Cr and C, ensuring sufficient formation of Cr-C wear-resistant phases while preventing excessive hard phases that could induce cracking in the cladding layer.

Table 5.1. Chemical compositions of cladding materials (wt.%).

	Fe	Cr	Nb	Si	Mn	C
ZG30SiMn	Bal.	0.43	-	0.64	1.39	0.28
NM450	Bal.	0.86	-	0.35	1.61	0.21
ER70-G	Bal.	0.30	-	0.30	1.45	0.10
KB968	Bal.	13.5	7.00	1.50	2.00	3.50

The gas metal arc cladding experiments were carried out by a FANUC industrial robot that was fitted with a MEGMEET melted electrode welding machine. Before cladding, the surface of the dissimilar steel welded joint was mechanically polished by an angle grinder to remove impurities and ensure a consistent surface flatness, and then further cleaned by absolute ethyl alcohol. Single-layer multi-pass cladding experiments were conducted under various currents, with detailed process parameters provided in Table 5.2. During cladding, a unidirectional travel path (from ZG30SiMn to NM450,

as illustrated in Fig. 5.1(a)) was maintained, with a constant overlap ratio of 20% and an inter-pass cooling time of 5 minutes. The wire stick-out length was set to 17 mm, and pure CO_2 shielding gas was supplied at a flow rate of 20 L/min.

Table 5.2. Detailed cladding parameters.

	Average current	Peak current	Base current	Pulse frequency	Voltage	Deposition speed	Wire feed speed
#1	180 A	197 A	75 A	140 Hz	29 V	400 mm/min	9 m/min
#2	240 A	254 A	126 A	140 Hz	33 V	400 mm/min	12 m/min

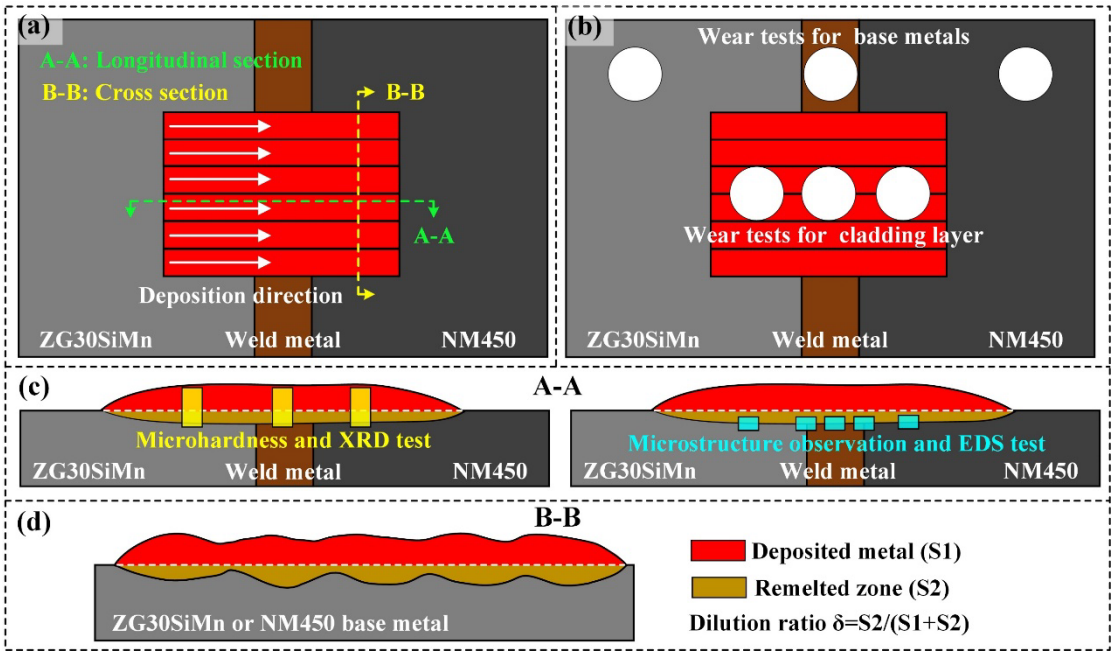


Fig. 5.1. Schematic illustration of the cladding process: (a) deposition strategy, (b, c) wear test and material characterization sampling methodology, and (d) dilution ratio calculation approach.

5.1.2 Material characterization

After the cladding experiments, metallographic specimens were extracted from both the longitudinal and transverse cross-sections of the cladding layer using wire electrical discharge machining to observe the macrostructures and microstructures. The sampling orientations are schematically illustrated in Fig. 5.1(a). The specimens were ground by 80# ~ 2000# sandpapers, followed by diamond polishing paste with a diameter of 2.5 μm, finally etched with $FeCl_3$ + HCl + H_2O reagent ($FeCl_3$: 5 g, HCl: 50 ml, and H_2O: 100 ml) for 15 s to reveal the microstructure, which was subsequently examined using optical microscopy (OM, OLYMPUS DSX510).

Due to the dissimilar steel welded joint (NM450/ER70-G/ZG30SiMn), the cladding layer formed three distinct heterogeneous interfaces: NM450/cladding layer, ER70-G/cladding layer, and ZG30SiMn/cladding layer. Additionally, two compositional mixing zones were observed: NM450/ER70-G/cladding layer and ER70-G/ZG30SiMn/cladding layer. Microhardness testing (Vickers hardness tester, HVS-1000) and X-ray diffraction (XRD, DX-2700) analysis were performed on the three interfaces. The hardness measurements were conducted under a 200 g load for 15 s, with a 0.2 mm spacing between indentations. XRD scans were performed over a 2θ range of 20° ~ 100° at a scanning rate of 2 °/min. Furthermore, scanning electron microscopy (SEM, MERLIN COMPACT) equipped with energy disperse spectroscopy (EDS) was employed to analyze the phase composition across all three interfaces and two mixing zones. The sampling strategy for material characterization is depicted in Fig. 5.1(c), while the methodology for calculating the cladding layer dilution ratio (δ) is illustrated in Fig. 5.1(d).

5.1.3 Wear resistance evaluation

In order to access the wear resistance, friction and wear tests were conducted in this study, as they are widely adopted and convenient approaches for evaluating wear behavior. Wear testing was conducted under a 10 N normal load using GCr15 steel as the counter face material, with a rotational speed of 500 rpm per minute and a wear track radius of 5 mm. The wear resistance was comprehensively evaluated through: friction coefficient calculation, weight loss measurement, and worn surface morphology analysis (via SEM microscopic examination). The coefficient of friction can be used to reveal the nature of surface interaction, and mass loss quantifies the severity of material degradation. To ensure accurate evaluation of the wear resistance performance of the cladding layers, specimens were sampled from the cladding layers of three distinct zones (NM450, ER70-G, and ZG30SiMn). Concurrently, wear resistance tests were conducted on their corresponding base materials (NM450, ER70-G, and ZG30SiMn), as depicted in Fig. 5.1(b). The wear test specimens were machined to dimensions of 5 mm in thickness and 15 mm in diameter.

5.2. Macrostructure characteristics of the cladding layer

5.2.1 Macro-morphology of the cladding layer

Fig. 5.2(a) and (b) present the macroscopic morphology of cladding layers deposited under different cladding parameters. All cladding conditions produced straight, continuous layers without visible cracks, confirming the suitability of the selected KB968 wire. Due to the narrow width of the ER70-G WM and the predominant base materials (ZG30SiMn and NM450), cross-sectional analysis focused on the ZG30SiMn and NM450 regions, with sampling locations marked by green dashed rectangles in Fig. 5.2(a) and (b). Cladding layer thickness was measured at three random locations to minimize statistical error. At lower currents, the average thickness measured 2.33 ± 0.18 mm of the ZG30SiMn region and 2.42 ± 0.24 mm of the NM450 region, while at higher currents the corresponding values were 2.30 ± 0.19 mm and 2.21 ± 0.08 mm, respectively. The thickness variation between regions of the same cladding layer remained within 5%, demonstrating good surface uniformity. Notably, despite higher heat input and faster wire feed rate, no significant increase in cladding thickness was observed. Instead, a slight decrease occurred compared to the lower-current condition. This phenomenon suggests that increased heat input enhanced base material remelting, resulting in a larger remelting zone. The enhanced remelting effect directly influenced compositional mixing between the cladding layer and base material. Therefore, the dilution ratio was subsequently measured. At lower currents, the dilution ratios of the ZG30SiMn and NM450 regions were 29.8% and 31.1%, respectively, while at higher currents, these values increased to 41.2% and 45.2%, indicating greater dilution ratio with higher heat input. Additionally, porosity was observed to decrease at higher heat input, likely due to prolonged molten pool duration facilitating more effective gas escape. The varied dilution ratio under different cladding parameters indicated distinct elemental diffusion and interfacial mixing behaviors, suggesting corresponding microstructural modifications that warrant further investigation.

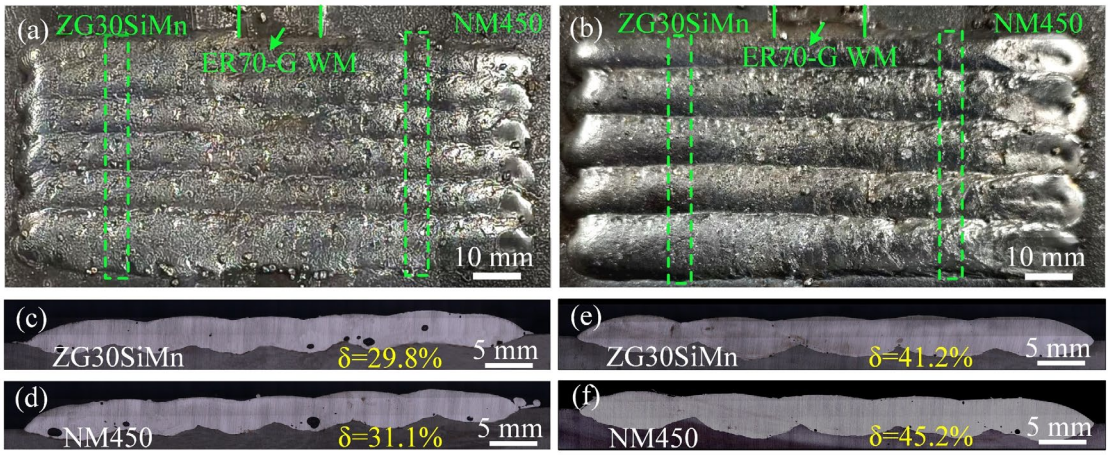


Fig. 5.2. Macro-morphology of the cladding layer: (a, b) general macro-morphologies at different cladding parameters, (c, d) cross-sectional morphologies of the ZG30SiMn and NM450 regions at low dilution ratios; (e, f) cross-sectional morphologies of the ZG30SiMn and NM450 regions at high dilution ratios.

5.2.2 Metallographic observation of the cladding layer

Fig. 5.3 presents the longitudinal section analysis of the low-dilution-ratio cladding layer, revealing microstructural characteristics across three heterogeneous interfaces: NM450/cladding, ER70-G/cladding, and ZG30SiMn/cladding. Metallographic examination demonstrates excellent interfacial bonding without cracking at all interfaces, confirming good compatibility between the selected wire and base materials. The microstructural evolution along the build direction shows a clear transition from prominent columnar grains in the bottom region to equiaxed grains in the middle and top sections. This gradient structure results from varying thermal conditions: the bottom region, being farthest from the heat source with optimal heat dissipation, experiences the highest thermal gradient, favoring columnar growth. Notably, white precipitates were observed to be non-uniformly distributed across all three interfaces, with apparently higher density in the NM450 region. Comparative analysis with Sousa et al.'s work on Fe-22Cr-5.5C alloy deposition (where similar precipitates were identified as M7C3 carbides) suggests these are likely carbide phases[139]. The observed variation in precipitate density may result from NM450's higher Cr content (approximately 0.8 wt.%) compared to ZG30SiMn and ER70-G (typically <0.5 wt.%

Cr), which would enhance carbide formation during solidification.

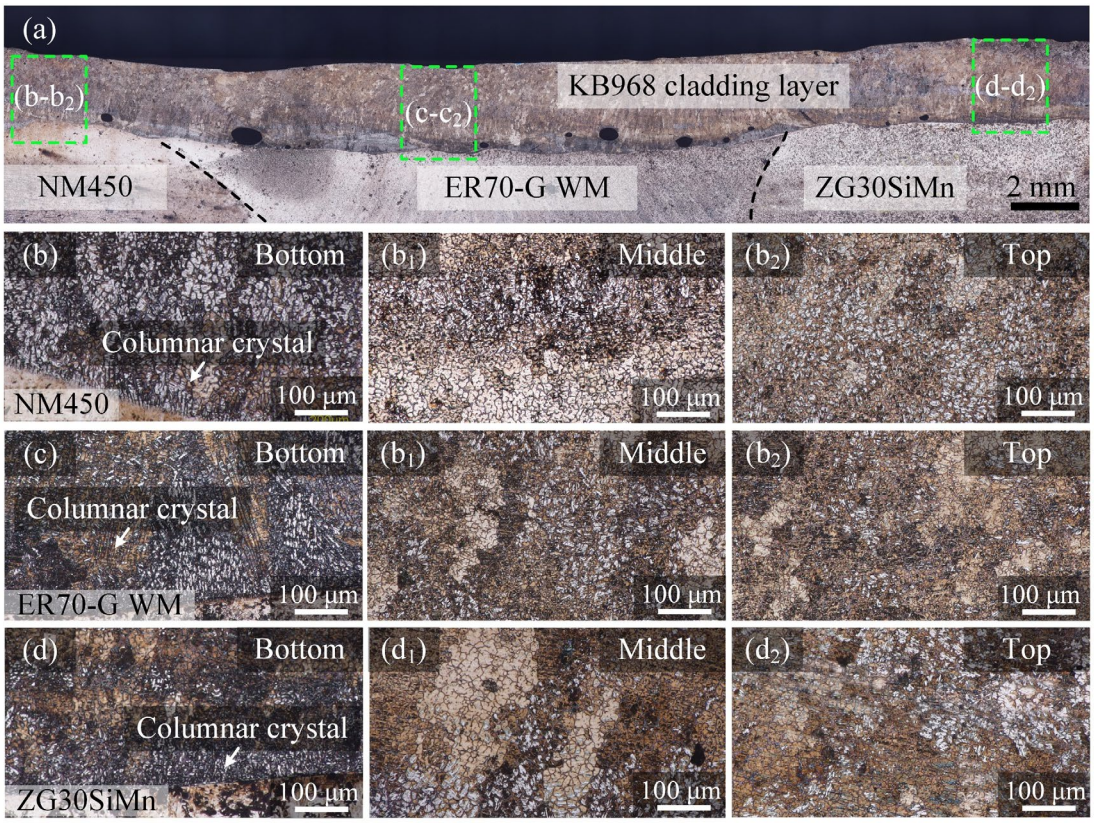


Fig. 5.3. Optical micrographs of the longitudinal section of the low-dilution-ratio cladding layer: (a) macroscopic overview; (b-b_2) across different height zones in the NM450 region (b: bottom, b_1: middle, b_2: top); (c-c_2) corresponding zones in the ER70-G region; (d-d_2) corresponding zones in the ZG30SiMn region.

Fig. 5.4 shows the longitudinal section analysis of the high-dilution-ratio cladding layer, revealing crack-free interfaces with all three base materials (NM450, ER70-G, and ZG30SiMn). The prolonged molten pool duration (attributed to higher heat input) in this condition reduced the thermal gradient, resulting in weaker columnar crystal characteristics at the cladding layer bottom compared to the low-dilution sample. Microstructural examination showed significantly more numerous and uniformly distributed white carbide precipitates throughout the NM450, ER70-G, and ZG30SiMn regions. However, a distinct vertical gradient in carbide precipitation was observed, with precipitate density increasing progressively from bottom to top. This distribution pattern directly correlates with the thermal history during cladding. The top zone, benefiting from direct arc heating and final solidification, maintained optimal

conditions for carbide nucleation, while the bottom region's relatively rapid cooling limited carbide growth. Furthermore, the intense elemental mixing in the bottom region of the cladding layer — a consequence of high dilution ratio—led to substantially reduced Cr concentration, thereby substantially inhibiting carbide formation in this zone.

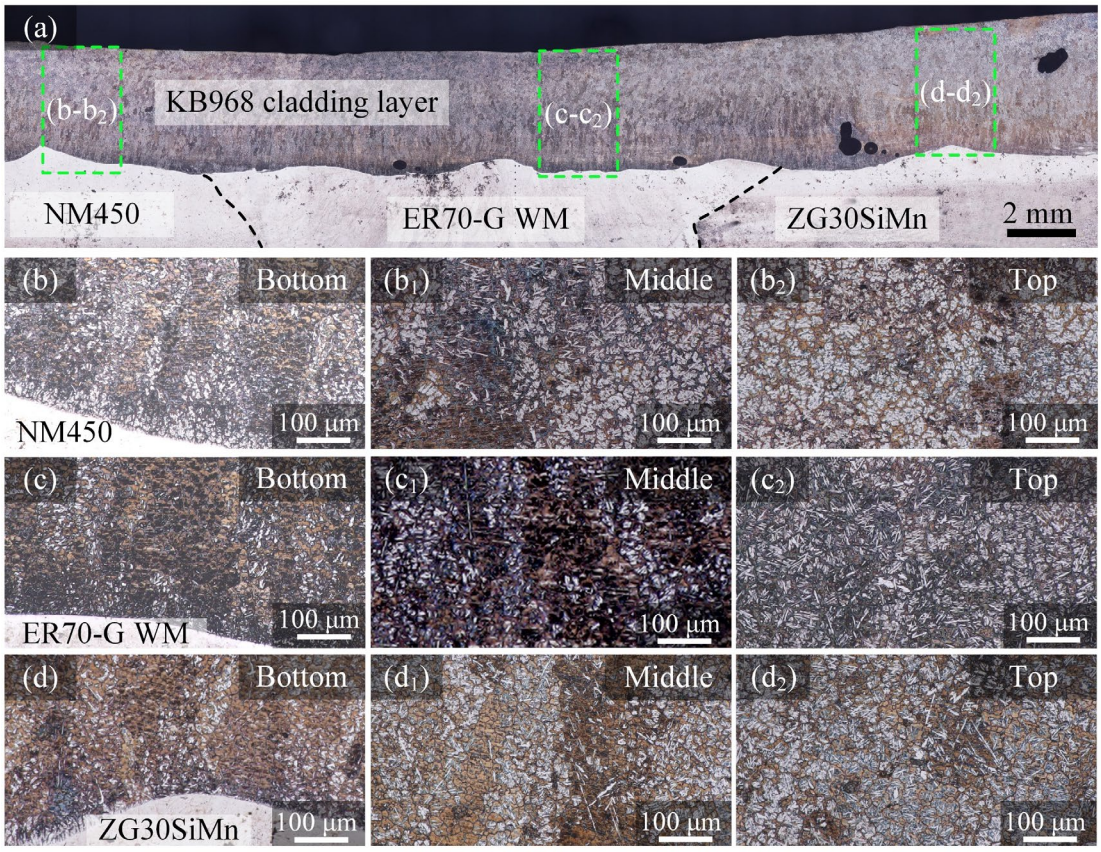


Fig. 5.4. Optical micrographs of the longitudinal section of the high-dilution-ratio cladding layer: (a) macroscopic overview; (b-b_2) across different height zones in the NM450 region (b: bottom, b_1: middle, b_2: top); (c-c_2) corresponding zones in the ER70-G region; (d-d_2) corresponding zones in the ZG30SiMn region.

To determine the fundamental phase composition of the cladding layer, XRD analysis was conducted on the three distinct regions of the NM450, ER70-G, and ZG30SiMn. The XRD specimens, measuring 2.5 mm in length, were carefully prepared to encompass both the deposited zone and remelted zone while minimizing interference from the base materials. As shown in Fig. 5.5, the XRD patterns reveal that the cladding layer primarily consisted of an Fe matrix accompanied by various carbides including

Fe4C, Fe3C, Cr23C6, Cr3C2, and Cr7C3. Comparative analysis demonstrates that the ER70-G region exhibited relatively fewer carbide peaks compared to the NM450 and ZG30SiMn regions, which can be attributed to its lower Cr content (as indicated in Table 5.1). While the variation in dilution ratio did not alter the fundamental phase species of the cladding layer, the high-dilution condition resulted in enhanced diffraction peak intensities of Cr23C6. This observation confirms the increased carbide precipitation previously observed via optical microscopy. The XRD result suggests that higher dilution ratio promoted more extensive carbide formation without changing the types of phases present.

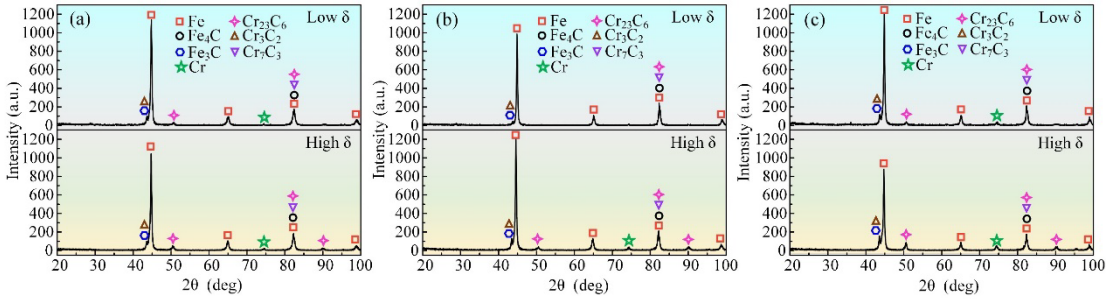


Fig. 5.5. XRD analysis results of different regions under low and high dilution ratios: (a) in the NM450 regions; (b) in the ER70-G regions; (c) in the ZG30SiMn regions.

Since the upper surface of the cladding layer, acting as the working surface, is directly subject to wear under external forces, we specifically observed the upper surface using an optical microscope, with the results shown in Fig. 5.6. Fig. 5.6(a-c) presents the morphologies of the upper surface of the cladding layer under low-dilution condition. When compared with the ER70-G and the ZG30SiMn regions, the NM450 region exhibited the largest number of carbides with the most uniform distribution. In contrast, the ER70-G and the ZG30SiMn regions showed extremely uneven carbide distribution, with a considerable portion showing almost no carbide precipitation. This indicates that the composition of base materials has a significant impact on the phase composition and wear resistance of the cladding layer — if the base material contains higher contents of elements such as Cr and C, it is more conducive to the precipitation and growth of carbides. While under high-dilution condition, the number of carbides increased significantly and their distribution uniformity was greatly improved, as

shown in Fig. 5.6(d-f). Furthermore, the upper surfaces of the NM450, ER70-G, and ZG30SiMn regions exhibited approximately similar carbide distribution morphologies. This phenomenon indicates that the growth tendency of carbides was enhanced under such condition, and the discrepancy in carbide precipitate quantities caused by variations in base material composition was effectively reduced.

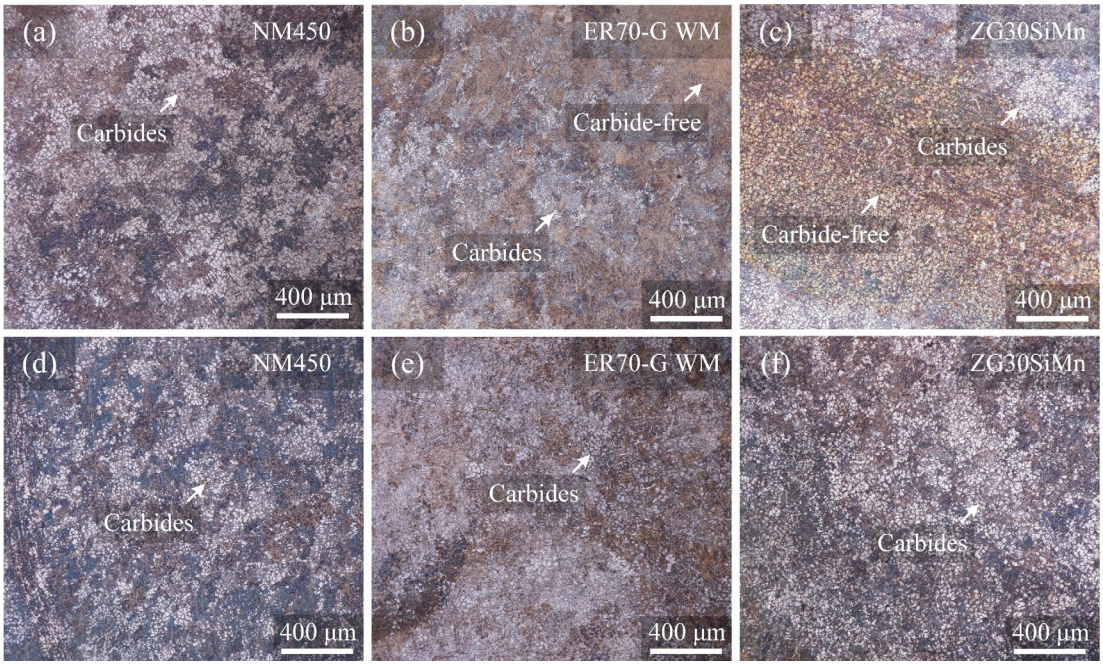


Fig. 5.6. Optical micrographs of the upper surface: (a-c) correspond to the NM450, ER70-G, and ZG30SiMn regions under low dilution ratios; (d-f) correspond to the NM450, ER70-G, and ZG30SiMn regions under high dilution ratios.

5.3. Microstructure characteristics of the cladding layer

5.3.1 Microstructure characteristics at the NM450/cladding layer interface

While optical microscopy and XRD analysis can characterize the macroscopic structure of the cladding layer, a more detailed investigation is required to clarify the microstructural distribution characteristics of the heterogeneous interface under varying dilution ratios. Fig. 5.7 illustrates the microstructure of the NM450/cladding layer interface, with corresponding EDS results summarized in Table 5.3. A continuous white precipitated phase was observed along the grain boundaries, whereas two distinct contrasts — white and dark gray — were evident inside the grains. EDS analysis revealed that the NM450 base material adjacent to the interface contained

approximately 5.1 wt.% Cr, with the elevated Cr content primarily attributed to element mixing with the welding wire. Specifically, the dark gray intragranular phase exhibited a Cr content of ~10.5 wt.%, while the white intragranular phase and white grain boundary phase contained ~15.3 wt.% and ~29.6 wt.% Cr, respectively. A clear correlation was observed between phase contrast and Cr content: white phases corresponded to higher Cr concentrations, with the grain boundary phase exhibiting the highest Cr content, followed by intragranular white precipitates. Buytoz et al.[140] demonstrated that in Fe-Cr-C alloy cladding, austenite was the primary solidification phase; as the temperature decreased further, primary austenite rejected C and Cr into the remaining liquid. Since grain boundaries are typically the last regions to solidify, they tend to accumulate higher carbide contents. Consequently, carbides frequently generate at the grain boundaries[141]. Additionally, carbide formation is strongly dependent on Cr content, as Cr acts as a potent nucleation promoter for carbides, whereas Fe exhibits significantly weaker promoting effects on carbide nucleation[142]. The spatial distribution of Cr effectively indicated the carbide distribution, and the white precipitates (at grain boundaries and inside the grains) with high Cr concentrations were highly likely to be carbides. Chuang et al.[99] demonstrated that M23C6 carbides nucleated and grew through a peritectic reaction between the residual liquid and M7C3 carbides. These M23C6 carbides were observed to form at the periphery of the M7C3 carbides[97], and further analysis revealed that they exhibited a lower Cr content compared to M7C3 carbides[82, 98]. Based on XRD and SEM results, combined with previous literature findings, the intergranular carbides were identified as Cr7C3, whereas the intragranular carbides were determined to be Cr23C6. In contrast, the dark gray intragranular phases with lower Cr concentrations were attributed to (Fe, Cr) solid solutions. With increasing distance from the interface, the proportion of intragranular Cr23C6 carbides gradually decreased. Near the top of the cladding layer, almost no intragranular carbides were observed, with carbides predominantly distributed along grain boundaries (Fig. 5.7(b) and (c)). Given that the top region exhibited the lowest degree of element mixing with the base material, the reduced

carbide content here cannot be attributed to insufficient Cr and C. Since the top region of the cladding layer was directly heated by the arc and solidified last, its cooling rate was significantly slower compared to the middle and bottom regions. The slower cooling facilitated the diffusion of Cr and C elements toward grain boundaries, reducing their solid solubility within the grains. As a result, carbide precipitation within the grains was notably diminished.

However, the microstructural distribution underwent significant variations under higher dilution ratios. At this high-dilution condition, the grain boundary phase retained the highest Cr content (>30 wt.%). Significant intragranular Cr23C6 carbide precipitation was observed near the top of the cladding layer (Fig. 5.7(f)), showing a clear distinction with the low-dilution case. For the high-dilution sample, the heat input was higher and the peak temperature of the molten pool was expected to rise, thereby enhancing the solid solubility of Cr and C elements within the melt. Although elevated temperatures generally promoted the diffusion of Cr and C, the prolonged high-temperature duration simultaneously facilitated grain growth. This extended thermal exposure effectively increased the diffusion distance of Cr and C to grain boundaries, ultimately leading to a higher incidence of intragranular Cr23C6 carbide precipitation and a more uniform distribution of the carbides. The observation aligns with the previous XRD results, indicating an increase in the diffracted intensity of Cr23C6. Fig. 5.7(g) and (h) present EDS line scan results across the NM450/cladding layer interface at low and high dilution ratios, respectively. The more gradual elemental distribution profile of the high-dilution sample confirmed more uniform element mixing under this condition.

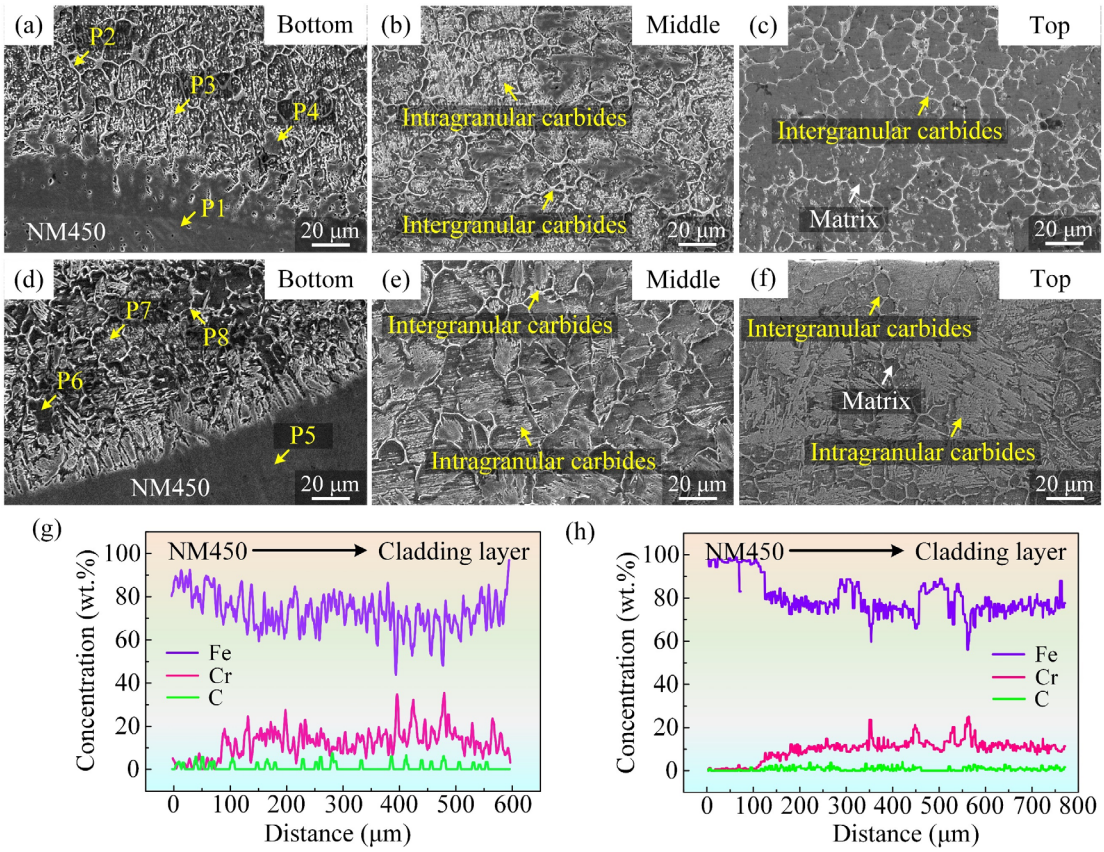


Fig. 5.7. Microstructures at the NM450/cladding layer interface: (a-c) in the bottom, middle, and top regions at low dilution ratios; (d-f) in the bottom, middle, and top regions at high dilution ratios; (g, h) EDS line scan results at low and high dilution ratios, respectively.

Table 5.3. EDS point analysis results at the NM450/cladding layer interface (wt.%).

	Fe	Cr	Nb	Si	Mn	C
P1	88.4	5.1	2.6	1.0	1.7	1.2
P2	64.4	29.6	0.3	1.2	1.7	2.8
P3	77.9	15.3	0.8	2.2	1.6	2.2
P4	83.4	10.5	0.7	1.5	2.6	1.3
P5	92.6	2.7	0.7	0.5	2.5	1.0
P6	93.4	6.5	-	-	-	0.1
P7	80.1	14.5	0.5	2.1	1.3	1.5
P8	60.6	32.5	0.3	1.6	2.3	2.7

5.3.2 Microstructure characteristics at the ER70-G/cladding layer interface

Fig. 5.8 presents the microstructural morphology at the interface between the ER70-G and the cladding layer, exhibiting distinct characteristics compared to the NM450

region. Although the phase distribution remained largely unchanged, with the white precipitates demonstrating higher Cr content than the gray phase (EDS results listed in Table 5.4), the quantity of carbides was visibly lower than that of the NM450 region. This phenomenon was particularly pronounced in the middle and top zones of the cladding layer, where intragranular carbides were notably scarce, as illustrated in Fig. 5.8(b) and (c). This discrepancy can be attributed to the base metal's inherent alloy composition. The NM450 base material naturally contains higher levels of Cr and C, which facilitate carbide formation. In contrast, the ER70-G possesses fewer alloying elements. Upon mixing with the cladding filler wire, the Cr and C concentrations were significantly diluted, thereby reducing carbide precipitation. However, when the dilution ratio was increased, the elevated peak temperature and prolonged high-temperature duration substantially enhanced the solid solubility of Cr and C. Concurrently, grain growth (longer diffusion distance for Cr and C) impeded effective grain boundary segregation, promoting extensive intragranular carbide precipitation and diminishing the characteristic carbide network along grain boundaries (Fig. 5.8(c-e)). This phenomenon contributed to more uniform carbide distribution, as further corroborated by EDS line-scan analysis (Fig. 5.8(g) and (h)), which revealed smoother elemental distribution profiles with reduced fluctuations under high-dilution condition.

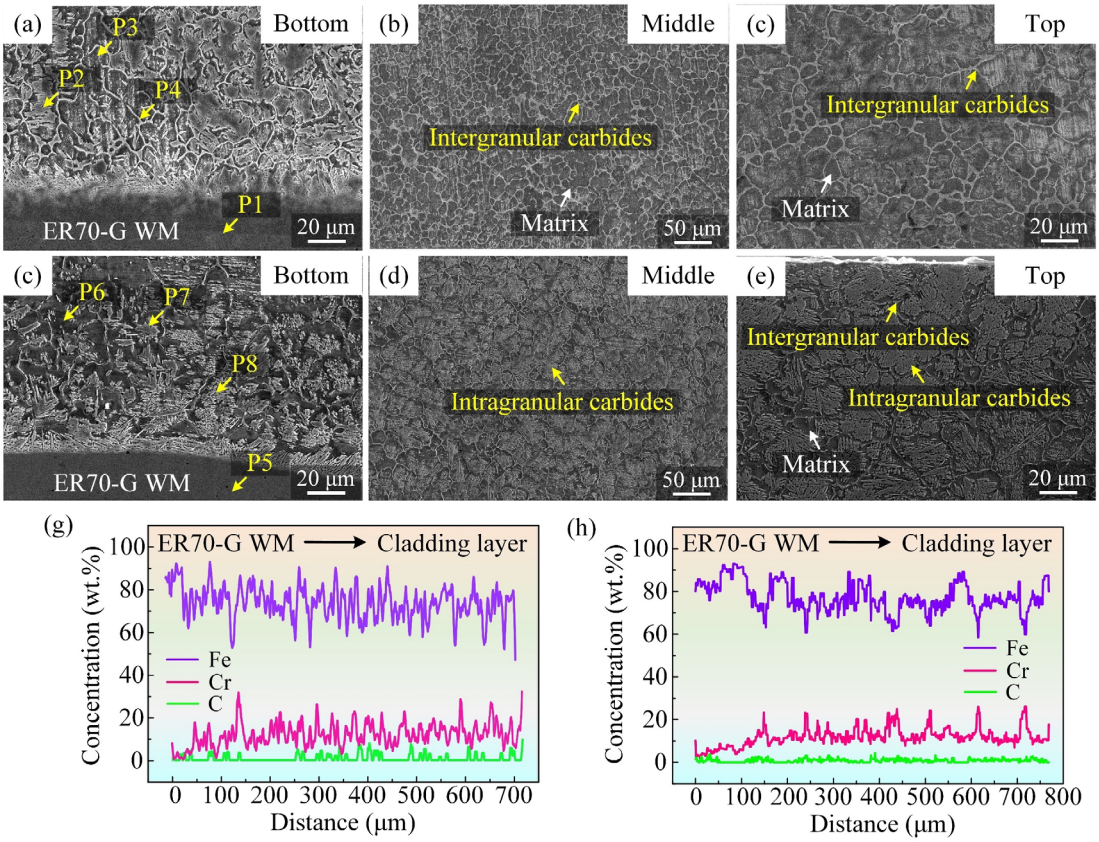


Fig. 5.8. Microstructures at the ER70-G/cladding layer interface: (a-c) in the bottom, middle, and top regions at low dilution ratios; (d-f) in the bottom, middle, and top regions at high dilution ratios; (g, h) EDS line scan results at low and high dilution ratios, respectively.

Table 5.4. EDS point analysis results at the ER70-G/cladding layer interface (wt.%).

	Fe	Cr	Nb	Si	Mn	C
P1	89.5	4.3	0.4	0.9	3.0	1.9
P2	80.9	13.9	0.5	1.3	1.5	1.9
P3	82.3	11.6	0.2	1.1	2.0	2.8
P4	66.3	26.1	0.3	1.7	3.1	2.5
P5	94.2	1.0	0.1	0.5	2.4	1.8
P6	82.1	12.9	0.3	1.6	1.3	1.8
P7	55.9	38.1	0.5	1.4	1.6	2.5
P8	80.8	14.0	-	1.9	1.7	1.6

5.3.3 Microstructure characteristics at the ZG30SiMn/cladding layer interface

Fig. 5.9 presents the interfacial microstructure between ZG30SiMn and the cladding layer, with the corresponding EDS results listed in Table 5.5. Although the Cr content

in the ZG30SiMn base material is lower than that in NM450, it is slightly higher than that in ER70-G. Additionally, its carbon content is marginally elevated. Consequently, while the number of intragranular carbides in the ZG30SiMn region was relatively low, a significant amount of dark gray (Fe, Cr) solid solution was observed, as shown in Fig. 5.9(a-c). Under high-dilution condition, the higher heat input promoted the formation of intragranular carbides, exhibiting a trend consistent with the microstructural distribution observed at the NM450 and ER70-G regions. This suggests that high-dilution sample possessed increased carbide nucleation and precipitation, and improved spatial uniformity, as evidenced by the line-scan results in Fig. 5.9(g) and (h).

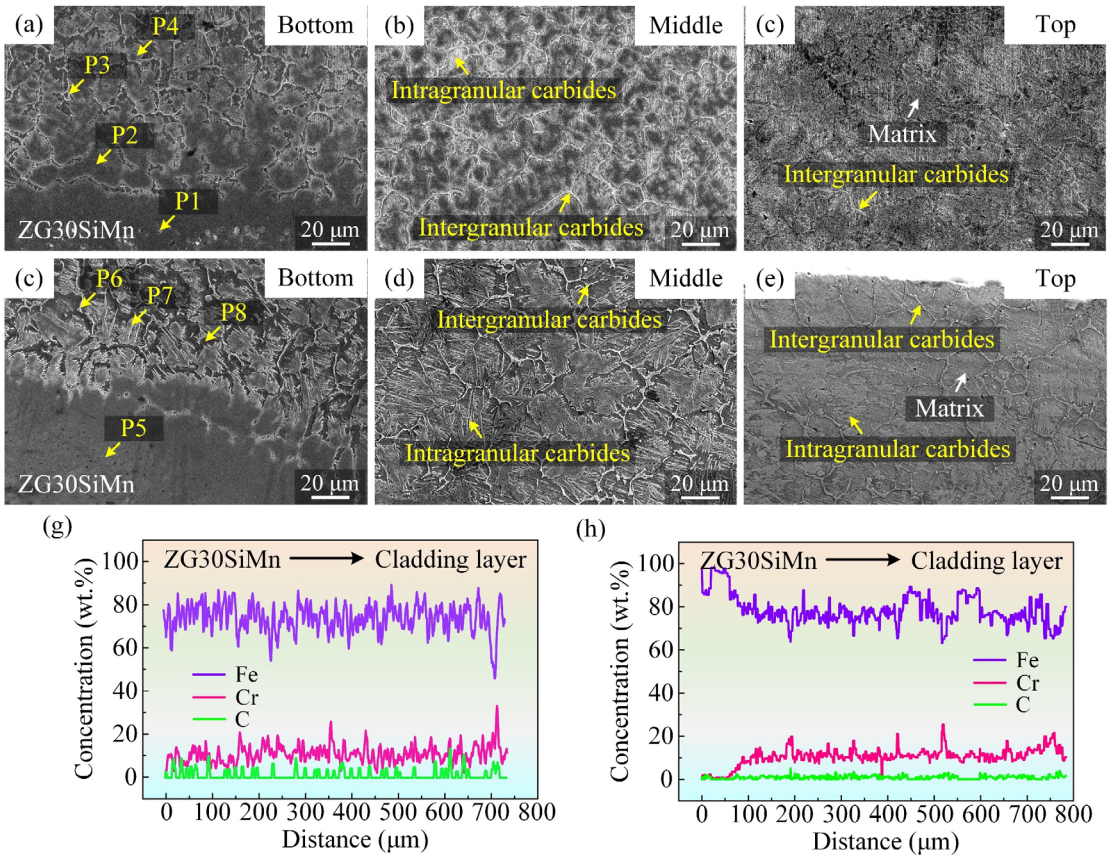


Fig. 5.9. Microstructures at the ZG30SiMn/cladding layer interface: (a-c) in the bottom, middle, and top regions at low dilution ratios; (d-f) in the bottom, middle, and top regions at high dilution ratios; (g, h) EDS line scan results at low and high dilution ratios, respectively.

Table 5. EDS point analysis results at the ZG30SiMn/cladding layer interface (wt.%).

	Fe	Cr	Nb	Si	Mn	C
P1	87.6	8.2	0.2	1.0	1.7	1.3

P2	82.7	11.6	0.1	1.1	2.7	1.8
P3	62.5	30.1	0.7	1.4	2.3	3.3
P4	83.4	12.9	0.2	1.3	1.4	0.8
P5	92.2	3.5	0.2	1.0	1.6	1.5
P6	58.3	34.9	0.4	1.3	1.8	3.3
P7	82.5	12.7	0.1	2.2	0.7	1.8
P8	81.1	11.8	0.4	2.0	2.3	2.4

5.3.4 Microstructure characteristics of the ternary mixing zones

In addition to the microstructures at the binary interfaces, particular attention should be paid to the microstructural characteristics of the ternary mixing zones in both NM450/ER70-G/cladding and ER70-G/ZG30SiMn/cladding systems, as shown in Figs 5.10 and 5.11, respectively. Under the high-dilution condition, a distinct transition in carbide distribution was observed: the continuity of grain boundary carbides was disrupted, while numerous intragranular carbides formed instead, leading to an increased areal fraction of carbide distribution. Notably, in the ER70-G/ZG30SiMn/cladding mixing zone at the low-dilution condition, a carbide-depleted region was clearly visible within the grains (Fig. 5.11(a)), indicating poor uniformity of carbide distribution. However, for the high-dilution sample, this carbide-depleted zone disappeared completely, accompanied by a remarkable improvement in the uniformity of carbide distribution.

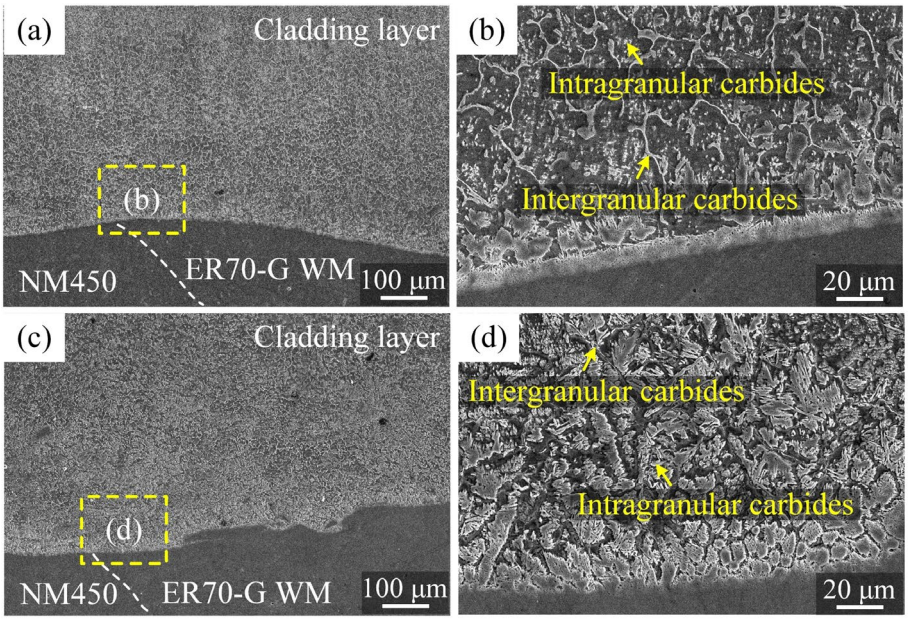


Fig. 5.10. Microstructures at the compositional mixing zone of NM450/ER70-G/cladding layer: (a, b) at low dilution ratios; (c, d) at high dilution ratios.

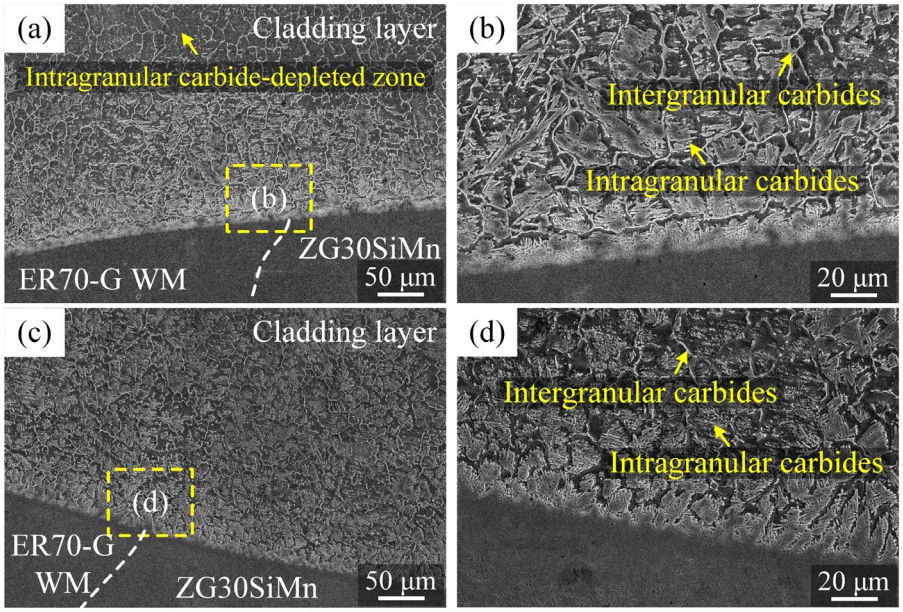


Fig. 5.11. Microstructures at the compositional mixing zone of ER70-G/ZG30SiMn/cladding layer: (a, b) at low dilution ratios; (c, d) at high dilution ratios.

5.4. Wear performance improvement for the welded joint

5.4.1 Microhardness distribution of the cladding layer

Microhardness measurements were conducted on the cladding layers, with the distribution profiles presented in Fig. 5.12. Fig. 5.12(a) displays the hardness distribution in the NM450 region under varying dilution ratios. The NM450 base material itself exhibited high hardness values ranging between 400-450 $HV_{0.2}$. The hardness of the cladding layer slightly exceeded that of the NM450 base material, measuring 450-500 $HV_{0.2}$. Notably, when the dilution ratio was increased, the cladding hardness rises significantly, reaching a maximum value of approximately 550 $HV_{0.2}$. Fig. 5.12(b) and (c) illustrate the hardness profiles for the ER70-G and ZG30SiMn regions, respectively. The base materials of ER70-G and ZG30SiMn showed markedly lower hardness (~300 $HV_{0.2}$) compared to NM450. However, the higher dilution ratio promoted the diffusion of alloying elements from the cladding into the base materials, resulting in elevated hardness near the interfacial region relative to the low-dilution condition. Generally, the cladding layers produced at high dilution ratio demonstrated

superior hardness, which was attributed to enhanced carbide formation under higher heat input conditions.

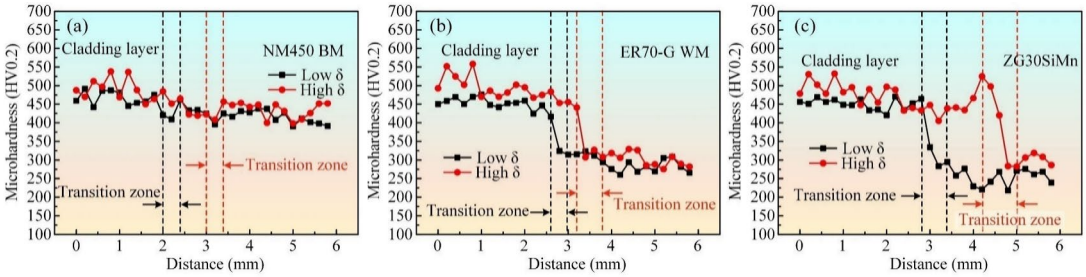


Fig. 5.12. Microhardness distribution: (a) in the NM450 region; (b) in the ER70-G region; (c) in the ZG30SiMn region.

5.4.2 Wear performance evaluation for the welded joint

The worn surface morphologies are presented in Fig. 5.13, along with measurements of the wear scar widths. For comparative analysis, the wear properties of the NM450, ER70-G, and ZG30SiMn base materials were also evaluated, as shown in Fig. 5.13(a-c). The wear scar width on the NM450 surface (806.2 μm) was narrower than that of ER70-G (828.9 μm) and ZG30SiMn (831.4 μm), proving the superior wear resistance of the NM450 plate. All three base materials exhibited prominent sliding grooves and adhesion features, indicating a mixed wear mechanism involving both sliding wear and adhesive wear. After cladding with KB968 welding wire, the characteristic sliding grooves disappeared, and adhesive wear played a dominant role. For the NM450 and ER70-G regions, the wear scar widths at high dilution ratio (565.5 μm and 607.8 μm, respectively) were slightly larger than those at low dilution ratio (551.5 μm and 597.5 μm). However, the low-dilution samples exhibited more severe adhesive wear behavior, characterized by large-scale surface spalling. In contrast, the ZG30SiMn region showed a significantly narrower wear scar at high-dilution condition (444.2 μm) compared to the low-dilution sample (599.1 μm), as illustrated in Fig. 5.13(c_1, c_2).

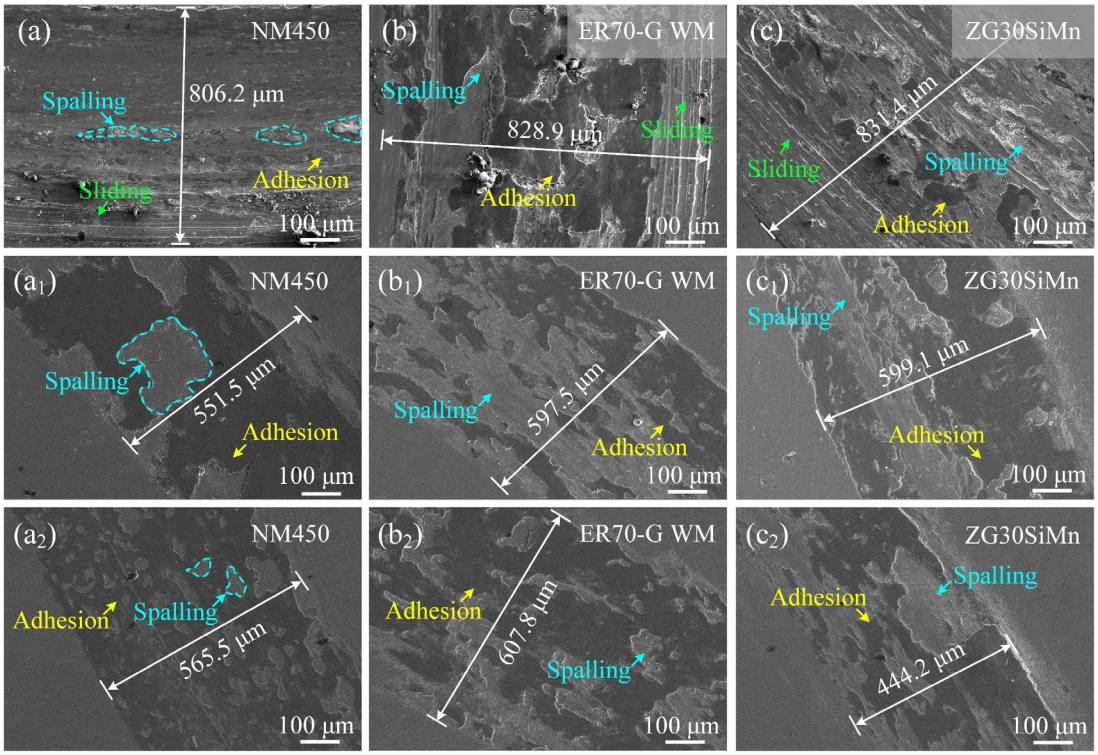


Fig. 5.13. Worn surface morphologies of base materials and their cladding layers under different dilution ratios: (a-c) NM450, ER70-G substrate, and ZG30SiMn base materials; (a_1-a_2) cladding layer in the NM450 region under low and high dilution ratios; (b_1-b_2) cladding layer in the ER70-G region under low and high dilution ratios; (c_1-c_2) cladding layer in the ZG30SiMn region under low and high dilution ratios.

The friction coefficient was further measured, as shown in Fig. 5.14. The friction coefficients of the NM450 and ER70-G regions were close under different dilution ratios, but slightly lower at high-dilution condition. The ZG30SiMn region, however, demonstrated a significantly lower friction coefficient at high-dilution condition. Notably, all cladding layers exhibited a markedly lower friction coefficient than the base materials. The friction coefficient reflects the resistance encountered during sliding contact under load. A higher friction coefficient means larger resistance and increases surface spalling and damage, whereas a lower value indicates improved wear resistance[141, 143]. This verified that the employment of KB968 welding wire improved the overall wear properties of the NM450/ER70-G/ZG30SiMn welded joints, with higher dilution ratio showed better wear resistance. To further precisely assess wear resistance, weight loss was measured and the results are presented in Fig. 5.15.

The results indicated that the NM450, ER70-G, and ZG30SiMn base materials exhibited severe weight loss, with values of 0.3549 g, 0.3916 g, and 0.4057 g, respectively. After cladding treatment, the weight loss was substantially reduced. Moreover, the results confirmed that across all material interfaces (NM450, ER70-G, and ZG30SiMn), samples of high dilution ratio exhibited less weight loss than those processed at low-dilution condition. Combined analysis of worn surface morphology, coefficient of friction, and weight loss demonstrates that the high-dilution sample yields superior tribological performance compared to the low-dilution one.

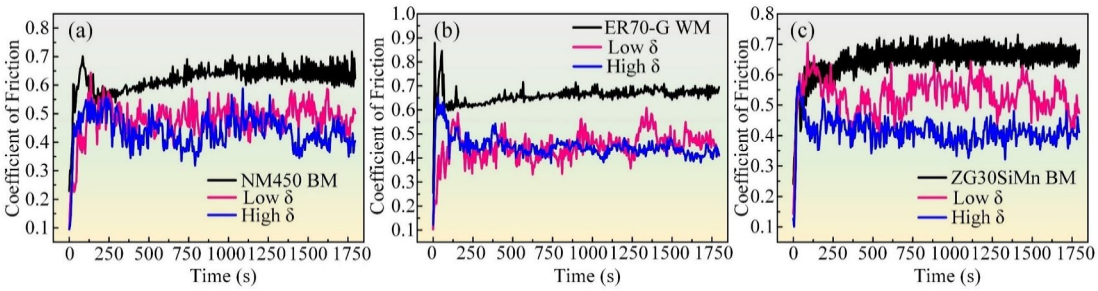


Fig. 5.14. Coefficient of friction: (a) in the NM450 region; (b) in the ER70-G region; (c) in the ZG30SiMn region.

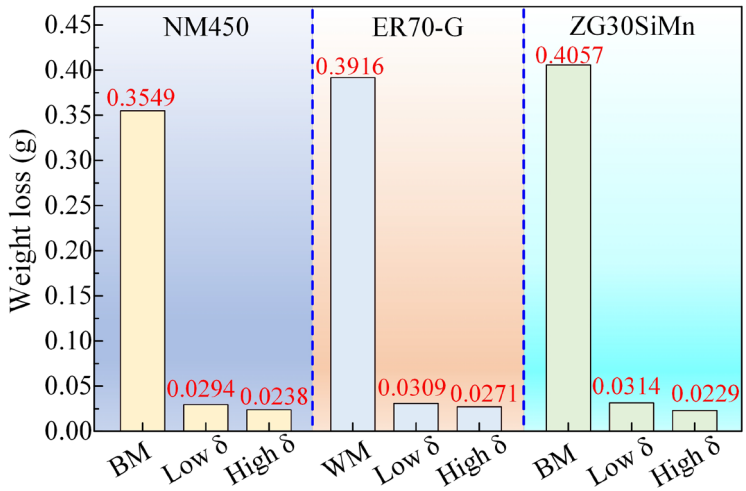


Fig. 5.15. Wear weight loss comparison under different dilution ratios.

The wear performance of materials is closely related to the quantity, size, and distribution of wear-resistant phases. Conventionally, a lower dilution ratio is believed to help preserve alloying elements (such as Cr and C) in the cladding layer, thereby promoting the formation of hard wear-resistant phases and reducing friction-induced

damage[81, 139, 144]. However, in this study, the high-dilution samples demonstrated superior wear resistance. This can be attributed to the fact that a moderate increase in current (and thus heat input) prolongs the metallurgical reaction time at elevated temperatures and enhances elemental diffusion. These effects not only increase the precipitation of carbides but also improve their distribution uniformity, ultimately leading to enhanced wear resistance. In addition, the high-efficiency arc wire cladding technology yields a thicker cladding layer compared to the powder cladding method. Although significant dilution or elemental mixing occurs at the interface regions, the top zones of thick cladding layer are less affected by the degree of dilution.

5.5. Summary

This study employed Fe-Cr-C welding wire to fabricate cladding layers on NM450/ER70-G/ZG30SiMn dissimilar steel welded joints, and investigated the microstructure distribution and wear resistance under different dilution ratios. Key findings are summarized as follows:

(1) The cladding layers exhibited a crack-free morphology across all three heterogeneous interfaces (NM450/cladding, ER70-G/cladding, and ZG30SiMn/cladding). Additionally, higher heat input led to an increased dilution ratio between the cladding layer and base material.

(2) Cr7C3 carbides were observed to precipitated along gain boundaries, whereas Cr23C6 carbides tended to form within grains. Compared to the low-dilution condition, the high-dilution sample exhibited enhanced precipitation of Cr23C6 carbides with a more homogeneous distribution.

(3) The NM450/ER70-G/ZG30SiMn heterogeneous welded joints showed improved wear performance after cladding treatment, with the high-dilution sample presenting superior wear resistance. Despite severe elemental mixing at the interface, the top region of the cladding layer was minimally affected by dilution-related adverse effects.

Chapter 6. Summary and prospect

This dissertation focuses on the key technical challenges in the manufacturing and performance enhancement of thick-walled dissimilar steel structures (represented by scraper conveyor chute structures). The author systematically conducted research on double-wire narrow GMAW process optimization, microstructure and mechanical property regulation of high-strength low-alloy (HSLA) steel deposited metal, comprehensive evaluation of dissimilar steel welded joints, and wear resistance improvement of welded joints via Fe-Cr-C alloy cladding. The main research findings and contributions are summarized as follows:

In Chapter 2:

I. Clarified the relationship between process parameters (wire feeding speed, welding speed, double-wire spacing) and arc stability/droplet transfer: stable spray transition is achieved at 8 m/min wire feeding speed; a 6 mm lateral spacing and 8–11 mm/s welding speed avoid defects like lack of fusion and undercut.

II. Optimized groove design (triangular bottom) and process matching, realizing defect-free welding of 30-mm-thick plates.

In Chapter 3:

I. Proposed an interlayer dwell time (IDT) control strategy: prolonging IDT from 2 min to 22 min mitigates thermal accumulation, stabilizes interlayer temperature, and refines microstructure (grain size reduced from 9.96 μm to 5.13 μm).

II. Achieved synergistic improvement of strength and toughness: ultimate tensile strength increased by 16.3%, impact toughness by 27.3%, with fracture mode transitioning to fully ductile.

In Chapter 4:

I. Revealed microstructure characteristics: weld metal (WM) consists of acicular ferrite and polygonal ferrite; heat-affected zone (HAZ) is divided into four sub-zones with distinct microstructures (martensite, fine martensite, etc.).

II. Confirmed reliable mechanical properties: joint ultimate tensile strength reaches ~708 MPa, HAZ impact toughness is 86%–110% of base metals, and bending tests

show no interfacial cracking.

In Chapter 5:

I. Realized crack-free cladding: KB968 wire forms a cladding layer with Fe matrix and carbides (Cr_7C_3, $Cr_{23}C_6$), microhardness increased to 450–550 $HV_{0.2}$.

II. Significantly improved wear performance: wear weight loss reduced by over 90%, friction coefficient decreased from 0.6–0.7 to 0.3–0.5.

Based on the research results of this dissertation, the following directions are proposed for future in-depth study and industrial application expansion:

(1) Expansion of welding process and material system

Extend the double-wire narrow gap GMAW technology to more dissimilar material combinations (such as NM500/ZG40CrMnSiMoVA, stainless steel/HSLA steel) and explore the influence of process parameters on joint formation and performance under different thicknesses (≥60 mm) and welding positions (vertical, overhead).

Develop gradient cladding technology based on Fe-Cr-C alloys, adjust the Cr/C ratio or add trace alloying elements (Nb, V, Ti) to tailor the type and distribution of carbides, and further improve the wear resistance and impact toughness of the cladding layer.

(2) Deepening of microstructure regulation mechanism

Conduct in-situ observation of phase transformation and carbide precipitation during the welding and cladding processes using advanced characterization techniques (in-situ high-temperature EBSD, transmission electron microscopy (TEM)), and establish a more precise process-microstructure-property relationship model.

Study the effect of thermal cycle accumulation on the evolution of residual stress in thick-walled dissimilar joints, and explore the coupling mechanism of residual stress and microstructure on joint fatigue performance.

(3) Evaluation of long-term service performance

Carry out accelerated aging tests, corrosion-wear synergy tests, and fatigue tests under actual working conditions (coal mine wet environment, impact load), and evaluate the long-term service reliability and failure mechanism of welded joints and cladding layers.

Investigate the influence of post-weld heat treatment (PWHT) on residual stress relief, microstructure homogenization, and performance optimization of dissimilar joints, and provide technical support for engineering application.

References

[1] Zhang J, Cheng D, Wang J, Yang S, Wan X, Li X. Improving recovery in sublevel top coal caving mining by using partially reverse drawing technique. Int J Min Sci Technol 2024;34: 1655-1676, https://doi.org/10.1016/j.ijmst.2024.11.010.

[2] Shi Z, Zhu Z. Case study : wear analysis of the middle plate of a heavy-load scraper conveyor chute under a range of operating conditions. Wear 2017;380-381: 36-41, https://doi.org/10.1016/j.wear.2017.03.005.

[3] Wang A, Cheng X, Meng G, Wo L, Pang Z. Experimental study on the welding procedure of the central groove of armored face conveyor. Adv Mech Eng 2016;8: 12, https://doi.org/10.1177/1687814016674101.

[4] Ozturan AB, Irsel G, Guezey BN. Study of the microstructure and mechanical property relationships of gas metal arc welded dissimilar hardox 450 and s355j2c+n steel joints. Mater Sci Eng a Struct Mater 2022;856: 21, https://doi.org/10.1016/j.msea.2022.143486.

[5] Sharma V, Shahi AS. Effect of groove design on mechanical and metallurgical properties of quenched and tempered low alloy abrasion resistant steel welded joints. Mater Des 2014;53: 727-736, https://doi.org/10.1016/j.matdes.2013.07.043.

[6] Han Y, Chu J, Wang Q, Fu K, Jin H, Wei Y. Investigation of microstructure , mechanical properties , residual stress , and distortion in multi-pass gas metal arc welding of ZGMn13mo / a514 dissimilar joints. Mater Chem Phys 2025;341: 26, https://doi.org/10.1016/j.matchemphys.2025.130941.

[7] Lei Z, Cao H, Cui X, Ma Y, Li L, Zhang Q. A novel high efficiency narrow-gap laser welding technology of 120 mm high-strength steel. Opt Lasers Eng 2024;178: 17, https://doi.org/10.1016/j.optlaseng.2024.108232.

[8] Ni Z, Dong B, Li Y, Cai X, Lin S. Effects of processing parameters on molten behavior , arc stability , and defect forming in swing - arc narrow gap GMA vertical up welding. J Mater Process Technol 2023;321: 14, https://doi.org/10.1016/j.jmatprotec.2023.118155.

[9] Zhu C, Cheon J, Tang X, Na S, Lu F, Cui H. Effect of swing arc on molten pool behaviors in narrow-gap GMAW of 5083 al-alloy. J Mater Process Technol 2018;259: 243-258, https://doi.org/10.1016/j.jmatprotec.2018.04.026.

[10] Sun Q, Liu Y, Zhang Q, Kang K, Liu C, Liu Y et al. A new method for refinement of ti-6al-4 v prior-β grain structure in the alternating magnetic field assisted narrow gap gas tungsten arc welding (AMF-GTAW) via filler wire oscillation. J Mater Process Technol 2024;327: 15, https://doi.org/10.1016/j.jmatprotec.2024.118376.

[11] Zhou J, Liu X, Li X, Huo X, Zhao B, Ding K et al. Microstructure details and impact toughness for dissimilar 9cr / CrMoV welded joints fabricated by NG-SAW and NG-TIG techniques. J Mater Res Technol-JMRT 2024;29: 2936-2946, https://doi.org/10.1016/j.jmrt.2024.02.048.

[12] Li J, Wang J, Liu Z, Lyu X, Liu X, Li Z et al. Interplay of microstructure and mechanical

properties in vacuum laser beam welded 50-mm-thick titanium alloy plates: insights from molten pool flow simulation. Opt Laser Technol 2026;193: 114187, https://doi.org/10.1016/j.optlastec.2025.114187.

[13] Fan Y, Cao J, Zhang J, Zhao Y, Fang R, Wang Y et al. Stable production of dissimilar steel joints in construction machinery by narrow gap oscillating laser welding. J Mater Res Technol-JMRT 2024;30: 1403-1413, https://doi.org/10.1016/j.jmrt.2024.03.126.

[14] Li FS, Wu LH, Li HJ, Hua PT, Ni DR, Xue P et al. Simultaneously enhanced strength and impact toughness in electron beam welded joints of near β titanium alloy thick plates via good coupling of multi-level lamellar microstructures. J Mater Sci Technol 2025;232: 28-42, https://doi.org/10.1016/j.jmst.2025.02.010.

[15] Zhao J, Chen G, Teng X, Yang C, Gan Z, Zhu L et al. Study on microstructure and properties of zr-4 / TC4 dissimilar metal electron beam welding. Mater Lett 2026;403: 4, https://doi.org/10.1016/j.matlet.2025.139505.

[16] Zhang C, Li G, Gao M, Zeng X. Microstructure and mechanical properties of narrow gap laser-arc hybrid welded 40 mm thick mild steel. Materials (Basel) 2017;10: 10, https://doi.org/10.3390/ma10020106.

[17] Long J, Zhang L, Zhuang M, Bai L, Na S. Narrow-gap laser welding with beam wobbling and filler wire and microstructural performance of joints of thick TC4 titanium alloy plates. Opt Laser Technol 2022;152: 20, https://doi.org/10.1016/j.optlastec.2022.108089.

[18] Li J, Liu Y, Kang K, Sun Q, Jin P, Liu Y et al. A novel approach to regulate energy allocation and melt flow in narrow gap laser welding with electromagnetic assisted wire wobbling. J Mater Process Technol 2021;289: 12, https://doi.org/10.1016/j.jmatprotec.2020.116909.

[19] Wang J, Liu Z, Xu Z, Duan Y, Liu X, Zhan X. Enhanced microstructure and mechanical properties in narrow gap ring-core adjustable laser welding of titanium alloys: insights from molten pool morphology. J Mater Process Technol 2025;342: 20, https://doi.org/10.1016/j.jmatprotec.2025.118934.

[20] Wei B, Jia C, Wu W, Fang C, Wu C. Stirring effect of the rotating arc on the molten pool during non- axisymmetric tungsten NG-GTAW. J Mater Process Technol 2020;285: 7, https://doi.org/10.1016/j.jmatprotec.2020.116769.

[21] Yang Z, Chen Y, Zhang Z, Fang C, Xu K, He P et al. Research on the sidewall penetration mechanisms of cable-type welding wire narrow gap GMAW process. Int J Adv Manuf Technol 2022;120: 2443-2455, https://doi.org/10.1007/s00170-022-08866-1.

[22] Li F, Sun Q, Jin P, Liu Y, Chen M, Li J et al. Wetting behavior of melt and its effect on lack of fusion in arc oscillating NG-GTAW. J Mater Process Technol 2021;296: 10, https://doi.org/10.1016/j.jmatprotec.2021.117176.

[23] Li F, Liu Y, Kong H, Ren H, Tao Y, Zhang Q et al. Insight on microstructure and mechanical properties of 40 mm thick-walled ferromagnetic super-MSS by magnetic-field-assisted narrow gap GTAW. J Mater Res Technol-JMRT 2023;24: 5805-5822, https://doi.org/10.1016/j.jmrt.2023.04.117.

[24] Yu J, Cai C, Xie J, Huang J, Liu Y, Chen H. Weld formation, arc behavior, and droplet transfer in narrow-gap laser-arc hybrid welding of titanium alloy. J Manuf Process 2023;91: 44-52, https://doi.org/10.1016/j.jmapro.2023.02.022.

[25] Yang X, Chen H, Li MV, Bu H, Zhu Z, Cai C. Porosity suppressing and grain refining of narrow-gap rotating laser-MIG hybrid welding of 5a06 aluminum alloy. J Manuf Process 2021;68: 1100-1113, https://doi.org/10.1016/j.jmapro.2021.06.036.

[26] Wang J, Zhu J, Fu P, Su R, Han W, Yang F. A swing arc system for narrow gap GMA welding. ISIJ Int 2012;52: 110-114, https://doi.org/DOI 10.2355/isijinternational.52.110.

[27] Xu G, Wang J, Li P, Zhu J, Cao Q. Numerical analysis of heat transfer and fluid flow in swing arc narrow gap GMA welding. J Mater Process Technol 2018;252: 260-269, https://doi.org/10.1016/j.jmatprotec.2017.09.030.

[28] Xu WH, Lin SB, Fan CL, Zhuo XQ, Yang CL. Statistical modelling of weld bead geometry in oscillating arc narrow gap all-position GMA welding. Int J Adv Manuf Technol 2014;72: 1705-1716, https://doi.org/10.1007/s00170-014-5799-2.

[29] Bao Y, Xue R, Zhou J, Xu Y. Effect of increasing oscillation width on the arc characteristics and droplet transfer behavior of x80 steel in the overhead welding position of narrow gap p-GMAW. Metals (Basel) 2023;13: 15, https://doi.org/10.3390/met13071314.

[30] Su N, Wang J, Xu G, Zhu J, Jiang Y. Infrared visual sensing detection of groove width for swing arc narrow gap welding. Sensors (Basel) 2022;22: 21, https://doi.org/10.3390/s22072555.

[31] Chen Q, Xie Z, Wang J, Lin S, Dou Q, Huang T. A comparison of the swing and non-swing arc behavior in arc ultrasonic assisted narrow gap GMAW. J Mater Res Technol-JMRT 2023;24: 4698-4710, https://doi.org/10.1016/j.jmrt.2023.04.095.

[32] Sankar N, Malarvizhi S, Balasubramanian V. Effect of rotating arc on mechanical properties and microstructural characteristics of gas metal arc welded carbon steel joints. Metallogr Microstruct Anal 2021;10: 541-559, https://doi.org/10.1007/s13632-021-00769-z.

[33] Guo N, Wang M, Guo W, Yu J, Feng J. Study on forming mechanism of appearance defects in rotating arc narrow gap horizontal GMAW. Int J Adv Manuf Technol 2014;75: 15-20, https://doi.org/10.1007/s00170-014-6127-6.

[34] Costa JFM, Filho WAS, Jorge JCF, Mendes MC, de Souza LFG, Chuvas TC et al. Investigation on the ASTM a516 grade 70 narrow gap welded joints obtained by the GMAW process with rotating electrode. Int J Adv Manuf Technol 2024;134: 3453-3464, https://doi.org/10.1007/s00170-024-14358-1.

[35] Silveira GMS, Filho WAS, Costa JFM, Mendes MC, Souza LFG, Jorge JCF. Influence of rotation frequency and rotation diameter on mechanical properties and microstructure of weld metal produced by MCAW-RE. Int J Adv Manuf Technol 2020;110: 1789-1803,

https://doi.org/10.1007/s00170-020-05961-z.
[36] Li W, Yu R, Huang D, Wu J, Wang Y, Hu T et al. Numerical simulation of multi-layer rotating arc narrow gap MAG welding for medium steel plate. J Manuf Process 2019;45: 460-471,
https://doi.org/10.1016/j.jmapro.2019.07.035.
[37] Han S, Tang X, Liu G, Xu L, Cui H, Shao C. Effects of arc interaction on lack-of-fusion and porosity in tandem NG-GMAW of 5083 al-mg alloy. J Manuf Process 2022;81: 92-106,
https://doi.org/10.1016/j.jmapro.2022.06.059.
[38] Liu G, Tang X, Han S, Lu F, Cui H. Influence of interwire angle on undercutting formation and arc behavior in pulsed tandem narrow-gap GMAW. Mater Des 2020;193: 14,
https://doi.org/10.1016/j.matdes.2020.108795.
[39] Kang S, Kang M, Jang YH, Kim C. Droplet transfer and spatter generation in DC-AC pulse tandem gas metal arc welding. Sci Technol Weld Join 2020;25: 589-599,
https://doi.org/10.1080/13621718.2020.1786262.
[40] Cai XY, Fan CL, Lin SB, Yang CL, Bai JY. Molten pool behaviors and weld forming characteristics of all-position tandem narrow gap GMAW. Int J Adv Manuf Technol 2016;87: 2437-2444,
https://doi.org/10.1007/s00170-016-8644-y.
[41] Cai X, Fan C, Lin S, Yang C, Hu L, Ji X. Effects of shielding gas composition on arc behaviors and weld formation in narrow gap tandem GMAW. Int J Adv Manuf Technol 2017;91: 3449-3456,
https://doi.org/10.1007/s00170-017-9990-0.
[42] Han S, Liu G, Tang X, Xu L, Cui H, Shao C. Effect of molten pool behaviors on welding defects in tandem NG-GMAW based on CFD simulation. Int J Heat Mass Transf 2022;195: 15,
https://doi.org/10.1016/j.ijheatmasstransfer.2022.123165.
[43] Assuncao PDC, Ribeiro RA, Santos EBFD, Gerlich AP, de Magalhaes Braga E. Feasibility of narrow gap welding using the cold-wire gas metal arc welding (CW-GMAW) process. Weld World 2017;61: 659-666,
https://doi.org/10.1007/s40194-017-0466-5.
[44] Wang J, Jiang Y, Zhu J, Liu D, Xu G, Li W. Development of swing arc narrow gap GMAW process assisted by swaying wire. J Mater Process Technol 2023;318: 11,
https://doi.org/10.1016/j.jmatprotec.2023.118004.
[45] Zhu Z, Wang J, Liu S, Jiang Y, Zhu J, Li X et al. Thick-wire swing arc narrow gap GMA welding assisted by pre-embedding cold wires. Int J Adv Manuf Technol 2024;131: 301-313,
https://doi.org/10.1007/s00170-024-13093-x.
[46] Wang Z, Zhang W, Li M, Wu Z, Liang J, Zhang L. Comparison of high-strength low-alloy steels fabricated by wire arc additive manufacturing and conventional casting: effect of quenching and tempering on microstructural evolution and mechanical properties. J Alloys Compd 2025;1032: 14,
https://doi.org/10.1016/j.jallcom.2025.181022.
[47] Wang C, Li C, Dai L, Yang X, Han J, Cui S et al. Simultaneously enhancing strength and

fracture toughness via tailoring the microstructure in x80 girth weld metal. J Mater Res Technol-JMRT 2024;29: 3096-3107, https://doi.org/10.1016/j.jmrt.2024.01.283.

[48] Shao Y, Liu C, Yan Z, Li H, Liu Y. Formation mechanism and control methods of acicular ferrite in HSLA steels: a review. J Mater Sci Technol 2018;34: 737-744, https://doi.org/10.1016/j.jmst.2017.11.020.

[49] Zhang W, Shang X, Chen S, Zhang L. Comparison of microstructural characteristics and mechanical properties of the high-strength low-alloy steels fabricated by wire arc additive manufacturing versus conventional casting. Mater Sci Eng a Struct Mater 2023;885: 15, https://doi.org/10.1016/j.msea.2023.145593.

[50] Chen M, Zhang T, Gong Z, Zuo W, Wang Z, Zong L et al. Mechanical properties and microstructure characteristics of wire arc additively manufactured high-strength steels. Eng Struct 2024;300: 16, https://doi.org/10.1016/j.engstruct.2023.117092.

[51] Wen J, Li L, Sheng X, Song F, Han B, Li X. Microstructure and mechanical properties of TIG and TIG+ FCAW automatic welded joints of x70 pipeline steel at 45° slope. Int J Pressure Vessels Pip 2025;214: 105450, https://doi.org/10.1016/j.ijpvp.2025.105450.

[52] Feng Y, Xu X, Wang X, Wang L, Zou J, Wang Z. Effect of heat treatment on microstructure and mechanical properties of AG728 steel joints welded with ER90s-g wires. Phys Scr 2024;99: 13, https://doi.org/10.1088/1402-4896/ad5652.

[53] Rodrigues TA, Duarte VR, Tomas D, Avila JA, Escobar JD, Rossinyol E et al. In - situ strengthening of a high strength low alloy steel during wire and arc additive manufacturing (WAAM). Addit Manuf 2020;34: 10, https://doi.org/10.1016/j.addma.2020.101200.

[54] Zou X, Sun J, Matsuura H, Wang C. Unravelling microstructure evolution and grain boundary misorientation in coarse-grained heat-affected zone of EH420 shipbuilding steel subject to varied welding heat inputs. Metall Mater Trans a Phys Metall Mater Sci 2020;51: 1044-1050, https://doi.org/10.1007/s11661-019-05604-3.

[55] Babu A, Ebrahimi A, Wu K, Richardson IM, Hermans MJM. Local control of microstructure and mechanical properties of high-strength steel in electric arc-based additive manufacturing. J Mater Res Technol-JMRT 2023;26: 1508-1526, https://doi.org/10.1016/j.jmrt.2023.07.262.

[56] Weber B, Meng X, Zhang R, Nitawaki M, Sagawa T, Gardner L. Tensile behaviour of WAAM high strength steel material and members. Mater Des 2024;237: 23, https://doi.org/10.1016/j.matdes.2023.112517.

[57] Li M, Zhang W, Zhou Z, Liang J, Sun X, Wang W et al. Effect of the interlayer temperature on microstructure and mechanical behavior of the high-strength low-alloy steel manufactured by the wire arc additive manufacturing. Mater Today Commun 2025;46: 12, https://doi.org/10.1016/j.mtcomm.2025.112845.

[58] Fang Q, Zhao L, Chen C, Zhu Y, Peng Y, Yin F. Effect of heat input on microstructural and mechanical properties of high strength low alloy steel block parts fabricated by wire

arc additive manufacturing. Mater Today Commun 2023;34: 13, https://doi.org/10.1016/j.mtcomm.2022.105146.

[59] Rodrigues TA, Duarte V, Avila JA, Santos TG, Miranda RM, Oliveira JP. Wire and arc additive manufacturing of HSLA steel: effect of thermal cycles on microstructure and mechanical properties. Addit Manuf 2019;27: 440-450, https://doi.org/10.1016/j.addma.2019.03.029.

[60] Okonkwo BO, Ming H, Wang J, Meng F, Xu X, Han E. Microstructural characterization of low alloy steel a508-309/308l stainless steel dissimilar weld metals. Int J Pressure Vessels Pip 2021;190: 11, https://doi.org/10.1016/j.ijpvp.2020.104297.

[61] Khan M, Dewan MW, Sarkar Z. Effects of welding technique, filler metal and post-weld heat treatment on stainless steel and mild steel dissimilar welding joint. J Manuf Process 2021;64: 1307-1321, https://doi.org/10.1016/j.jmapro.2021.02.058.

[62] Aucott L, Dong H, Mirihanage W, Atwood R, Kidess A, Gao S et al. Revealing internal flow behaviour in arc welding and additive manufacturing of metals. Nat Commun 2018;9: 7, https://doi.org/10.1038/s41467-018-07900-9.

[63] Zhang X, Mi G, Wang C. Microstructure and performance of hybrid laser-arc welded high-strength low alloy steel and austenitic stainless steel dissimilar joint. Opt Laser Technol 2020;122: 7, https://doi.org/10.1016/j.optlastec.2019.105878.

[64] Chen Y, Zuo X, Zhang W, Hao Z, Li Y, Luo Z et al. Enhanced strength-ductility synergy of bimetallic laminated steel structure of 304 stainless steel and low-carbon steel fabricated by wire and arc additive manufacturing. Mater Sci Eng a Struct Mater 2022;856: 10, https://doi.org/10.1016/j.msea.2022.143984.

[65] Ayan Y, Kahraman N. Fabrication and characterization of functionally graded material (FGM) structure containing two dissimilar steels (ER70s-6 and 308LSi) by wire arc additive manufacturing (WAAM). Mater Today Commun 2022;33: 13, https://doi.org/10.1016/j.mtcomm.2022.104457.

[66] Gao L, Yang Y, Gu B, Li S, Xu G, Yu Y. Experimental and simulation analysis on the effect of vibratory stress relief on impact toughness of q345/316 l dissimilar steel welded joints. Mater Today Commun 2024;38: 12, https://doi.org/10.1016/j.mtcomm.2024.108084.

[67] Meng Y, Kang K, Gao M, Zeng X. Microstructures and properties of single-pass laser-arc hybrid welded stainless clad steel plate. J Manuf Process 2018;36: 293-300, https://doi.org/10.1016/j.jmapro.2018.10.022.

[68] Lin Z, Liu B, Zhang B, Ji P, Feng J, Yin F. The evolution behavior and constitution characteristics of interfacial oxides in the hot-rolled stainless steel clad plate. Corros Sci 2023;211: 11, https://doi.org/10.1016/j.corsci.2022.110866.

[69] Ge Y, Que Z, Lindgren K, Hytonen N, Thuvander M. Effect of thermal aging on microstructure and carbides of SA508/alloy 52 dissimilar metal weld. Mater Charact 2023;200: 15,

https://doi.org/10.1016/j.matchar.2023.112880.
[70] Ge G, Hu J, Huo Y, Tang S, Liu Y, Li J et al. Effect of heat input on the microstructure and performance of dissimilar welded joint between q345b low-alloy steel and 2205 duplex stainless steel. J Mater Res Technol-JMRT 2024;33: 4858-4874, https://doi.org/10.1016/j.jmrt.2024.10.165.
[71] You P, Mi H, Feng L, Liao S, Liu Q, He B et al. A comparative investigation on the microstructure and mechanical properties of laser and arc fillet welding of dissimilar steels with flux-cored wire. J Mater Res Technol-JMRT 2025;38: 2325-2340, https://doi.org/10.1016/j.jmrt.2025.08.075.
[72] Feng J, Luo C, Liu J, Liu H, Zhang Y, Chen X et al. Narrow gap multi-pass laser welding with 52m/308l double wires filler addition for SA508/316l dissimilar metals. Int J Pressure Vessels Pip 2024;211: 13, https://doi.org/10.1016/j.ijpvp.2024.105286.
[73] Zhou W, Yue J, Liu S, Zhong P, Zhou H, Wang Z. Research on fusion regulation mechanism of dissimilar steel welds based on compound magnetic field. Int J Pressure Vessels Pip 2025;215: 12, https://doi.org/10.1016/j.ijpvp.2025.105464.
[74] Liu T, Wu Q, Fang Y, Wang Y, Chu Q, Chen Y et al. Characterization of fusion boundary between low alloy steel and stainless steel cladding. J Mater Res Technol-JMRT 2024;28: 2363-2378, https://doi.org/10.1016/j.jmrt.2023.12.183.
[75] Xiao Y, Jing W, Qinghai Z, Zhikai C, Bing H. Microstructure and wear resistance of fe-based and co-based coating of AISI h13. China Welding 2019;28: 54-60, https://doi.org/10.12073/j.cw.20190623001.
[76] Aslam M, Chandan GK, Kanchan BK. Hard and wear resistant AISI304 stainless steel clad layer deposited on mild steel substrate by TIG cladding. Manuf Lett 2024;42: 34-39, https://doi.org/10.1016/j.mfglet.2024.10.003.
[77] Wang Y, Yu T, Zhang Y, Sun J, Sun Z. Process parameter optimization of fe-based coating on ductile iron using laser cladding with grey related analysis. Opt Laser Technol 2025;181: 10, https://doi.org/10.1016/j.optlastec.2024.111906.
[78] Zhang Y, Zhan H, Wan Q, Wang R, Zhang X, Wang W. Multi-objective optimization of process parameters for rectangular laser cladding of fe-based alloy wear-resistant coatings. Surf Coat Technol 2025;503: 15, https://doi.org/10.1016/j.surfcoat.2025.131990.
[79] Liu Z, Han C, Cao X, Guo J, Li H, Lin Y et al. Microstructure and wear behavior of AISI 316l austenitic stainless steel coating fabricated by laser cladding and plasma nitriding. Mater Lett 2025;383: 5, https://doi.org/10.1016/j.matlet.2024.137951.
[80] Santana DA, Koga GY, Wolf W, Bataev IA, Ruktuev AA, Bolfarini C et al. Wear-resistant boride reinforced steel coatings produced by non-vacuum electron beam cladding. Surf Coat Technol 2020;386: 11, https://doi.org/10.1016/j.surfcoat.2020.125466.
[81] Durmuş H, çömez N, Gül C, Yurddaşkal M, Yurddaşkal M. Wear performance of fe-cr-c-b

hardfacing coatings: dry sand/rubber wheel test and ball-on-disc test. International Journal of Refractory Metals and Hard Materials 2018;77: 37-43, https://doi.org/10.1016/j.ijrmhm.2018.07.006.

[82] Yuksel N, Sahin S. Wear behavior-hardness-microstructure relation of fe-cr-c and fe-cr-c-b based hardfacing alloys. Mater Des 2014;58: 491-498, https://doi.org/10.1016/j.matdes.2014.02.032.

[83] Ding T, Li C, Jing W, Di X, Hu W. Influences of boron on the microstructural characteristics and wear performance of hypereutectic fe-cr-c-mo-xb hardfacing alloy. Surf Coat Technol 2024;478: 12, https://doi.org/10.1016/j.surfcoat.2024.130415.

[84] Li G, Dong H, Zhang C, Li Y, Wang Y. Achieving wear resistance enhancement of fe-cr-b-c alloy coating by laser cladding and remelting processes. Opt Laser Technol 2025;190: 11, https://doi.org/10.1016/j.optlastec.2025.113291.

[85] Weimin L, Huawei S, Dashuang L, Jian Q, Lei Z, Hongbo L. Effect of TiC addition on the microstructure and wear resist-ance of induction brazed nickel-based coating in air. China Welding 2022;31: 1-6, https://doi.org/10.12073/j.cw.20221017001.

[86] Gou J, Chen K, Le M, Wang G, Liu J, Tan G et al. A study on the scratch behavior and two-body abrasion wear resistance of TiC-modified e690 steel cladding. Wear 2025;570: 11, https://doi.org/10.1016/j.wear.2025.205923.

[87] Mo K, Cao L, Zhao D, Long Y, Zhong J, Zhong J et al. Study on the microstructure and wear resistance of laser clad martensitic stainless steel 420 with different content of TiC. Mater Today Commun 2025;46: 14, https://doi.org/10.1016/j.mtcomm.2025.112615.

[88] Daniu H, Yonggang T, Manyu H, Honglin M, Jian L, Zhihai C et al. Ultra wear resistant TiC-fe coating prepared by high efficient and economic plasma cladding method. China Welding 2024;33: 20-26, https://doi.org/10.12073/j.cw.20231221023.

[89] Wang X, Zhang Z, Men Y, Li X, Liang Y, Ren L. Fabrication of nano-TiC functional gradient wear-resistant composite coating on 40cr gear steel using laser cladding under starved lubrication conditions. Opt Laser Technol 2020;126: 9, https://doi.org/10.1016/j.optlastec.2020.106136.

[90] Aslam M, Sahoo CK. Development of hard and wear-resistant SiC-AISI304 stainless steel clad layer on low carbon steel by GMAW process. Mater Today Commun 2023;36: 12, https://doi.org/10.1016/j.mtcomm.2023.106444.

[91] Jian Q, Jiao Y, Pan L, Dashuang L, Hongbo L, Qingquan L et al. Microstructure and properties of induction brazing nickel base/WC composite coating. China Welding 2023;32: 27-34, https://doi.org/10.12073/j.cw.20221213001.

[92] Ding H, Cui T, Wang W, Lin Q, Wang L, Yang Y et al. Laser cladding WC/fe composite coating on nose rail of turnout: microstructure characteristics and wear behaviors. Wear 2025;570: 14, https://doi.org/10.1016/j.wear.2025.205929.

[93] Wei R, Mao M, Liang J, Zhao C, Ouyang C, Wang R et al. Study of the effect of overlap rate on the failure form, microstructure and wear resistance of multilayer laser cladding on grey cast iron surfaces. Tribol Int 2024;194: 17, https://doi.org/10.1016/j.triboint.2024.109568.

[94] Liu X, Chen Z, Liu Y, Dong W, Tang H, Li H et al. Enhanced wear resistance of laser cladding al0.5CoCrFeNi coating via in-situ reaction synthesis between ti and b4c particles. J Alloys Compd 2025;1031: 13, https://doi.org/10.1016/j.jallcom.2025.180965.

[95] Shayanfar P, Daneshmanesh H, Janghorban K. Parameters optimization for laser cladding of inconel 625 on ASTM a592 steel. J Mater Res Technol-JMRT 2020;9: 8258-8265, https://doi.org/10.1016/j.jmrt.2020.05.094.

[96] Sadeghi F, Najafi H, Abbasi A. The effect of ta substitution for nb on the microstructure and wear resistance of an fe-cr-c hardfacing alloy. Surf Coat Technol 2017;324: 85-91, https://doi.org/10.1016/j.surfcoat.2017.05.067.

[97] Tang XH, Chung R, Pang CJ, Li DY, Hinckley B, Dolman K. Microstructure of high (45 wt.%) chromium cast irons and their resistances to wear and corrosion. Wear 2011;271: 1426-1431, https://doi.org/10.1016/j.wear.2010.11.047.

[98] Lin C, Lai H, Kuo J, Wu W. Effect of carbon content on solidification behaviors and morphological characteristics of the constituent phases in cr-fe-c alloys. Mater Charact 2011;62: 1124-1133, https://doi.org/10.1016/j.matchar.2011.09.007.

[99] Chung RJ, Tang X, Li DY, Hinckley B, Dolman K. Microstructure refinement of hypereutectic high cr cast irons using hard carbide-forming elements for improved wear resistance. Wear 2013;301: 695-706, https://doi.org/10.1016/j.wear.2013.01.079.

[100] de Sousa JMS, Gil GS, Barbosa MDS, Garcia DN, Lobato MQ, Machado PC. Tribological performance under abrasive wear of fe-cr-c plus nb coating deposited by FCAW process. Wear 2023;523: 13, https://doi.org/10.1016/j.wear.2023.204824.

[101] Tian W, Kong H, Sun Q, Liu Y, Wang C, Sun Q. Thermal history-tailored microstructure, microhardness, and tensile properties in heterogeneous double-wire arc directed energy deposited martensitic stainless steel. J Mater Process Technol 2025;341: 15, https://doi.org/10.1016/j.jmatprotec.2025.118904.

[102] Giarollo DF, Hackenhaar W, Mazzaferro CCP, Mazzaferro JAE. Bead geometry prediction in pulsed GMAW welding: a comparative study on the performance of artificial neural network and regression models. Soldagem Insp 2022;27: 11, https://doi.org/10.1590/0104-9224/SI27.22.

[103] Schauenberg AS, Rodriguez RQ, Almeida DT, Zanon JE, Cunha E, Lopes APO et al. Evaluating thermal gradient in GMAW welding process with a novel heat source model: numerical and experimental approach. Eng Struct 2024;318: 16, https://doi.org/10.1016/j.engstruct.2024.118724.

[104] Peter A, Mutua J, Obiko J, Ngoret J. A comparative study on the effect of GMAW welding current on the performance of API 5l GrB pipeline steel welds for oil and gas industrial

applications. Journal of Pipeline Science and Engineering 2025: 100360, https://doi.org/10.1016/j.jpse.2025.100360.

[105] Bate SK, Charles R, Warren A. Finite element analysis of a single bead-on-plate specimen using SYSWELD. Int J Pressure Vessels Pip 2009;86: 73-78, https://doi.org/10.1016/j.ijpvp.2008.11.006.

[106] Luo W, Mao Z, Cong W, Ma N, Deng D. Numerical simulation of phase volume fraction and hardness in UHSS q960e welded joints. J Manuf Process 2025;153: 49-69, https://doi.org/10.1016/j.jmapro.2025.08.077.

[107] Xiong J, Lei Y, Li R. Finite element analysis and experimental validation of thermal behavior for thin-walled parts in GMAW-based additive manufacturing with various substrate preheating temperatures. Appl Therm Eng 2017;126: 43-52, https://doi.org/10.1016/j.applthermaleng.2017.07.168.

[108] Dadkhah A, Khorrami MS, Kashani-Bozorg SF, Miresmaeili R. The effect of heat input on the residual stress distribution in gas-metal arc welding of carbon steel: simulation and experimental methods. J Adv Join Process 2025;12: 11, https://doi.org/10.1016/j.jajp.2025.100333.

[109] Feng Z, Ma N, Li W, Narasaki K, Lu F. Efficient analysis of welding thermal conduction using the newton-raphson method, implicit method, and their combination. Int J Adv Manuf Technol 2020;111: 1929-1940, https://doi.org/10.1007/s00170-020-06233-6.

[110] Ding J, Colegrove P, Mehnen J, Williams S, Wang F, Almeida PS. A computationally efficient finite element model of wire and arc additive manufacture. Int J Adv Manuf Technol 2014;70: 227-236, https://doi.org/10.1007/s00170-013-5261-x.

[111] Lee C, Chang K. Temperature fields and residual stress distributions in dissimilar steel butt welds between carbon and stainless steels. Appl Therm Eng 2012;45-46: 33-41, https://doi.org/10.1016/j.applthermaleng.2012.04.007.

[112] Chen D, Chen M, Wu C. Effects of phase difference on the behavior of arc and weld pool in tandem p-GMAW. J Mater Process Technol 2015;225: 45-55, https://doi.org/10.1016/j.jmatprotec.2015.05.022.

[113] Wu K, Zeng Y, Zhang M, Hong X, Xie P. Effect of high-frequency phase shift on metal transfer and weld formation in aluminum alloy double-wire DP-GMAW. J Manuf Process 2022;75: 301-319, https://doi.org/10.1016/j.jmapro.2021.12.005.

[114] Schmidt J, Rust B, Stroetmann R. The influence of cooling time on the alloy distribution in weld metals. Welding International 2024;38: 750-761, https://doi.org/10.1080/09507116.2024.2418913.

[115] Darivandpour M, Dehmolaei R, Ranjbar K, Naseri H. Selecting the appropriate filler metal to join HSLA-100 steel by gas tungsten arc welding process. J Mater Eng Perform 2023;32: 10503-10513, https://doi.org/10.1007/s11665-023-07887-5.

[116] Kong H, Liu Y, Ren H, Li F, Kang K, Tao Y et al. Surface modification of mild steel via heterogeneous double-wire arc directed energy deposition: microstructure and performance of cladding layer. Surf Coat Technol 2024;482: 12,

https://doi.org/10.1016/j.surfcoat.2024.130751.
[117] Lv S, Wu H, Wang K, Wang S, Wu G, Gao J et al. The microstructure evolution and influence factors of acicular ferrite in low alloy steels. Comput Mater Sci 2023;218: 11, https://doi.org/10.1016/j.commatsci.2022.111989.
[118] Di X, Ji S, Cheng F, Wang D, Cao J. Effect of cooling rate on microstructure, inclusions and mechanical properties of weld metal in simulated local dry underwater welding. Mater Des 2015;88: 505-513, https://doi.org/10.1016/j.matdes.2015.09.025.
[119] Dornelas PHG, Filho JDCP, Farias FWC, Oliveira VHPM, de Oliveira Moraes D, Junior PZ. Influence of the interpass temperature on the microstructure and mechanical properties of the weld metal (AWS a5.18 ER70s-6) of a narrow gap welded API 5l x70 pipe joint. Int J Pressure Vessels Pip 2022;199: 8, https://doi.org/10.1016/j.ijpvp.2022.104690.
[120] Chen H, Yang Z, Zhang C, Zhu K, van der Zwaag S. On the transition between grain boundary ferrite and bainitic ferrite in fe-c-mo and fe-c-mn alloys: the bay formation explained. Acta Mater 2016;104: 62-71, https://doi.org/10.1016/j.actamat.2015.11.012.
[121] Wu S, Zhang C, Zhu L, Zhang Q, Ma X. In-depth analysis of intragranular acicular ferrite three-dimensional morphology. Scr Mater 2020;185: 61-65, https://doi.org/10.1016/j.scriptamat.2020.03.007.
[122] Bhattacharya A, Mondal K, Upadhyay CS, Sangal S. A phase-field investigation of the effect of grain-boundary diffusion on austenite to ferrite transformation. Comput Mater Sci 2020;173: 13, https://doi.org/10.1016/j.commatsci.2019.109428.
[123] Wei Q, Yang S, Yu H, Mao H, Xu H. Design of high strength mg-li dual-phase alloys by synergistic dislocation and grain size control. J Alloys Compd 2025;1016: 10, https://doi.org/10.1016/j.jallcom.2025.178947.
[124] Jia Y, Wei Y, Ying Z, Cai Z. Synergistic strengthening through dislocations and precipitates in 3cr13MoV martensitic stainless steel achieves an excellent strength-toughness balance. J Alloys Compd 2025;1022: 13, https://doi.org/10.1016/j.jallcom.2025.180111.
[125] Yang X, Di X, Duan Q, Fu W, Ba L, Li C. Effect of precipitation evolution of NiAl and cu nanoparticles on strengthening mechanism of low carbon ultra-high strength seamless tube steel. Mater Sci Eng a Struct Mater 2023;872: 14, https://doi.org/10.1016/j.msea.2023.144939.
[126] Chen J, Lv M, Tang S, Liu Z, Wang G. Influence of cooling paths on microstructural characteristics and precipitation behaviors in a low carbon v-ti microalloyed steel. Mater Sci Eng a Struct Mater 2014;594: 389-393, https://doi.org/10.1016/j.msea.2013.09.086.
[127] Li C, Duan R, Fu W, Gao H, Wang D, Di X. Improvement of mechanical properties for low carbon ultra-high strength steel strengthened by cu-rich multistructured precipitation via modification to bainite. Mater Sci Eng a Struct Mater 2021;817: 13, https://doi.org/10.1016/j.msea.2021.141337.
[128] Xiong Z, Liu S, Wang X, Shang C, Li X, Misra RDK. The contribution of intragranular

acicular ferrite microstructural constituent on impact toughness and impeding crack initiation and propagation in the heat-affected zone (HAZ) of low-carbon steels. Mater Sci Eng a Struct Mater 2015;636: 117-123, https://doi.org/10.1016/j.msea.2015.03.090.

[129] Wang C, Di X, Dai L, Ma Y, Han J, Yang X et al. Correlation between heterogeneous micromechanical properties and fracture toughness in x80 girth weld. Mater Today Commun 2024;41: 13, https://doi.org/10.1016/j.mtcomm.2024.110589.

[130] Saedi AH, Hajjari E, Sadrossadat SM. Microstructural characterization and mechanical properties of TIG-welded API 5l x60 HSLA steel and AISI 310s stainless steel dissimilar joints. Metall Mater Trans a Phys Metall Mater Sci 2018;49A: 5497-5508, https://doi.org/10.1007/s11661-018-4890-y.

[131] Dhib Z, Guermazi N, Gasperini M, Haddar N. Cladding of low-carbon steel to austenitic stainless steel by hot-roll bonding : microstructure and mechanical properties before and after welding. Mater Sci Eng a Struct Mater 2016;656: 130-141, https://doi.org/10.1016/j.msea.2015.12.088.

[132] Zhang Y, Liu Z, Wang Y, Chen Z, Liu H, Wang X. Study on microstructure and sliding wear behavior of similar and dissimilar welded joints produced by laser-arc hybrid welding of wear - resistant steels. Wear 2025;562: 15, https://doi.org/10.1016/j.wear.2024.205643.

[133] Zhang Q, You L, Yu Y, Chen Z, Wang W, Anyakin M et al. Preparation of bainite phase microstructure by laser-electromagnetic induction hybrid solid-state phase transformation. J Mater Res Technol-JMRT 2024;33: 526-534, https://doi.org/10.1016/j.jmrt.2024.08.135.

[134] Jousset N, Gaume M, Bridier F, Beaudet J, Heuze J, Gourgues-Lorenzon A. Effect of the thermal history on macrostructure and microstructure development in high-strength steel welds. Metall Mater Trans a Phys Metall Mater Sci 2022;53: 2561-2576, https://doi.org/10.1007/s11661-022-06686-2.

[135] Xue J, Zhang Y, Guo W, Xia M, Shi J, Zhao G et al. Significantly improving mechanical properties of ultra-high strength steel joints via optimal in - situ post-weld heat treatment. J Mater Process Technol 2025;337: 17, https://doi.org/10.1016/j.jmatprotec.2025.118741.

[136] Sharma V, Shahi AS. Quenched and tempered steel welded with micro-alloyed based ferritic fillers. J Mater Process Technol 2018;253: 2-16, https://doi.org/10.1016/j.jmatprotec.2017.10.039.

[137] Cong Q, Li J, Zhou L, Li M. Simultaneous improvement of strength and uniform elongation of ferrite-bainite steel with heterogeneous networked microstructure. Mater Lett 2024;370: 4, https://doi.org/10.1016/j.matlet.2024.136815.

[138] Tumer M, Schneider-Broskamp C, Enzinger N. Fusion welding of ultra-high strength structural steels-a review. J Manuf Process 2022;82: 203-229, https://doi.org/10.1016/j.jmapro.2022.07.049.

[139] de Sousa JMS, Lobato MQ, Garcia DN, Machado PC. Abrasion resistance of fe - cr - c coating deposited by FCAW welding process. Wear 2021;476: 12,

https://doi.org/10.1016/j.wear.2021.203688.
[140] Buytoz S. Microstructural properties of m 7 c 3 eutectic carbides in a fe-cr-c alloy. Mater Lett 2006;60: 605-608, https://doi.org/10.1016/j.matlet.2005.09.046.
[141] Anijdan SHM, Sabzi M, Najafi H, Jafari M, Eivani AR, Park N et al. The influence of aluminum on microstructure, mechanical properties and wear performance of fe-14%mn-1.05%c manganese steel. J Mater Res Technol-JMRT 2021;15: 4768-4780, https://doi.org/10.1016/j.jmrt.2021.10.054.
[142] Bedolla-Jacuinde A, Hernández B, Béjar-Gómez L. SEM study on the m 7 c 3 carbide nucleation during eutectic solidification of high-chromium white irons. Zeitschrift Fur Metallkunde 2005;96: 1380-1385, https://doi.org/DOI 10.3139/146.101188.
[143] Mahade S, Awe SA, Bjorklund S, Lukac F, Musalek R, Joshi S. Sliding wear behavior of a sustainable fe-based coating and its damage mechanisms. Wear 2022;500: 14, https://doi.org/10.1016/j.wear.2022.204375.
[144] Balasubramanian V, Lakshminarayanan AK, Varahamoorthy R, Babu S. Application of response surface methodolody to prediction of dilution in plasma transferred arc hardfacing of stainless steel on carbon steel. J Iron Steel Res Int 2009;16: 44-53, https://doi.org/DOI 10.1016/S1006-706X(09)60009-1.

Achievements

Publications related to ph.D. thesis:

[1] **Ning Xiao**, Haoyu Kong, Qingjie Sun, **Ninshu Ma***. Study of Process, Microstructure, and Properties of Double-Wire Narrow-Gap Gas Metal Arc Welding Low-Alloy Steel, Materials, 2024.

[2] **Ning Xiao**, Haoyu Kong, Qingjie Sun, **Ninshu Ma***. Comprehensive Evaluation of Double-Wire Narrow Gap GMAW Process and Dissimilar Joint for Chute Structure, Journal of Materials Engineering and Performance, 2025.

[3] **Ning Xiao**, Yujie Tao, Yiheng Liu, Haoyu Kong, Qingjie Sun, **Ninshu Ma***. Wear performance and microstructures of Fe-Cr-C alloy cladding on heterogeneous welded joints of NM450/ER70-G/ZG30SiMn, China Welding, 2025.

[4] **Ning Xiao**, Haoyu Kong, Qingjie Sun, Haiyan Zhao, **Ninshu Ma***. Strength-toughness synergistic enhancement mechanism in double-wire multilayer GMA-deposited HSLA steel via interlayer dwell time strategy, Welding International, 2025.

Acknowledgements

First and foremost, I would like to express my heartfelt gratitude to my academic advisor, Prof. Ninshu Ma, the Director of the Department of Joining Mechanics and Analysis at the Joining and Welding Research Institute. Despite the challenging circumstances in the post-COVID-19 environment and even as he approached retirement, he guided me with patience, dedication, and profound insight. His guidance was indispensable for the completion of my dissertation and my application for a doctoral degree. I am deeply grateful to the members of the doctoral dissertation examination committee, Prof. Naoki Osawa and Associate Prof. Akira Tatsumi of Osaka University, for their invaluable review.

I sincerely appreciate the support, active discussions, and collaborative spirit of the faculty, staff, and colleagues at the Joining and Welding Research Institute (JWRI) of Osaka University. Special thanks to Mr. Kunio Narasaki, Dr. Wenjia Huang and Mr. Renzhi Zhang and other related individuals for their advice on the research content, experimental equipment, and analysis software. I would also like to thank Ms. Michiko Kikuchi and Ms. Eriko Hirose from Prof. Ma's laboratory at JWRI for their great assistance in facilitating the research activities. I am also very grateful to Prof. Daolun Chen for their assistance in the fatigue performance testing of the joints.

I would also like to thank my colleagues, Dr. Qingjie Sun, Mr. Haoyu Kong, Mr. Haiyan Zhao, Yujie Tao, Yiheng Liu etal at METALLECO for their support and encouragement. Their companionship and assistance have been a constant source of motivation throughout my journey toward earning a doctoral degree.

I would like to express my deepest gratitude to my family for their unwavering support during my doctoral studies at Osaka University. Their encouragement and understanding were the foundation that sustained me through every challenge of this journey.

Finally, if I am fortunate enough to be awarded a doctoral degree, I hope that my work can inspire more young researchers in the field of metal welding and enable me to take on greater social responsibilities. Thank you!

Supplementary materials

Microhardness is often used to evaluate wear resistance. The core rationale for assessing wear resistance through microhardness lies in the positive correlation between material hardness and wear resistance, as described by the Archard formula [s1-s2]. Specifically, higher hardness generally corresponds to a greater ability of the material to resist wear. The underlying principle of this relationship is that hardness reflects the material's resistance to local plastic deformation and indentation, while the wear process, particularly abrasive wear and adhesive wear, involves plastic deformation, cutting, or spalling of the material surface [s3]. Higher hardness makes the material surface less susceptible to indentation and ploughing by abrasive particles, thereby reducing the volume loss due to wear. Fig. S1 illustrates the mechanism for evaluating wear resistance through microhardness assessment in this study.

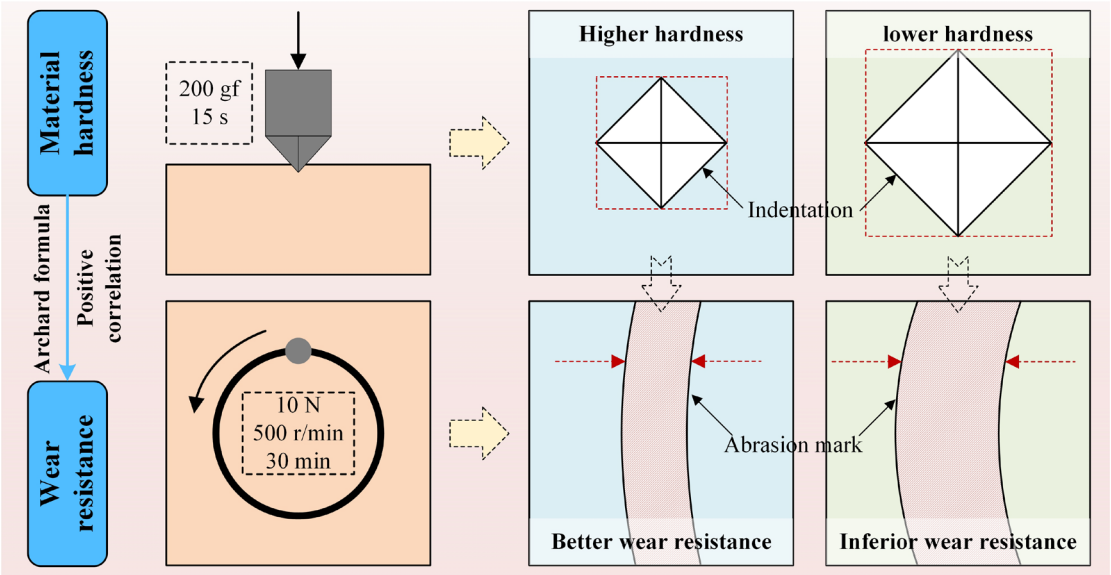


Fig. S1. The principle of evaluating wear resistance through microhardness assessment.

[s1] Aghababaei R, Zhao K. Micromechanics of material detachment during adhesive wear: a numerical assessment of archard's wear model. Wear 2021;476: 6, https://doi.org/10.1016/j.wear.2021.203739.

[s2] Gou S, Li S, Hu H, Fang Y, Liu J, Dong W et al. Surface hardening of CrCoFeNi high-entropy alloys via al laser alloying. Mater Res Lett 2021;9: 437-444, https://doi.org/10.1080/21663831.2021.1968524.

[s3] Delaney BC, Wang QJ, Aggarwal V, Chen W, Evans RD. A contemporary review and data-driven evaluation of archard-type wear laws. Appl Mech Rev 2025;77: 17, https://doi.org/10.1115/1.4068297.